Probing Anomalous Couplings of the Higgs Boson to Weak Bosons and Fermions with Precision Calculations

by

Yaofu Zhou

A dissertation submitted to The Johns Hopkins University

in conformity with the requirements for the degree of

Doctor of Philosophy

Baltimore, Maryland

January, 2019

Abstract

In this thesis I present a phenomenological study of the Higgs boson anomalous couplings to weak bosons and fermions. I focus on Higgs bosons produced in association with a weak boson ($V \to VH$ ($V = W^{\pm}, Z$)) at hadron and lepton colliders, and direct production via proton-proton scattering followed by weak boson decay ($pp \to H \to VV$). The $V \to VH$ interactions as well as the interaction between the Higgs boson and fermions (Hff) are investigated along with the construction of event generators for the $e^-e^+ \to ZH$ and $q\bar{q} \to VH$ processes. Within the framework of JHUGEN, I discuss numerical simulation code that calculates the amplitude for the $q\bar{q} \to VH$ process, including the anomalous HVV and Hff couplings, to next-to-leading order precision in Quantum Chromodynamics (QCD). The $gg \to ZH$ process is also included due to its sizable contribution. The construction of event generators at leading and next-to-leading order are presented in detail. The $pp \to H \to VV$ processes are calculated using modified event generators of MADGRAPH and MCFM with up to next-to-next-to-leading order QCD and NLO Quantum Electrodynamics effects taken into account. I also develop a method for constraining the anomalous Higgs boson (Yukawa) coupling to quarks in the first two generations, and I study the method using early data

from the Large Hadron Collider.

Thesis Committee

Prof. Andrei Gritsan (Joint Advisor)
Professor
Department of Physics & Astronomy
Johns Hopkins Krieger School of Arts & Sciences

Prof. Jared Kaplan (Joint Advisor)
Associate Professor
Department of Physics & Astronomy
Johns Hopkins Krieger School of Arts & Sciences

Dr. Markus C. Schulze
Heisenberg Fellow
Institut für Physik
Humboldt-Universität zu Berlin

Prof. Nadia Zakamska
Associate Professor
Department of Physics & Astronomy
Johns Hopkins Krieger School of Arts & Sciences

Prof. Nitu Kitchloo
Professor
Department of Applied Mathematics & Statistics
Johns Hopkins Krieger School of Arts & Sciences

Acknowledgments

My work on the JHUGEN project went under the instructions and support of Prof. Kirill Melnikov, Prof. Andrei Gritsan, and Dr. Markus C. Schulze. Special Thanks to Dr. Schulze for his mentorship over the past six years. Also special thanks to Dr. Ulascan Sarica and Heshy Roskes for resolving countless technical challenges working on JHUGEN, as well as to Dr. Yanyan Gao for her tireless help on validating my numerical simulation against analytical predictions. I am grateful to Dr. Schulze for his invitation and support to collaborate at MIT and Humboldt University of Berlin, Germany. The wonderful experience at Berlin and hospitality from the theoretical physics group of Humboldt University of Berlin have been the most memorable. I appreciate Dr. Till Martini and Stefan Mölbitz for teaching me a great deal.

The ideas behind the study of the light quark Yukawa couplings were generated in a conversation with Prof. Chien-Peng "C-P" Yuan of the Michigan State University. I am grateful to Prof. Andrei Gritsan and Dr. Markus Schulze for encouragement and useful discussions. I am also grateful to the Department of Physics and Astronomy at the Michigan State University for the hospitality during the visits.

I would like to express my gratitude toward the Johns Hopkins University

and especially the Department of Physics and Astronomy for the unforgettable experience during a significant part of my academic life. Among many others, the discussion with Dr. Jingsheng Li, Dr. Fabrizio Caola, Dr. Liang Dai, Dr. Lin Yang, Dr. Lei "Raymond" Feng, Dr. Can "Candice" You, Dr. Arpit Gupta, and Dr. Ian Anderson were particularly helpful toward the completion of this thesis. Many thanks to Prof. Jared Kaplan, Prof. David E. Kaplan, Prof. Nadia Zakamska, Dr. Reid Mumford, and many other staff members at the Department of Physics and Astronomy for their administrative support during my graduate study.

Last but not the least, I am deeply grateful to Dr. Schulze, Prof. Jonathan A. Bagger, Prof. David M. Lampton, Prof. Gritsan, Prof. Jared Kaplan, and Dr. Jingsheng Li for their advise and support for my career beyond graduate school.

To my parents,

Table of Contents

List of Tables

List of Figures

Chapter 1

Introduction

The Higgs boson was discovered in 2012 first in the its decay to a pair of electroweak bosons ($H \to ZZ$, $H \to W^+W^-$ and $H \to \gamma\gamma$), with a mass of about 125 GeV by the ATLAS and CMS experiments at the Large Hadron Collider (LHC) [1, 2]. In the following years and until recently, almost all of the production mechanisms and the decay modes of the Higgs boson predicted by the Standard Model (SM) have been observed by the ATLAS and CMS experiments. These observations include the production of the Higgs boson in association with a top quark pair ($t\bar{t}H$) [3, 4], the Higgs boson decaying to a pair of bottom quarks ($H \to b\bar{b}$) [5, 6], as well as the Higgs boson decaying to a pair of τ leptons ($H \to \tau^-\tau^+$) [7, 8]. The notable exception is the Higgs boson production via vector boson fusion (HVBF), whose discovery is expected when more LHC data becomes available. During Run I (2009-2013) and II (2015-2018) of the LHC operations, extensive searches and measurements by the ATLAS [9, 10, 11, 12, 13, 14] and CMS [15, 16, 17, 18, 19, 20, 21, 22, 23, 24, 25] have so far shown consistency with SM expectations within the uncertainties. With the analysis of the LHC Run II data, as well as the planning

of future lepton colliders as "Higgs factory" well on the way, the study of the Higgs boson has gradually transitioned from "discovery mode" to "precision mode", where precision measurement of the properties of the Higgs boson are made and constraints of beyond Stand Model (BSM) physics involving the Higgs boson are placed. It is therefore necessary to supply these efforts with beyond leading order (LO) calculations. These calculations should include the anomalous couplings of the Higgs boson, and tools that interface these experimental data with these calculations should be made available.

1.1 Higgs Mechanism

The Higgs mechanism was theorized by R. Brout, F. Englert [26], P. Higgs [27, 28], G. S. Guralnik, C. R. Hagen, and T. W. B. Kibble [29], through which massless vector boson can acquire mass via spontaneous symmetry breaking. The Glashow-Weinberg-Salam theory [30, 31, 32], which unifies the electromagnetic interaction and weak interaction, sees the application of the Higgs mechanism. While the unified electroweak theory has a symmetry of $SU(2) \times U(1)$, corresponding to 4 massless vector bosons; after the spontaneous breaking of the $SU(2)$ gauge symmetry, the degrees of freedom of the 4 massless vector bosons become the massive $W^{\pm}$, Z bosons, the massless photon, as well as the scalar Higgs boson.

To illustrate the Higgs mechanism, the theory of scalar quantum electrodynamics suffices as an example [33, 34]. The Lagrangian of the massless $U(1)$

gauge boson (photon) is

$$\mathscr{L} = -\frac{1}{4} F_{\mu\nu} F^{\mu\nu}, \tag{1.1}$$

where

$$F_{\mu\nu} = \partial_\mu A_\nu - \partial_\nu A_\mu, \tag{1.2}$$

and it observes the $U(1)$ gauge symmetry. That is, this Lagrangian is invariant under the transformation of

$$A_\mu(x) \to A_\mu(x) + \partial_\mu \eta(x) \tag{1.3}$$

for any η and x. A naive addition of the mass term to the Lagrangian

$$\mathscr{L} = -\frac{1}{4} F_{\mu\nu} F^{\mu\nu} + \frac{1}{2} m^2 A_\mu A^\mu \tag{1.4}$$

would violate the local gauge symmetry. Now rather than adding a naive mass term to the Lagrangian, I introduce a complex scalar field ϕ with charge g that couples both to the photon A and to ϕ itself,

$$\mathscr{L} = -\frac{1}{4} F_{\mu\nu} F^{\mu\nu} + (D_\mu \phi)^\dagger (D^\mu \phi) - V(\phi), \tag{1.5}$$

where D is the covariant derivative,

$$D_\mu = \partial_\mu + \mathrm{i} g A_\mu, \tag{1.6}$$

and $V(\phi)$ the Higgs potential,

$$V(\phi) = -\mu^2 \phi^\dagger \phi + \lambda (\phi^\dagger \phi)^2. \tag{1.7}$$

The new Lagrangian is now invariant under the gauge transformations,

$$A_\mu(x) \to A_\mu(x) + \partial_\mu \eta(x) \tag{1.8}$$

$$\phi(x) \to \mathrm{i} e^{-\mathrm{i} g \eta(x)} \phi(x) \tag{1.9}$$

If $\mu^2 < 0$, $\phi = 0$ is the state with minimal energy, and the potential $V(\phi)$ preserves the symmetries of the Lagrangian. If $\mu^2 > 0$, however, the ϕ field acquires a vacuum expectation value (VEV)

$$\langle \phi \rangle = \sqrt{\frac{\mu^2}{2\lambda}} \equiv \frac{v}{2} \tag{1.10}$$

and the global $U(1)$ gauge symmetry is spontaneously broken. The field can be expressed with respect to the VEV,

$$\phi = \frac{v + h}{2} \exp\left(\mathrm{i} \frac{\chi}{v}\right), \tag{1.11}$$

where h can be referred to as the Higgs boson and χ the Goldstone boson. The complex scalar field ϕ with non-zero VEV has now been expressed in terms of two real scalar fields with no VEVs. The Lagrangian can then be rewritten as

$$\begin{aligned} \mathscr{L} = &-\frac{1}{4} F_{\mu\nu} F^{\mu\nu} + g v A_\mu \partial^\mu \chi + \frac{g^2 v^2}{2} A_\mu A^\mu + \frac{1}{2}\left(\partial_\mu h \partial^\mu h - 2\mu^2 h^2\right) \\ &+ \big(\text{interaction terms}\big). \end{aligned} \tag{1.12}$$

The mixing of A_μ and $\partial^\mu \chi$ in the second term can be removed with the choice of unitary gauge,

$$A_\mu \to A_\mu + \frac{1}{g v} \partial_\mu \chi, \tag{1.13}$$

and the Lagrangian becomes

$$\mathscr{L} = -\frac{1}{4}F_{\mu\nu}F^{\mu\nu} + \frac{g^2v^2}{2}A_\mu A^\mu + \frac{1}{2}\left(\partial_\mu h \partial^\mu h - 2\mu^2 h^2\right) + \big(\text{interaction terms}\big). \tag{1.14}$$

The Goldstone boson χ has completely disappeared. The Lagrangian now describes a theory of a $U(1)$ gauge boson A with mass

$$m_A = gv, \tag{1.15}$$

and the Higgs boson with mass

$$m_h = \sqrt{2}\mu = \sqrt{2\lambda}v. \tag{1.16}$$

Notice that before the spontaneously breaking of the $U(1)$ symmetry, there are 2 degrees of freedom from the massless $U(1)$ gauge boson A and 2 from the complex scalar boson ϕ before; and after the spontaneously symmetry breaking there are 3 from the now massive $U(1)$ gauge boson A and 1 from the real scalar Higgs boson h. Therefore the total degrees of freedom in the theory is conserved before and after the symmetry breaking.

In the Standard Model, the $SU(2) \times U(1)$ symmetry is associated with 4 massless vector fields called $W^{1,2,3}$ and B, and a complex scalar field in the representation of $SU(2)$ 2-component spinor

$$\phi = \begin{pmatrix} \phi^+ \\ \phi^0 \end{pmatrix}, \tag{1.17}$$

which amount to 12 degrees of freedom (2 from each massless vector field and

4 from the complex doublet). After the spontaneously breaking of the $U(2)$ symmetry, linear combinations of the massless $W^{1,2}$ fields become the massive $W^{\pm}$ fields; and that of the massless W^3 and B fields become the massive Z field and the massless γ field, which correspond to the massive weak bosons of $W^{\pm}$ and Z and the massless photon. The theory is also left with a real scalar Higgs boson H. With a longitudinal degree of freedom added to each massive boson, the total degrees of freedom remains 12. While a more comprehensive review of the Standard Model can be found in, e.g. Ref. [33, 34], but it is worth pointing out that the interactions among the Higgs boson and the vector bosons can be derived from the covariant derivative of the scalar field ϕ

$$D_\mu \phi = \left(\partial_\mu + \mathrm{i} g T^i W_\mu^i + \mathrm{i} \frac{1}{2} g' B_\mu\right)\phi \tag{1.18}$$

and the Higgs potential

$$V(\phi) = -\mu^2 \phi^\dagger \phi + \lambda (\phi^\dagger \phi)^2, \tag{1.19}$$

and that the interaction strengths are related to the masses in the theory, which allows the Higgs sector of the Standard Model to be tested experimentally.

Among all the Higgs boson interactions, I will focus mainly on those between the Higgs boson and the weak bosons, denoted as HVV, $V = W^{\pm}, Z$; as well as those between the Higgs boson and the quarks, denoted as Hff. I will take the effective field theory approach in studying the Higgs physics beyond the Standard Model, which extends each individual interaction Lagrangian with gauge-invariant operators with higher mass dimensions, and explores the experimental effect of each operator.

1.2 HVV Interaction in the Higgs Boson Production in Association with a Weak Boson

One way to organize the terms in the Lagrangian of an effective field theory is by mass dimension. While in natural unit the overall dimension of a quantum field theory Lagrangian is mass, and equivalently momentum or energy to the forth power, the dimension of each term refers to the total power of mass associated with the involving field strengths as well as their derivatives. The effective HVV interaction Lagrangian with the lowest mass dimensions is[1]

$$\mathscr{L}_{HVV} = g_1^{HVV}\frac{m_V^2}{v}HV_\mu V^\mu + g_2^{HVV}\frac{1}{v}HV_{\mu\nu}V^{\mu\nu} + g_4^{HVV}\frac{1}{v}HV_{\mu\alpha}\widetilde{V^{\mu\beta}} \qquad (1.20)$$

where the superscript of HVV indicates that the dimensionless g_i coefficients are not necessarily identical for different V bosons (I will omit it when unnecessary for simplicity), $v \approx 246\,\text{GeV}$ is the Higgs field vacuum expectation value, Λ denotes the scale where new physics could appear, V_μ is the field vector, $V_{\mu\nu}$ is the field tensor, and $\widetilde{V^{\mu\beta}} = \frac{1}{2}\epsilon_{\rho\sigma\mu\beta}V^{\rho\sigma}$, with $\epsilon_{\rho\sigma\mu\beta}$ being the rank-4 antisymmetric tensor, is the dual field tensor.

For SM Higgs boson coupling to massive vector bosons, Z or W, $g_1^{HZZ} = g_1^{HWW} = 2$, and $g_2^{HVV} = g_4^{HVV} = 0$. A small value of $g_2 \sim \mathcal{O}(\alpha_{\text{Electroweak}}) \sim 10^{-2}$ is generated in the SM by electroweak radiative corrections. The CP-violating constant g_4 is tiny in the SM since it appears only at two-loop level for HWW and three-loop level for HZZ [36]. The SM $H\gamma\gamma$, $HZ\gamma$, or Hgg

[1] The g_3 term $g_3^{HVV}\frac{1}{v}\frac{1}{\Lambda^2}V_{\mu\alpha}V^{\mu\beta}[\partial_\beta\partial^\alpha H]$ from Ref. [35] is omitted in this study because it is high-dimensional and suppressed by a factor of $\frac{1}{\Lambda^2}$ where Λ is the energy scale where new physics could appear.

couplings are loop-induced and thus $g_2 \neq 0$ while the other coefficients are zero [37]. Allowing for effective couplings generated with loops of light particles as well as for beyond the SM scenarios, the g_i couplings can take complex values. Thus the contributions due to different couplings may interfere with a relative phase that is left to be resolved. This will be discussed in Section 2.6.3 and 3.2.6.

To apply Eq. (1.20) to the $e^-e^+/pp \to V^* \to VH$ processes, I start by considering the amplitude of the $V^* \to VH$ decay[2], and applying the correspondence

$$\mathscr{L} = g_1^{HVV}\frac{m_V^2}{v}HV_\mu V^\mu \Rightarrow \mathrm{i}\mathscr{M} = g_1^{HVV}\frac{m_V^2}{v}\epsilon_\mu(p_{V^*})\epsilon^{\mu *}(p_V), \tag{1.21}$$

$$\mathscr{L} = g_2^{HVV}\frac{1}{v}HV_{\mu\nu}V^{\mu\nu} \Rightarrow \mathrm{i}\mathscr{M} = g_2^{HVV}\frac{1}{v}f_{\mu\nu}(p_{V^*})f^{\mu\nu *}(p_V), \tag{1.22}$$

$$\mathscr{L} = g_4^{HVV}\frac{1}{v}HV_{\mu\nu}\widetilde{V}^{\mu\nu} \Rightarrow \mathrm{i}\mathscr{M} = g_4^{HVV}\frac{1}{v}f_{\mu\nu}(p_{V^*})\widetilde{f}^{\mu\nu *}(p_V), \tag{1.23}$$

$$\text{with} \quad f_{\mu\nu}(p_V) = \epsilon_\mu(p_V)p_{V,\nu} - \epsilon_\nu(p_V)p_{V,\mu}, \tag{1.24}$$

$$\text{and} \quad \widetilde{f}_{\mu\nu}(p_V) = \frac{1}{2}\epsilon_{\mu\nu\alpha\beta}f^{\alpha\beta}(p_V) = \epsilon_{\alpha\beta\mu\nu}\epsilon^\alpha p_V^\beta. \tag{1.25}$$

Because different momentum dependences in the scattering amplitude lead to different kinematic distributions measured experimentally, it is useful to collect terms with the same tensor structure in Eq. (1.21-1.25) and define the

[2]While the superscript of * indicates the offshellness of a particle, here it is also used to distinguish the V bosons as parent and child particles.

dimensionless coefficients

$$a_1 = g_1 \frac{m_V^2}{m_H^2} + g_2 \frac{-p_{V^*}.p_V}{m_H^2}, \tag{1.26}$$

$$a_2 = -g_2, \tag{1.27}$$

$$a_3 = -2g_4. \tag{1.28}$$

The $V^* \to VH$ amplitude is then expressed in terms of the a_i coefficients,

$$\mathrm{i}\mathscr{M}_{V^* \to VH} = \frac{1}{v}\epsilon^{\mu}(p_{V^*})\epsilon^{\nu *}(p_V)\Big(a_1 m_V^2 g_{\mu\nu} - a_2 p_{V,\mu} p_{V^*,\nu} - a_3 \epsilon_{\mu\nu\alpha\beta} p_{V^*}^{\alpha} p_V^{\beta}\Big). \tag{1.29}$$

The the a_2 and a_3 terms take a minus sign rather than a plus sign as in Eq. (11) of Ref. [37] because the $H \to VV$ vertex is considered in the latter, and turning an outgoing V into an incoming V^* results in a minus sign associated with the V^* momentum. While the a_i coefficients correspond to different tensor structure of the HVV vertices, in this thesis, theoretical scenarios are defined in terms of the g_i constants.

After the electroweak symmetry breaking, the generic Lagrangian for the Hff interaction of the Higgs boson to fermion is

$$\mathscr{L}_{Hff} = \frac{m_f}{v}\bar{f}(\kappa + \mathrm{i}\tilde{\kappa}\gamma^5)fH \tag{1.30}$$

where κ and $\tilde{\kappa}$ are scaling factors of the scalar and pseudoscalar couplings respectively, and for SM, $\kappa = 1$ and $\tilde{\kappa} = 0$.

1.3 Higgs Boson Production in Association with a Weak Boson in the JHUGEN Event Generator

The study of the Higgs boson in the association production process I am carrying out is with the construction of Monte Carlo event generators for the VH processes, within the JHUGEN [38, 37, 35] framework. JHUGEN is an analysis framework to investigate the Higgs boson. It consists of Monte Carlo event generators and matrix element tools for optimal analysis of anomalous Higgs boson interactions.

All of the HVV and Hff interactions introduced in Section 1.2 are implemented in the relevant vertices in the VH production and subsequent decay of the Higgs boson. The first results from the VH study with JHUGEN is in Ref. [35]. Since then, I have implemented the VH production in gluon fusion, as well as the next-to-leading order (NLO) correction in quantum chromodynamics (QCD) to the quark-initiated VH production process. Although JHUGEN accomodates the Higgs boson decay to any SM particles, in this thesis the focus is given to the decay to to a pair of bottom quarks because it is the dominant decay channel in SM. In addition, while JHUGEN can accomodate V as a photon, and the $H\gamma\gamma$ and $HZ\gamma$ interactions can be switched on, in this thesis I focus on the cases where $V = W^{\pm}, Z$.

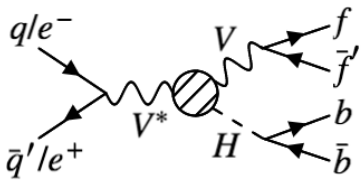

Figure 1.1: Feynman diagram of the $q\bar{q}/e^+e^- \to V^* \to VH \to f\bar{f}'b\bar{b}$ processes. The shaded blob indicates the HVV interactions with anomalous couplings.

At leading order, the geometry of each event from the $q\bar{q}/e^+e^- \to V^* \to VH \to f\bar{f}'b\bar{b}$ processes[3] have 8 degrees of freedom: one invariant mass for each of the V and H bosons, and 6 angular degrees of freedom. One of such angular degree of freedom is the rotation of an event around the colliding beam axis, and is trivial. The rest of the angles are illustrated in Fig. 1.2 in two different reference frames. It is necessary to specify the reference frames in

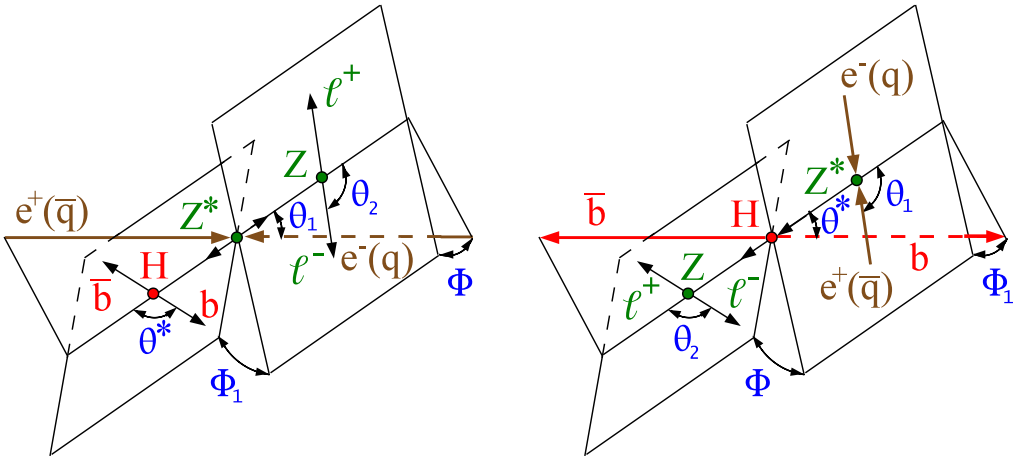

Figure 1.2: Geometry of the $q\bar{q}/e^+e^- \to Z^* \to ZH \to \ell^-\ell^+b\bar{b}$ processes, shown in the Z^* (left) and H (right) rest frames. Graphs are from Ref. [35].

which the angles are defined. $\cos\theta_1$ is defined in the rest frame of Z^*. $\cos\theta_2$

[3] In this thesis, $q\bar{q}$, $q\bar{q}'$, $\bar{q}q'$, and $\bar{q}q'$ will often be collectively referred to as $q\bar{q}'$; and $f\bar{f}$, $f\bar{f}'$, $\bar{f}f'$, and $\bar{f}f'$ as $f\bar{f}'$.

is defined in the rest frame of Z. $\cos\theta^*$, Φ, and Φ_1 are all defined in the rest frame of H. In such choice of the reference frame, the distributions of Φ_1 and $\cos\theta^*$ are trivially flat because of the Higgs boson being a scalar particle.

Notice that some of the angles defined above are LO in nature, and additional particles radiated from anywhere in the process may require redefinition of some of these angles. The NLO kinematics will be discussed in Chapter 4.

1.4 Constraining the Higgs Boson Coupling to Light Quarks in the $H \to ZZ$ Final States

First published in Ref. [39], I proposed a method of constraining the Higgs boson (Yukawa) coupling to quarks in the first two generations in the $H \to ZZ$ final states. Deviation of these couplings from the Standard Model values (by varying κ in Eq. (1.30) leads to change in the Higgs boson width and in the cross sections of relevant processes. In the Higgs boson resonance region, an increased light Yukawa coupling leads to an increased Higgs boson width, which in turn leads to a decreased cross section. In the off-shell region, increased Yukawa couplings result in an enhancement of the Higgs boson signal through $q\bar{q}$ annihilation. With the assumption of scaling one Yukawa coupling at a time, this study is conceptually simple and yields results with the same order of magnitude as the tightest in the literature. The study is based on results published by the CMS experiment at the LHC in 2014, corresponding to integrated luminosities of 5.1 fb^{-1} at a centre-of-mass energy $\sqrt{s} = 7\,\text{TeV}$ and 19.7 fb^{-1} at 8 TeV.

The rest of this thesis is organized as follows. In Chapter 2, I will take the $q\bar{q}/e^+e^- \to V^* \to VH$ processes as an example and introduce in detail the construction of an event generator at leading order, as well as some of its collider-phenomenological results. In Chapter 3, I will present the extension of the generator to include the gluon-initiated $gg \to ZH$ process, which is at one-loop induced leading order. In particular, the construction of the one-loop $gg \to ZH$ amplitudes will be presented in detail. The collider-phenomenological results will also be presented. In Chapter 4, I will present the extension of the generator to include the next-to-leading order correction to the $q\bar{q} \to V^* \to VH$ process, as well as its phenomenological implication. In Chapter 5, I will present one method of constraining of the Higgs boson (Yukawa) coupling to quarks in the first two generations in the $H \to ZZ$ final states. Finally I will conclude and present outlooks in Chapter 6.

Chapter 2

An Event Generator for ZH/WH Production at Leading Order

An event generator is a Monte Carlo integration program that calculates the differential cross section of a scattering process in quantum field theory. In the process, events, i.e. 4-momenta of the relevant particles are returned with their given probability. Random numbers are used to perform the Monte Carlo phase space integration of the cross section. The events with non-uniform weight are called weighted events, and weighted events can be unweighted by keeping an event with a probability equal to its weight divided by the maximum weight among all the events. The result is that all of the retained events have weight one, but are distributed according their probabilities. The unweighted events closely resemble the hard process in high energy collisions, and can be further processed for detector simulation and analysis to predict the outcome of a given theory.

Motivated by the discovery of a new boson by the LHC experiments in 2012 [1, 2], the JHUGEN event generator generates both weighted and unweighted events for processes that involve XVV and Xff interactions,

where X is a boson of spin-0, 1, or 2, and f is a SM fermion of any applicable flavor. With the determination of H being the Higgs boson in the Standard Model within uncertainties, later development of the generator gave focus on the processes involving spin-0VV interactions so that experimental effects of the deviations from the SM HVV interactions can be studied. Two versions of the $q\bar{q}/e^+e^- \to V^* \to VH$ processes have been implemented, in PROCESS=50 and 51 respectively. For the $q\bar{q}/e^+e^- \to V^* \to VH$ processes, the main difference between PROC=50 and 51 is the formulation of their matrix elements. In addition, the $gg \to ZH$ and the next-to-leading order correction to the $q\bar{q} \to V \to VH$ process is implemented in PROC=51 which are presented in Chapter 3 and 4 respectively.

At leading order in quantum chromodynamics, the hadronic cross section for a proton-proton scattering process is

$$\sigma_{pp} = \sum_{a,b} \int \frac{1}{2\hat{s}} \mathrm{d}x_1 \mathrm{d}x_2 \mathrm{PDF}_a(x_1; \mu^2_{\mathrm{Fac}}) \mathrm{PDF}_b(x_2; \mu^2_{\mathrm{Fac}}) \times \int \mathrm{dPS} |\mathscr{M}_{ab,\,\mathrm{LO}}|^2 \Theta(x_1 x_2 s - \hat{s}) \Theta_{\mathrm{cut}}(\{p\}) \quad (2.1)$$

where the sum is performed over all possible parton combinations, s is the square of the center-of-mass energy, or invariant mass, of the colliding hadrons, $x_{1,2}$ are the momentum fractions carried by each parton, $\mathrm{PDF}_a(x_1; \mu^2_{\mathrm{Fac}})$ is the parton distribution function of parton species a at energy scale μ_{Fac}, dPS is the differential phase space, and $\mathscr{M}_{\mathrm{LO},ab}$ is the leading order matrix element, or scattering amplitude of the process with initial-state parton a and b[1]. If the

[1]The subscript LO will be omitted for the remaining of this Chapter for simplicity.

one or both of the scattering hadron is replaced by a lepton, the corresponding summation over its parton species and the integration over the corresponding momentum fraction is dropped. In the case of electron-positron scattering, the cross section is

$$\sigma_{e^+e^-} = \int \frac{1}{2s} \mathrm{dPS} |\mathscr{M}|^2 \Theta_{\mathrm{cut}}(\{p\}) \tag{2.2}$$

The phase space integration is over the four-momenta $\{p\}$ of the final-state particles. The first step function $\Theta(x_1 x_2 s - \hat{s})$ dictates that the invariant mass of initial-state parton combination is sufficient for an event with invariant mass $\sqrt{s}$ to occur. The second step function $\Theta_{\mathrm{cut}}(\{p\})$ specifies the phase space cuts, which dictates that the final-state momenta $\{p\}$ pass certain selection criteria that are usually determined by the collider experiment. In the following sections, I will present the implementation of the above elements in an event generator.

2.1 Phase Space

Including the final-state particles, the $q\bar{q}/e^+e^- \to V^* \to VH \to f\bar{f}'b\bar{b}$ processes, where $f\bar{f}'$ is the fermion pair decayed from the V boson and $b\bar{b}$ is the bottom quark pair decayed from the Higgs boson, is a $2 \to 1 \to 2 \to 4$ process, as shown in Fig. 1.1. On the left of Fig. 2.1, the diagram without specifying the particle identities is shown.

Figure 2.1: Schematic diagrams of a four-body decay process (left) and a two-body decay process (right).

The left of Fig. 2.1 can be seen as three $1 \to 2$ diagrams, shown on the right, connecting to one another.

2.1.1 2-Particle Phase Space

With invariant mass $\sqrt{s_{ij}}$, the phase space integral for the the $1 \to 2$, or $ij \to i, j$ diagram without phase space cuts is

$$\int \mathrm{dPS}_{ij\to i,j} = \int \frac{\mathrm{d}^3\mathbf{p}_i}{(2\pi)^3 2E_i} \int \frac{\mathrm{d}^3\mathbf{p}_j}{(2\pi)^3 2E_j} (2\pi)^4 \delta^{(4)}(p_{ij} - p_i - p_j). \tag{2.3}$$

Let the 4-momenta p take the familiar form of

$$\begin{aligned} p = (E, \mathbf{p}) &= (E, p_x, p_y, p_z) \\ &= (E, |\mathbf{p}| \sin\theta\cos\phi, |\mathbf{p}| \sin\theta \sin\phi, |\mathbf{p}| \cos\theta). \end{aligned} \tag{2.4}$$

The above expression becomes

$$\begin{aligned} \int \mathrm{dPS}_{ij\to i,j} = \int \frac{|\mathbf{p}|_i^2 \mathrm{d}|\mathbf{p}|_i \mathrm{d}\cos\theta_i \mathrm{d}\phi_i}{(2\pi)^3 2E_i} \int \frac{|\mathbf{p}|_j^2 \mathrm{d}|\mathbf{p}|_j \mathrm{d}\cos\theta_j \mathrm{d}\phi_j}{(2\pi)^3 2E_j} \\ \times (2\pi)\delta(E_{ij} - E_i - E_j)(2\pi)^3 \delta^{(3)}(\mathbf{p}_{ij} - \mathbf{p}_i - \mathbf{p}_j). \end{aligned} \tag{2.5}$$

In the center-of-mass frame, $E_{ij}^2 = s_{ij}$, and the second Dirac delta function can be eliminated,

$$\int \mathrm{dPS}_{ij\to i,j} = \int \frac{|\mathbf{p}|_i^2 \mathrm{d}|\mathbf{p}|_i \mathrm{d}\cos\theta_i \mathrm{d}\phi_i}{(2\pi)^3 2E_i 2E_j}(2\pi)\delta(E_{ij} - E_i - E_j), \tag{2.6}$$

$$\text{with} \quad \mathbf{p}_j = -\mathbf{p}_i. \tag{2.7}$$

Applying the identity for Dirac delta function

$$\delta(g(x)) = \frac{\delta(x - x_0)}{\mathrm{d}g(x_0)/\mathrm{d}x}, \tag{2.8}$$

and

$$|\mathbf{p}|^2 \mathrm{d}|\mathbf{p}| = |\mathbf{p}|^2 \mathrm{d}\sqrt{E^2 - m^2} = |\mathbf{p}| E \mathrm{d}E, \tag{2.9}$$

the two-particle phase space integral is finally

$$\int \mathrm{dPS}_{ij\to i,j} = \int \frac{|\mathbf{p}_i| \mathrm{d}\cos\theta_i \mathrm{d}\phi_i}{(2\pi)^2 4E_{ij}}, \tag{2.10}$$

$$\text{with} \quad E_i = \frac{E_{ij}^2 + m_i^2 - m_2^j}{2E_{ij}}, \tag{2.11}$$

$$\text{and} \quad |\mathbf{p}_i| = \frac{\sqrt{E_{ij}^4 + (m_i^2 - m_j^2)^2 - 2(m_i^2 + m_j^2)E_{ij}^2}}{2E_{ij}}. \tag{2.12}$$

In the limit where all of the final-state particles are (treated as) massless,

$$\int \mathrm{dPS}_{ij\to i,j} = \frac{1}{8\pi^2}. \tag{2.13}$$

While Monte Carlo integration for the somewhat trivial $1 \to 2$ phase space seems unnecessary, uniformly distributed random numbers $x_{\cos\theta,\phi}$ between,

say, 0 and 1 can be mapped according to

$$x_{\cos\theta} \to \cos\theta = 2x_{\cos\theta} - 1 \in [-1,1], \quad \text{and} \quad x_\phi \to \phi = 2\pi x_\phi \in [0,2\pi], \tag{2.14}$$

which can be then applied to Eq. (2.11, 2.12, and 2.4) to generate events with particles of momenta p_i and p_j. Of course, these momenta are generated in the center-of-mass frame, and can be boosted to another reference frame as needed.

2.1.2 4-Particle Phase Space

With the $1 \to 2$ phase space understood, the $1 \to 4$ phase space integral without cuts,

$$\int \mathrm{dPS}_{1234\to1,2,3,4} = \prod_{i=1}^{4} \int \frac{\mathrm{d}^3\mathbf{p}_i}{(2\pi)^3 2E_i} (2\pi)^4 \delta^{(4)}(p_{1234} - p_1 - p_2 - p_3 - p_4), \tag{2.15}$$

as needed for the $q\bar{q}/e^+e^- \to V^* \to VH \to f\bar{f}'b\bar{b}$ processes can be assembled to reflect the three $ij \to i,j$ splittings,

$$\begin{aligned}
&\int \mathrm{dPS}_{1234\to1,2,3,4} \\
&= \int \mathrm{dPS}_{1234\to12,34\to1,2,3,4} && (2.16)\\
&= \int \mathrm{dPS}_{1234\to12,34} \int \frac{\mathrm{d}s_{12}}{2\pi} \int \mathrm{dPS}_{12\to1,2} \int \frac{\mathrm{d}s_{34}}{2\pi} \int \mathrm{dPS}_{34\to3,4} && (2.17)\\
&= \int \frac{|\mathbf{p}_{12}|\mathrm{d}\cos\theta_{12}\mathrm{d}\phi_{12}}{(2\pi)^2 4E_{12}} \int \frac{\mathrm{d}s_{12}}{2\pi} \int \frac{|\mathbf{p}_1|\mathrm{d}\cos\theta_1\mathrm{d}\phi_1}{(2\pi)^2 4E_1} \int \frac{\mathrm{d}s_{34}}{2\pi} \int \frac{|\mathbf{p}_3|\mathrm{d}\cos\theta_3\mathrm{d}\phi_3}{(2\pi)^2 4E_3}. && (2.18)
\end{aligned}$$

The limits of the ds_{12} and ds_{34} integrals satisfy

$$(\sqrt{s} - m_1 - m_2)^2 \geq s_{34}, \tag{2.19}$$

$$s \geq (\sqrt{s_{12}} + \sqrt{s_{34}})^2, \tag{2.20}$$

$$s_{12} \geq (m_1 + m_2)^2, \tag{2.21}$$

$$s_{34} \geq (m_3 + m_4)^2, \tag{2.22}$$

where $\sqrt{s}$ is the invariant mass of the event, and m_i is the mass of the i-th particle. It needs to be stressed that each set of E_i, $|\mathbf{p}|_i$, $\cos\theta_i$, and ϕ_i in Eq. (2.18) are defined in the rest frame of the mother particle.

It should be noted that the same phase space integration can be done with different splittings, for example,

$$\begin{aligned} &\int \mathrm{dPS}_{1234\to1,2,3,4} \\ &= \int \mathrm{dPS}_{1234\to123,4\to12,3,4\to1,2,3,4} \qquad (2.23) \\ &= \int \frac{\mathrm{dPS}_{123}}{2\pi} \int \mathrm{dPS}_{1234\to123,4} \int \frac{\mathrm{dPS}_{12}}{2\pi} \int \mathrm{dPS}_{123\to12,3} \int \mathrm{dPS}_{12\to1,2}. \qquad (2.24) \end{aligned}$$

In any case, the 4-particle final state has 8 degrees of freedom – 2 angles at each of the 3 splittings and 2 invariant masses. The splittings can be chosen according to the decaying chain so that the invariant masses can be generated efficiently, which is further discussed below.

2.1.3 Importance Sampling

In the $q\bar{q}/e^+e^- \to V^* \to VH \to f\bar{f}'b\bar{b}$ processes, the invariant mass of the first intermediate vector boson V^* is determined by the scattering partons, and is usually off-shell. The other vector boson V and the Higgs boson H tend to be produced on-shell, and hence their invariant masses follow the Breit-Wigner distributions, which is a consequence of the Feynman propagators, as those appeared in Eq. (2.50),

$$\begin{aligned} |\mathscr{M}|^2 \sim & \frac{1}{\left|p_V^2 - m_V^2 + \mathrm{i}m_V\Gamma_V\right|^2} \frac{1}{\left|p_H^2 - m_H^2 + \mathrm{i}m_H\Gamma_H\right|^2} \\ = & \frac{1}{(p_V^2 - m_V^2)^2 + m_V^2\Gamma_V^2} \frac{1}{(p_H^2 - m_H^2)^2 + m_H^2\Gamma_H^2}, \end{aligned} \tag{2.25}$$

where Γ is the decay width. Unless V is massless, these distributions have sharp peaks around the masses of the boson, shown in Fig. 2.2, and uniformly distributed random numbers cannot efficiently sample their invariant masses.

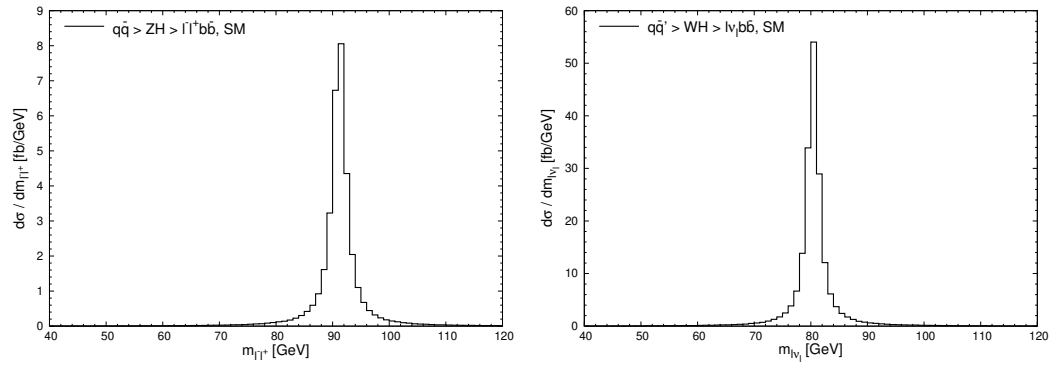

Figure 2.2: Invariant mass distribution of the lepton pair for simulated $q\bar{q} \to ZH \to \ell^-\ell^+b\bar{b}$ events, and that of the lepton-neutrino pair for simulated $q\bar{q}' \to WH \to l\nu_l b\bar{b}$ events.

To improve the sampling efficiency, a change of variable is performed on

the corresponding random number, so that the transformed random number (approximately) follows the Breit-Wigner distribution, and the invariant masses with higher weights are sampled much more often. The Breit-Wigner distribution can be generated using the technique of importance sampling analytically. Starting with the probability distribution,

$$\text{Prob.}(s) \sim |\mathscr{M}|^2 \sim \frac{1}{(s-m^2)^2 + m^2\Gamma^2}, \tag{2.26}$$

the cumulative distribution function (CDF) is

$$\text{CDF}(s) = \frac{1}{\text{NORM}} \int_{s_{\text{min}}}^{s \leq s_{\text{max}}} \frac{\mathrm{d}s'}{(s'-m^2)^2 + m^2\Gamma^2} \tag{2.27}$$

$$= \frac{1}{\text{NORM}} \frac{1}{m\Gamma} \Big[\tan^{-1}\left(\frac{s-m^2}{m\Gamma}\right) - \tan^{-1}\left(\frac{s_{\text{min}}-m^2}{m\Gamma}\right) \Big], \tag{2.28}$$

where the factor of

$$\text{NORM} = \frac{1}{m\Gamma} \Big[\tan^{-1}\left(\frac{s_{\text{max}}-m^2}{m\Gamma}\right) - \tan^{-1}\left(\frac{s_{\text{min}}-m^2}{m\Gamma}\right) \Big] \tag{2.29}$$

dictates that

$$\text{CDF}(s_{\text{min}}) = 0, \tag{2.30}$$

$$\text{and that} \quad \text{CDF}(s_{\text{max}}) = 1. \tag{2.31}$$

Drawing the uniformly distributed random number

$$x_s \in [\text{CDF}(s_{\text{min}}), \text{CDF}(s_{\text{max}})] = [0,1] \tag{2.32}$$

and apply it to the inverse function of CDF(s), the squared invariant mass

$$s = \mathrm{CDF}^{-1}(x_s) \tag{2.33}$$

$$= m^2 + m\Gamma \tan\left(\tan^{-1}\left(\frac{s_{\min} - m^2}{m\Gamma}\right) + \mathrm{NORM}\ x_s m\Gamma\right) \tag{2.34}$$

is generated following the Breit-Wigner distribution. The change of variable from ds to dx_s is associated with a Jacobian

$$\mathbf{J}_s = \mathrm{d}s/\mathrm{d}x_s$$

$$= (m\Gamma)^2(1 + (\tan(x'_s m\Gamma))^2)(x'_{s,max} - x'_{s,min}), \tag{2.35}$$

$$\text{with} \quad x' = x(x'_{s,max} - x'_{s,min}) + x'_{s,min}, \tag{2.36}$$

$$x'_{s,min} = -\frac{1}{m\Gamma}\tan^{-1}(\frac{m}{\Gamma}), \tag{2.37}$$

$$\text{and} \quad x'_{s,max} = -\frac{1}{m\Gamma}\tan^{-1}(\frac{m^2 - s_{\max}}{m\Gamma}). \tag{2.38}$$

Applying all the changes of variables to Eq. (2.18), the phase space integral of the $q\bar{q}/e^+e^- \to V^* \to VH \to f\bar{f}'b\bar{b}$ processes is

$$\int \mathrm{dPS}_{q\bar{q}/e^+e^- \to V^* \to VH \to f\bar{f}'b\bar{b}}$$

$$= \int \mathrm{dPS}_{V^* \to VH \to f\bar{f}'b\bar{b}} \tag{2.39}$$

$$= \int \mathrm{dPS}_{V^* \to VH} \int \frac{\mathrm{d}s_V}{2\pi} \int \mathrm{dPS}_{V \to f\bar{f}'} \int \frac{\mathrm{d}s_H}{2\pi} \int \mathrm{dPS}_{H \to b\bar{b}} \tag{2.40}$$

$$= \int_{(m_f+m_{\tilde{f}'}+2m_b)^2}^{(\sqrt{\hat{s}}-2m_b)^2} \frac{\mathrm{d}s_V}{2\pi} \int_{(2m_b)^2}^{(\sqrt{\hat{s}}-\sqrt{s_V})^2} \frac{\mathrm{d}s_H}{2\pi} \int_{-1}^{1} \mathrm{d}\cos\theta_V \int_0^{2\pi} \mathrm{d}\phi_V \frac{|\mathbf{p}_V|}{(2\pi)^2 4E_V}$$

$$\times \int_{-1}^{1} \mathrm{d}\cos\theta_f \int_0^{2\pi} \mathrm{d}\phi_f \frac{|\mathbf{p}_f|}{(2\pi)^2 4E_f} \int_{-1}^{1} \mathrm{d}\cos\theta_b \int_0^{2\pi} \mathrm{d}\phi_b \frac{|\mathbf{p}_b|}{(2\pi)^2 4E_b} \tag{2.41}$$

$$= \int_0^1 \mathbf{J}_{s_V} \frac{\mathrm{d}x_{s_V}}{2\pi} \int_0^1 \mathbf{J}_{s_H} \frac{\mathrm{d}x s_H}{2\pi} \int_0^1 \mathbf{J}_{\cos\theta_V} \mathrm{d}x_{\cos\theta_V} \int_0^1 \mathbf{J}_{\phi_V} \mathrm{d}x_{\phi_V} \frac{|\mathbf{p}_V|}{(2\pi)^2 4E_V}$$

$$\times \int_0^1 \mathbf{J}_{\cos\theta_f} \mathrm{d}x_{\cos\theta_f} \int_0^1 \mathbf{J}_{\phi_f} \mathrm{d}x_{\phi_f} \frac{|\mathbf{p}_f|}{(2\pi)^2 4E_f} \int_0^1 \mathbf{J}_{\cos\theta_b} \mathrm{d}x_{\cos\theta_b} \int_0^1 \mathbf{J}_{\phi_b} \mathrm{d}x_{\phi_b} \frac{|\mathbf{p}_b|}{(2\pi)^2 4E_b}, \tag{2.42}$$

where

$$\mathbf{J}_y \equiv \mathrm{d}y/\mathrm{d}x_y \tag{2.43}$$

is the Jacobian for the change of variable. Specifically,

$$\mathbf{J}_{\cos\theta} = 2, \quad \mathbf{J}_{\phi} = 2\pi, \tag{2.44}$$

and $\mathbf{J}_s$ is given by Eq. (2.35-2.38). The limits of the ds integrals in Eq. (2.41) are such that the sum of the invariant masses of V and H does not exceed the total available invariant mass $\sqrt{\hat{s}}$ of that event, and that each of them is sufficient for the subsequent decay to take place, as stated in Eq. (2.19-2.22).

In Monte Carlo simulation, the $\int_0^1 \mathrm{d}x$ integrals are approximated by a weighted average. Defining phase space weight

$$\mathrm{PS}_{V^* \to VH \to f\bar{f}'b\bar{b}}$$

$$=\mathrm{PS}_{V^*\to VH\to f\bar{f}'b\bar{b}}(x_{s_V}, x_{s_H}, x_{\cos\theta_V}, x_{\phi_V}, x_{\cos\theta_f}, x_{\phi_f}, x_{\cos\theta_b}, x_{\phi_b}; s) \tag{2.45}$$

$$\equiv\mathrm{PS}(\mathbf{x}; s) \tag{2.46}$$

$$\equiv\frac{\mathbf{J}_{s_V}(x_{s_V}; s)}{2\pi}\frac{\mathbf{J}_{s_H}(x_{s_H}; s)}{2\pi}\mathbf{J}_{\cos\theta_V}(x_{\cos\theta_V})\mathbf{J}_{\phi_V}(x_{\phi_V})\frac{|\mathbf{p}_V(s)|}{(2\pi)^2 4E_V(s)}$$

$$\times\mathbf{J}_{\cos\theta_f}(x_{\cos\theta_f})\mathbf{J}_{\phi_f}(x_{\phi_f})\frac{|\mathbf{p}_f(x_{s_V})|}{(2\pi)^2 4E_f(x_{s_V})}\mathbf{J}_{\cos\theta_b}(x_{\cos\theta_b})\mathbf{J}_{\phi_b}(x_{\phi_b})\frac{|\mathbf{p}_b(x_{s_H})|}{(2\pi)^2 4E_b(x_{s_H})}, \tag{2.47}$$

The phase space integral becomes

$$\int \mathrm{dPS}_{V^*\to VH\to f\bar{f}'b\bar{b}} = \frac{V}{N}\sum_{i=1}^{N}\mathrm{PS}(\mathbf{x_i}; s) + \sigma, \tag{2.48}$$

where V is the volume of the integrated $\mathbf{x}$ space, and conveniently $V = 1$ because all of the components in $\mathbf{x}$ have been chosen to be uniformly distributed random numbers in $[0, 1]$. The estimation of the variance of the integral can be derived from Ref. [40],

$$\sigma^2 \approx \frac{1}{N-1}\left(\frac{1}{N}\sum_{i=1}^{N}\mathrm{PS}(\mathbf{x_i}; s) - \frac{1}{N^2}\sum_{i=1}^{N}\mathrm{PS}^2(\mathbf{x_i}; s)\right). \tag{2.49}$$

Again, an event can be generated with each set of $\mathbf{x}$. Specifically, four-momenta of the intermediate and final-state particles can be calculated in the rest frames of the mother particles by Eq. (2.4, 2.11, 2.12, and 2.14); invariant masses of the intermediate particles can be determined by Eq. (2.34); and $E_{ij}^2 = s_{ij}$ in the rest frame of particle ij. Before an event is written down (see Section 2.5.2) for analysis or is processed to produce statical distributions, the four-momenta of all of the particles involved are boosted to the reference frame of the laboratory (see Section 2.5.1), where kinematic selection can be

properly applied.

The phase space weight of an event $\mathrm{PS}(\mathbf{x}; s)$ is further multiplied by the squared matrix element of the process and other factors seen in Eq. (2.1 or 2.2) to form the weight of the event (see Eq. (2.116-2.117)), as well as to evaluate the cross section of the process. The construction of the leading order amplitudes is presented in the next section.

The numerical integration in JHUGEN is implemented with the VEGAS algorithm [40], which supplies all of the random numbers, as well as applies additional importance sampling during the numerical integration. As a result, an additional Jacobian due to VEGAS is supplied and multiplied to the event weights.

2.2 Matrix Elements

For definiteness and without loss of too much generality, in this section I am mostly treating the $e^+e^- \to Z^* \to ZH \to \ell^-\ell^+ b\bar{b}$ process, whose leading order matrix element with anomalous couplings is

$$
\begin{aligned}
&\mathrm{i}\mathscr{M}_{e^+e^-\to Z^*\to ZH\to \ell^-\ell^+ b\bar{b},\ \mathrm{LO}} \\
=&\bar{\psi}(p_{e^+}, h_{e^+})\big(\mathrm{i}\frac{2M_Z}{v}\gamma_\mu(g_V^{Zee} - g_A^{Zee}\gamma^5)\big)\psi(p_{e^-}, h_{e^-}) \\
\times&\bar{\psi}(p_{\ell^-}, h_{\ell^-})\big(\mathrm{i}\frac{2M_Z}{v}\gamma_\nu(g_V^{Zll} - g_A^{Zll}\gamma^5)\big)\psi(p_{\ell^+}, h_{\ell^+}) \\
\times&\bar{\psi}(p_b, h_b)\big(-\mathrm{i}\frac{m_b}{v}(\kappa + \mathrm{i}\tilde{\kappa}\gamma^5)\big)\psi(p_{\bar{b}}, h_{\bar{b}})
\end{aligned}
$$

$$\times \frac{\mathrm{i}(-g^{\mu\alpha} + p^{\mu}_{Z^*} p^{\alpha}_{Z^*}/m_Z^2)}{p^2_{Z^*} - m_Z^2 + \mathrm{i}m_Z\Gamma_Z} \frac{\mathrm{i}(-g^{\beta\nu} + p^{\beta}_{Z} p^{\nu}_{Z}/m_Z^2)}{p^2_{Z} - m_Z^2 + \mathrm{i}m_Z\Gamma_Z} \frac{\mathrm{i}}{p^2_H - m_H^2 + \mathrm{i}m_H\Gamma_H}$$

$$\times \frac{\mathrm{i}}{v}(a_1 g_{\alpha\beta} m_H^2 - a_2 p_{V,\alpha} p_{V^*,\beta} - a_3 \epsilon_{\alpha\beta\rho\sigma} p^{\rho}_{Z^*} p^{\sigma}_{Z}), \tag{2.50}$$

where (p, h) denotes the momentum and helicity dependencies of fermion spinors, $v \approx 246$ GeV is the vacuum expectation value of the Higgs field, g_V^{Zff} and g_A^{Zff} are the vector and axial couplings between the Z boson and f-fermion current, κ ($\tilde{\kappa}$) is the scaling factor of the Higgs boson (pseudo-)scalar coupling to fermions with $\kappa = 1$ ($\tilde{\kappa} = 0$) being SM, and the coefficients a_1, a_2 and a_3 are defined in Eq. (1.26-1.28). Notice that the a_2 and a_3 terms receive minus signs because in Eq. (11) of Ref. [37] it was defined in the $H \to VV$ decay, and here one of the outgoing Z has been replaced by an incoming Z^*. The values of g_V^{Zff} and g_A^{Zff} in the Standard Model are

$$g_V^{Zff} = \frac{1}{2} T_f^3 - Q_f \sin^2\theta_{\mathrm{W}}, \tag{2.51}$$

$$g_A^{Zff} = \frac{1}{2} T_f^3, \tag{2.52}$$

where

$$T^3_{l_L} = T^3_{d_L} = -\frac{1}{2}, \tag{2.53}$$

$$T^3_{\nu_L} = T^3_{u_L} = \frac{1}{2}, \tag{2.54}$$

$$T^3_{l_R} = T^3_{u_R} = 0, \tag{2.55}$$

Q_f is the electric charge of the particle species f, and θ_W is the weak mixing angle with $\cos\theta_{\mathrm{W}} = m_W/m_Z$ at LO.

2.3 Calculating Matrix Elements with Feynman Rules in the Traditional Manner

The first implementation of the $q\bar{q}/e^+e^- \to V^* \to VH \to f\bar{f}'b\bar{b}$ matrix elements in the JHUGEN event generator is with PROCESS=50. In Eq. (2.50), the matrix element consists of fermion spinors, polarization vectors for external vector bosons, propagators for intermediate particles, and interaction vertices. In this implementation, inner product of fermion spinors (with γ^5 "sandwiched" in between) have been taken to form Lorentz-invariant (pseudo-)scalars. Fermion spinors are also combined with γ_μ and $\gamma_\mu\gamma^5$ to form vector and axial currents.

Since the energy scale of the VH production is sufficiently high, I have taken the limit where the spinors of external fermions are massless. This not only greatly simplifies the scalar, pseudoscalar, vector, and axial vectors formed by the spinors; but also eliminates the $p^\mu_{Z^*}p^\alpha_{Z^*}/m^2_Z$ and $p^\beta_Z p^\nu_Z/m^2_Z$ tensors in the numerators of the vector boson propagators, via the massless Dirac equation,

$$\begin{aligned} \text{or,} \quad p_\mu\gamma^\mu\psi(p,h) &= 0 \\ \bar{\psi}(p,h)p_\mu\gamma^\mu &= 0, \end{aligned} \tag{2.56}$$

and thus allowing the fermion currents to directly Lorentz-contract with the HVV interaction tensor.

2.3.1 Spinor Products

Some of the expressions, conventions, and derivations in this and the next subsection were adopted from Appendix B of Ref. [41]. I adopt the γ-matrices

$$\gamma^0 = \begin{pmatrix} 0 & 0 & 1 & 0 \\ 0 & 0 & 0 & 1 \\ 1 & 0 & 0 & 0 \\ 0 & 1 & 0 & 0 \end{pmatrix}, \quad \gamma^1 = - \begin{pmatrix} 0 & 0 & 0 & 1 \\ 0 & 0 & 1 & 0 \\ 0 & -1 & 0 & 0 \\ -1 & 0 & 0 & 0 \end{pmatrix},$$

$$\gamma^2 = - \begin{pmatrix} 0 & 0 & 0 & -\mathrm{i} \\ 0 & 0 & \mathrm{i} & 0 \\ 0 & \mathrm{i} & 0 & 0 \\ -\mathrm{i} & 0 & 0 & 0 \end{pmatrix}, \quad \gamma^3 = - \begin{pmatrix} 0 & 0 & 1 & 0 \\ 0 & 0 & 0 & -1 \\ -1 & 0 & 0 & 0 \\ 0 & 1 & 0 & 0 \end{pmatrix}, \tag{2.57}$$

$$\text{and, additionally,} \quad \gamma^5 \equiv \mathrm{i}\gamma^0\gamma^1\gamma^2\gamma^3 = \begin{pmatrix} 1 & 0 & 0 & 0 \\ 0 & 1 & 0 & 0 \\ 0 & 0 & -1 & 0 \\ 0 & 0 & 0 & -1 \end{pmatrix}. \tag{2.58}$$

The left and right projection operators are defined as

$$P_L \equiv \frac{1}{2}(\mathbf{1} - \gamma^5) = \begin{pmatrix} 0 & 0 & 0 & 0 \\ 0 & 0 & 0 & 0 \\ 0 & 0 & 1 & 0 \\ 0 & 0 & 0 & 1 \end{pmatrix}, \quad P_R \equiv \frac{1}{2}(\mathbf{1} + \gamma^5) = \begin{pmatrix} 1 & 0 & 0 & 0 \\ 0 & 1 & 0 & 0 \\ 0 & 0 & 0 & 0 \\ 0 & 0 & 0 & 0 \end{pmatrix}, \tag{2.59}$$

which, when operating on a generic spinor, will project out its left (lower) or right (upper) component. With the fermion momentum defined in Eq. (2.4), the solutions of the massless Dirac equation Eq. (2.56) in the left and right basis are

$$\psi(p, h = L) = u_-(p) = v_+(p) = \begin{pmatrix} 0 \\ 0 \\ \frac{p_x - \mathrm{i}p_y}{\sqrt{E + p_z}} \\ -\sqrt{E + p_z} \end{pmatrix}, \tag{2.60}$$

$$\psi(p, h = R) = u_+(p) = v_-(p) = \begin{pmatrix} \sqrt{E + p_z} \\ \frac{p_x + \mathrm{i}p_y}{\sqrt{E + p_z}} \\ 0 \\ 0 \end{pmatrix}, \tag{2.61}$$

and

$$\bar{\psi}(p, h = L) = \psi^\dagger(p, h = L)\gamma^0 = \overline{u_-}(p) = \overline{v_+}(p)$$

$$= (\frac{p_x + \mathrm{i}p_y}{\sqrt{E + p_z}}, -\sqrt{E + p_z}, 0, 0), \tag{2.62}$$

$$\bar{\psi}(p, h = R) = \psi^\dagger(p, h = R)\gamma^0 = \overline{u_+}(p) = \overline{v_-}(p)$$

$$= (0, 0, \sqrt{E + p_z}, \frac{p_x - \mathrm{i}p_y}{\sqrt{E + p_z}}). \tag{2.63}$$

Notice the degeneracy between the particle and antiparticle states with opposite spins. The non-zero spinor products are

$$\langle ij \rangle \equiv \bar{\psi}(p_i, h = L)\psi(p_j, h = R)$$

$$= \frac{(p_{i,x} + \mathrm{i}p_{i,y})\sqrt{E_j + p_{j,z}}}{\sqrt{E_i + p_{i,z}}} - \frac{(p_{j,x} + \mathrm{i}p_{j,y})\sqrt{E_i + p_{i,z}}}{\sqrt{E_j + p_{j,z}}} \tag{2.64}$$

and $\quad [ij] \equiv \bar{\psi}(p_i, h = R)\psi(p_j, h = L)$

$$= \frac{(p_{i,x} - \mathrm{i}p_{i,y})\sqrt{E_j + p_{j,z}}}{\sqrt{E_j + p_{j,z}}} - \frac{(p_{j,x} - \mathrm{i}p_{j,y})\sqrt{E_i + p_{i,z}}}{\sqrt{E_i + p_{i,z}}}. \tag{2.65}$$

In addition, the non-zero spinor products with a γ^5 matrix sandwiched in between are

$$\mathrm{i}\bar{\psi}(p_i, h = L)\gamma^5\psi(p_j, h = R)$$

$$= \frac{\mathrm{i}(p_{i,x} + \mathrm{i}p_{i,y})\sqrt{E_j + p_{j,z}}}{\sqrt{E_i + p_{i,z}}} - \frac{\mathrm{i}(p_{j,x} + \mathrm{i}p_{j,y})\sqrt{E_i + p_{i,z}}}{\sqrt{E_j + p_{j,z}}} \tag{2.66}$$

$$= \mathrm{i}\langle ij \rangle \tag{2.67}$$

$$\text{and} \quad \mathrm{i}\bar{\psi}(p_i, h = R)\gamma^5\psi(p_j, h = L)$$

$$= -\frac{\mathrm{i}(p_{i,x} - \mathrm{i}p_{i,y})\sqrt{E_j + p_{j,z}}}{\sqrt{E_j + p_{j,z}}} + \frac{\mathrm{i}(p_{j,x} - \mathrm{i}p_{j,y})\sqrt{E_i + p_{i,z}}}{\sqrt{E_i + p_{i,z}}} \tag{2.68}$$

$$= -\mathrm{i}[ij]. \tag{2.69}$$

It is worth pointing out that the spinor products above do not contain singularities as p_z approaches $-E$, since at the same time both p_x and p_y are approaching 0 as well. In these limits,

$$\lim_{p_z \to -E} \psi(p, h = L) = \begin{pmatrix} 0 \\ 0 \\ \sqrt{2E} \\ 0 \end{pmatrix}, \quad \lim_{p_z \to -E} \psi(p, h = R) = \begin{pmatrix} 0 \\ \sqrt{2E} \\ 0 \\ 0 \end{pmatrix}, \tag{2.70}$$

and the expressions of the spinor products do not have numerical instability, which can be implemented when $E + p_z$ approaches the machine precision $\epsilon_{\text{machine}}$. An alternative implementation is to add a small quantity slightly above the machine precision to the square root in the denominator so that dividing by zero does not occur. For example,

$$\begin{pmatrix} 0 \\ 0 \\ \dfrac{p_x - \mathrm{i}p_y}{\sqrt{E + p_z}} \\ -\sqrt{E + p_z} \end{pmatrix} \to \begin{pmatrix} 0 \\ 0 \\ \dfrac{p_x - \mathrm{i}p_y}{\sqrt{E + p_z} + \epsilon_{\text{machine}}} \\ -\sqrt{E + p_z} \end{pmatrix}. \tag{2.71}$$

2.3.2 Fermion Currents

Spinors can sandwich γ^μ and $\gamma^\mu\gamma^5$ to form fermion vector and axial currents. In the limit where fermions are massless, the currents are either left- or right-handed. With the expressions from Section 2.3.1, the non-zero vector currents J_V are

$$J^\mu_{V,L}(p_i, p_j) = \bar{\psi}(p_i, h = L)\gamma^\mu\psi(p_j, h = L)$$

$$= \overline{u}_-(p_i)\gamma^\mu u_-(p_j) = \overline{u}_-(p_i)\gamma^\mu v_+(p_j) = \overline{v}_+(p_i)\gamma^\mu u_-(p_j) = \overline{v}_+(p_i)\gamma^\mu v_+(p_j) \tag{2.72}$$

$$= \begin{pmatrix} \frac{(p_{i,x} + \mathrm{i}p_{i,y})(p_{j,x} - \mathrm{i}p_{j,y})}{\sqrt{E_i + p_{i,z}}\sqrt{E_j + p_{j,z}}} + \sqrt{E_i + p_{i,z}}\sqrt{E_j + p_{j,z}} \\ \frac{\sqrt{E_i + p_{i,z}}(p_{j,x} - \mathrm{i}p_{j,y})}{\sqrt{E_j + p_{j,z}}} + \frac{\sqrt{E_j + p_{j,z}}(p_{i,x} + \mathrm{i}p_{i,y})}{\sqrt{E_i + p_{i,z}}} \\ \frac{\mathrm{i}\sqrt{E_i + p_{i,z}}(p_{j,x} - \mathrm{i}p_{j,y})}{\sqrt{E_j + p_{j,z}}} - \frac{\mathrm{i}\sqrt{E_j + p_{j,z}}(p_{i,x} + \mathrm{i}p_{i,y})}{\sqrt{E_i + p_{i,z}}} \\ -\frac{(p_{i,x} + \mathrm{i}p_{i,y})(p_{j,x} - \mathrm{i}p_{j,y})}{\sqrt{E_i + p_{i,z}}\sqrt{E_j + p_{j,z}}} + \sqrt{E_i + p_{i,z}}\sqrt{E_j + p_{j,z}} \end{pmatrix}^{\mathrm{T}}, \tag{2.73}$$

$$J^\mu_{V,R}(p_i, p_j) = \bar{\psi}(p_i, h = R)\gamma^\mu\psi(p_j, h = R)$$

$$= \overline{u}_+(p_i)\gamma^\mu u_+(p_j) = \overline{u}_+(p_i)\gamma^\mu v_-(p_j) = \overline{v}_-(p_i)\gamma^\mu u_+(p_j) = \overline{v}_-(p_i)\gamma^\mu v_-(p_j) \tag{2.74}$$

$$= \begin{pmatrix} \frac{(p_{i,x} - \mathrm{i}p_{i,y})(p_{j,x} + \mathrm{i}p_{j,y})}{\sqrt{E_i + p_{i,z}}\sqrt{E_j + p_{j,z}}} + \sqrt{E_i + p_{i,z}}\sqrt{E_j + p_{j,z}} \\ \frac{\sqrt{E_i + p_{i,z}}(p_{j,x} + \mathrm{i}p_{j,y})}{\sqrt{E_j + p_{j,z}}} + \frac{\sqrt{E_j + p_{j,z}}(p_{i,x} - \mathrm{i}p_{i,y})}{\sqrt{E_i + p_{i,z}}} \\ -\frac{\mathrm{i}\sqrt{E_i + p_{i,z}}(p_{j,x} + \mathrm{i}p_{j,y})}{\sqrt{E_j + p_{j,z}}} + \frac{\mathrm{i}\sqrt{E_j + p_{j,z}}(p_{i,x} - \mathrm{i}p_{i,y})}{\sqrt{E_i + p_{i,z}}} \\ -\frac{(p_{i,x} - \mathrm{i}p_{i,y})(p_{j,x} + \mathrm{i}p_{j,y})}{\sqrt{E_i + p_{i,z}}\sqrt{E_j + p_{j,z}}} + \sqrt{E_i + p_{i,z}}\sqrt{E_j + p_{j,z}} \end{pmatrix}^{\mathrm{T}} ; \tag{2.75}$$

and the non-zero axial currents J_A are

$$\begin{aligned} J^{\mu}_{A,L}(p_i, p_j) &= \bar{\psi}(p_i, h = L)\gamma^{\mu}\gamma^5\psi(p_j, h = L) \\ &= \overline{u}_-(p_i)\gamma^{\mu}\gamma^5 u_-(p_j) = \overline{u}_-(p_i)\gamma^{\mu}\gamma^5 v_+(p_j) \\ &= \overline{v}_+(p_i)\gamma^{\mu}\gamma^5 u_-(p_j) = \overline{v}_+(p_i)\gamma^{\mu}\gamma^5 v_+(p_j) \end{aligned} \tag{2.76}$$

$$= \begin{pmatrix} -\frac{(p_{i,x} + \mathrm{i}p_{i,y})(p_{j,x} - \mathrm{i}p_{j,y})}{\sqrt{E_i + p_{i,z}}\sqrt{E_j + p_{j,z}}} - \sqrt{E_i + p_{i,z}}\sqrt{E_j + p_{j,z}} \\ -\frac{\sqrt{E_i + p_{i,z}}(p_{j,x} - \mathrm{i}p_{j,y})}{\sqrt{E_j + p_{j,z}}} - \frac{\sqrt{E_j + p_{j,z}}(p_{i,x} + \mathrm{i}p_{i,y})}{\sqrt{E_i + p_{i,z}}} \\ -\frac{\mathrm{i}\sqrt{E_i + p_{i,z}}(p_{j,x} - \mathrm{i}p_{j,y})}{\sqrt{E_j + p_{j,z}}} + \frac{\mathrm{i}\sqrt{E_j + p_{j,z}}(p_{i,x} + \mathrm{i}p_{i,y})}{\sqrt{E_i + p_{i,z}}} \\ \frac{(p_{i,x} + \mathrm{i}p_{i,y})(p_{j,x} - \mathrm{i}p_{j,y})}{\sqrt{E_i + p_{i,z}}\sqrt{E_j + p_{j,z}}} + \sqrt{E_i + p_{i,z}}\sqrt{E_j + p_{j,z}} \end{pmatrix}^{\mathrm{T}} , \tag{2.77}$$

$$\begin{aligned} J^{\mu}_{A,R}(p_i, p_j) &= \bar{\psi}(p_i, h = R)\gamma^{\mu}\gamma^5\psi(p_j, h = R) \\ &= \overline{u}_+(p_i)\gamma^{\mu}\gamma^5 u_+(p_j) = \overline{u}_+(p_i)\gamma^{\mu}\gamma^5 v_-(p_j) \end{aligned}$$

$$= \overline{v}_-(p_i)\gamma^\mu\gamma^5 u_+(p_j) = \overline{v}_-(p_i)\gamma^\mu\gamma^5 v_-(p_j) \tag{2.78}$$

$$= \begin{pmatrix} \frac{(p_{i,x}-\mathrm{i}p_{i,y})(p_{j,x}+\mathrm{i}p_{j,y})}{\sqrt{E_i+p_{i,z}}\sqrt{E_j+p_{j,z}}} + \sqrt{E_i+p_{i,z}}\sqrt{E_j+p_{j,z}} \\ \frac{\sqrt{E_i+p_{i,z}}(p_{j,x}+\mathrm{i}p_{j,y})}{\sqrt{E_j+p_{j,z}}} + \frac{\sqrt{E_j+p_{j,z}}(p_{i,x}-\mathrm{i}p_{i,y})}{\sqrt{E_i+p_{i,z}}} \\ -\frac{\mathrm{i}\sqrt{E_i+p_{i,z}}(p_{j,x}+\mathrm{i}p_{j,y})}{\sqrt{E_j+p_{j,z}}} + \frac{\mathrm{i}\sqrt{E_j+p_{j,z}}(p_{i,x}-\mathrm{i}p_{i,y})}{\sqrt{E_i+p_{i,z}}} \\ -\frac{(p_{i,x}-\mathrm{i}p_{i,y})(p_{j,x}+\mathrm{i}p_{j,y})}{\sqrt{E_i+p_{i,z}}\sqrt{E_j+p_{j,z}}} + \sqrt{E_i+p_{i,z}}\sqrt{E_j+p_{j,z}} \end{pmatrix}^{\mathrm{T}}. \tag{2.79}$$

Again, in the limit of $E + p_z$ approaching 0, special care needs to be taken, and either treatment in Eq. (2.70) or Eq. (2.71) may be applied.

2.3.3 Polarization Vectors and Propagators

Up to gauge redundancy, a massive vector boson with momentum

$$p = (E, 0, 0, |\mathbf{p}|), \tag{2.80}$$

has two transverse polarization vectors

$$\varepsilon_\pm = (0, \mp\frac{1}{\sqrt{2}}, -\frac{\mathrm{i}}{\sqrt{2}}, 0), \tag{2.81}$$

and one longitudinal polarization vector

$$\varepsilon_0 = (\frac{|\mathbf{p}|}{m}, 0, 0, \frac{E}{m}). \tag{2.82}$$

If the vector boson is massless, as in the case of gluon or photon, the longitudinal polarization vector does not exist. For a vector boson with generic

momentum

$$p = (E, \mathbf{p}) = (E, p_x, p_y, p_z)$$

$$= (E, |\mathbf{p}| \sin\theta\cos\phi, |\mathbf{p}| \sin\theta \sin\phi, |\mathbf{p}| \cos\theta), \quad (2.83)$$

which is rotated from Eq. (2.80) by the rotation operator

$$R(\theta, \phi) = \begin{pmatrix} 1 & 0 & 0 & 0 \\ 0 & \cos\phi\cos\theta & -\sin\phi & \cos\phi\sin\theta \\ 0 & \sin\phi\cos\theta & \cos\phi & \sin\phi\sin\theta \\ 0 & -\sin\theta & 0 & \cos\theta \end{pmatrix}, \quad (2.84)$$

the polarization vectors can be rotated from Eq. (2.81 and 2.82) by the same operator,

$$\varepsilon_{\pm}(p) = (0, \frac{\mp\cos\theta\cos\phi + \mathrm{i}\sin\theta}{\sqrt{2}}, \frac{\mp\cos\theta\sin\phi - \mathrm{i}\cos\phi}{\sqrt{2}}, \frac{\pm\sin\theta}{\sqrt{2}}) \quad (2.85)$$

$$\varepsilon_0(p) = (\frac{|\mathbf{p}|}{m}, \frac{E\sin\theta\cos\phi}{m}, \frac{E\sin\theta\sin\phi}{m}, \frac{E\cos\theta}{m}). \quad (2.86)$$

The numerator of the propagator of a vector boson is a rank-2 tensor, as appeared in Eq. (2.50). It is an option to decompose the rank-2 tensor in the vector boson propagator into the sum of outer products of the polarization vectors,

$$-g^{\mu\nu} + \frac{p^\mu p^\nu}{m_V^2} = \sum_{\lambda=\pm,0} \varepsilon_\lambda^\mu(p)\varepsilon_\lambda^{\nu*}(p) \quad (2.87)$$

and to have the polarization vectors Lorentz-contract with the external currents and the tensor of the HVV interaction that the propagator connects,

$$\begin{aligned} \mathrm{i}\mathscr{M} \sim & J_\mu(\text{propagator})^{\mu\alpha}(Z^*ZH \text{ vertex})_{\alpha\beta}(\text{propagator})^{\beta\nu}J_\nu \\ \sim & \sum_{\lambda_1=\pm,0}\sum_{\lambda_2=\pm,0}(J_\mu\varepsilon^\mu_{\lambda_1})(\varepsilon^{\mu *}_{\lambda_1}(Z^*ZH \text{ vertex})_{\mu\nu}\varepsilon^\nu_{\lambda_2})(\varepsilon^{\mu *}_{\lambda_2}J_\mu). \end{aligned} \tag{2.88}$$

For the $q\bar{q}/e^+e^- \to V^* \to VH \to f\bar{f}'b\bar{b}$ processes, however, this is not necessary, because when the $p_Z^{\mu(*)}p_Z^{\nu(*)}/m_Z^2$ terms Lorentz-contract with the massless fermion currents, Dirac equation would guarantee an outcome of zero. For example,

$$\begin{aligned} & \bar{\psi}(p_{e^+})\gamma_\mu\psi(p_{e^-})p_Z^\mu = \bar{\psi}(p_{e^+})\gamma_\mu\psi(p_{e^-})(p_{e^+}^\mu + p_{e^-}^\mu) \\ =& \bar{\psi}(p_{e^+})\gamma_\mu\psi(p_{e^-})p_{e^+}^\mu + \bar{\psi}(p_{e^+})\gamma_\mu\psi(p_{e^-})p_{e^-}^\mu = 0. \end{aligned} \tag{2.89}$$

Therefore the non-vanishing term in the propagator is proportional to the metric tensor $g^{\mu\nu}$, which will allow the current to directly Lorentz-contract with the HVV interaction tensor. When a propagator is attached to other than a massless current, as occurs in the $gg \to ZH$ amplitudes (see Fig. 3.1), the full tensor structure of the vector boson propagator must be preserved.

The denominator of propagators as part of an event generator has been discussed in Section 2.1.3.

2.3.4 Interaction Vertices and Assembling of the Matrix Elements

Vector and axial currents can be either left- and right-handed, and the current of each fermion flavor couple to the Z boson with its own strength,

$$\begin{aligned}
g_V^{Zl_Ll_L} &= \sin^2\theta_W, & g_V^{Zl_Rl_R} &= \sin^2\theta_W - \frac{1}{4},\\
g_A^{Zl_Ll_L} &= 0, & g_A^{Zl_Rl_R} &= -\frac{1}{4},\\
g_V^{Zu_Lu_L} &= -\frac{2}{3}\sin^2\theta_W & g_V^{Zu_Ru_R} &= \frac{1}{4} - \frac{2}{3}\sin^2\theta_W,\\
g_A^{Zu_Lu_L} &= 0, & g_A^{Zu_Ru_R} &= \frac{1}{4},\\
g_V^{Zd_Ld_L} &= \frac{1}{3}\sin^2\theta_W, & g_V^{Zd_Rd_R} &= -\frac{1}{4} + \frac{1}{3}\sin^2\theta_W,\\
g_A^{Zd_Ld_L} &= 0, & g_A^{Zd_Rd_R} &= -\frac{1}{4}.
\end{aligned} \tag{2.90}$$

Because γ^5 can always be treated as part of the left or right projection operator, currents do not need to be considered vector or axial, but only left or right, and the couplings $(g_V^{Zff} - g_A^{Zff}\gamma^5)$ may therefore be reduced to $g_L^{Zff}\frac{\mathbf{1}-\gamma^5}{2} + g_R^{Zff}\frac{\mathbf{1}+\gamma^5}{2}$, with

$$\begin{aligned}
g_L^{Zll} &= \sin^2\theta_W - \frac{1}{2}, & g_R^{Zll} &= \sin^2\theta_W,\\
g_L^{Zuu} &= -\frac{2}{3}\sin^2\theta_W + \frac{1}{2}, & g_R^{Zuu} &= -\frac{2}{3}\sin^2\theta_W,\\
g_L^{Zdd} &= \frac{1}{3}\sin^2\theta_W - \frac{1}{2}, & g_R^{Zdd} &= +\frac{1}{3}\sin^2\theta_W.
\end{aligned} \tag{2.91}$$

It is also useful to define

$$
\begin{aligned}
g_V^{Zll} =& g_V^{Zl_Ll_L} + g_V^{Zl_Rl_R}, & g_A^{Zll} =& g_A^{Zl_Ll_L} + g_A^{Zl_Rl_R}, \\
g_V^{Zuu} =& g_V^{Zu_Lu_L} + g_V^{Zu_Ru_R}, & g_A^{Zuu} =& g_A^{Zu_Lu_L} + g_A^{Zu_Ru_R}, \\
g_V^{Zdd} =& g_V^{Zd_Ld_L} + g_V^{Zd_Rd_R}, & g_A^{Zdd} =& g_A^{Zd_Ld_L} + g_A^{Zd_Rd_R},
\end{aligned} \tag{2.92}
$$

which will be useful in Chapter 3.

The tensor of HVV interaction is rank-2. The a_1 and a_2 terms are easy to obtain, and the rank-4 antisymmetric tensor in the a_3 term can take a compact form,

$$
\epsilon_{\alpha\beta\mu\nu} = \frac{1}{12}\big[(\alpha-\beta)(\alpha-\mu)(\alpha-\nu)(\beta-\mu)(\beta-\nu)(\mu-\nu)\big], \tag{2.93}
$$

$$
\text{with} \quad \epsilon_{0123} = 1, \tag{2.94}
$$

which allows $\epsilon_{\alpha\beta\rho\sigma} p_{Z^*}^{\rho} p_Z^{\sigma}$ to be easily implemented.

Putting everything together, the helicity amplitude for the $e^+e^- \to Z^* \to ZH \to \ell^-\ell^+ b\bar{b}$ process at leading order is

$$
\begin{aligned}
&\mathrm{i}\mathscr{M}_{e^+e^-\to Z^*\to ZH\to \ell^-\ell^+ b\bar{b},\,\mathrm{LO}} \\
=&\mathrm{i}\frac{2M_Z}{v}\, g_{L/R}^{Zll}\, J_{L/R}^{\mu}(p_{e^+}, p_{e^-})\, \mathrm{i}\frac{2M_Z}{v}\, g_{L/R}^{Zll} J_{L/R}^{\nu}(p_{\ell^-}, p_{\ell^+}) \\
\times&\mathrm{i}\frac{M_b}{v} \times \begin{cases} \left[\ \kappa\langle b\bar{b}\rangle + \mathrm{i}\tilde{\kappa}(\mathrm{i}\langle b\bar{b}\rangle)\ \right] & \text{if } b \text{ is left-handed} \\ \left[\ \kappa[b\bar{b}] + \mathrm{i}\tilde{\kappa}(-\mathrm{i}[b\bar{b}])\ \right] & \text{if } b \text{ is right-handed} \end{cases}
\end{aligned}
$$

$$\times \frac{\mathrm{i}}{v}(a_1 g_{\mu\nu} m_H^2 - a_2 p_{V,\mu} p_{V^*,\nu} - a_3 \epsilon_{\alpha\beta\mu\nu} p_{Z^*}^{\alpha} p_Z^{\beta})$$

$$\times \frac{-\mathrm{i}}{p_{Z^*}^2 - m_Z^2 + \mathrm{i} m_Z \Gamma_Z} \frac{-\mathrm{i}}{p_Z^2 - m_Z^2 + \mathrm{i} m_Z \Gamma_Z} \frac{\mathrm{i}}{p_H^2 - m_H^2 + \mathrm{i} m_H \Gamma_H}. \tag{2.95}$$

2.4 Calculating Matrix Elements using Spinor-Helicity Formalism

One compact way to express matrix element is the spinor-helicity formalism, whose review can be found in, e.g. Ref.[34, 41, 42]. In this formalism, the entire structure involving spinors and Lorentz indices of a helicity amplitude can be expressed as a rational expression of only the spinor products as defined in Eqs. (2.64) and (2.65).

The notations of spinors in the spinor-helicity formalism are consistent with those of the spinor products defined in Eqs. (2.64) and (2.65) – breaking the spinor products apart,

$$\psi(p, h = L) = u_-(p) = v_+(p) \equiv |p] \tag{2.96}$$

$$\psi(p, h = R) = u_+(p) = v_-(p) \equiv |p\rangle \tag{2.97}$$

$$\bar{\psi}(p, h = L) = \overline{u_-}(p) = \overline{v_+}(p) \equiv \langle p| \tag{2.98}$$

$$\bar{\psi}(p, h = R) = \overline{u_+}(p) = \overline{v_-}(p) \equiv [p| \quad . \tag{2.99}$$

Similarly, the currents can be written with Lorentz indices sandwiched between spinors.

$$J^{\mu}_{V,L}(p_i, p_j) \equiv \langle p_i|\gamma^{\mu}|p_j] \quad , \tag{2.100}$$

$$J^{\mu}_{V,R}(p_i, p_j) \equiv [p_i|\gamma^{\mu}|p_j\rangle \quad , \tag{2.101}$$

$$J^{\mu}_{A,L}(p_i, p_j) \equiv \langle p_i|\gamma^{\mu}|5|p_j] \quad , \tag{2.102}$$

$$J^{\mu}_{A,R}(p_i, p_j) \equiv [p_i|\gamma^{\mu}|5|p_j\rangle \tag{2.103}$$

Of course, an arbitrary number of γ-matrices can be sandwiched between a pair of spinors to form the Dirac structure of a fermion line in a matrix element with certain helicities.

The polarization vectors for massless vector bosons are

$$\varepsilon^{\mu}_{+}(k) = -\frac{\langle q|\gamma^{\mu}|k]}{\sqrt{2}\langle qk\rangle} \quad , \tag{2.104}$$

$$\varepsilon^{\mu}_{-}(k) = -\frac{[q|\gamma^{\mu}|k\rangle}{\sqrt{2}[qk]} \quad , \tag{2.105}$$

where q is an arbitrary massless reference momentum as long as $\langle qk\rangle \neq 0$ and $[qk] \neq 0$.

The algebra for Dirac matrices can be found in, e.g. Appendix A3 and A4 of Ref. [43], and commonly used identities in the spinor-helicity formalism can be found in, e.g. Chapter 50 and 60 of Ref.[34]. The matrix elements of the VH processes expressed in the spinor-helicity formalism are constructed in the symbolic manipulation language FORM [44] with the SPINNEY package [45].

2.5 Other Technical Aspects

2.5.1 Regarding Incoming Particle Beams

I have so far omitted the discussion on the incoming particle beams. For proton-proton collisions, whose cross section is expressed in Eq. (2.1), parton distribution functions (PDF's) need to be invoked. For each incoming proton beam, its PDF determines the probability for finding a parton with certain flavor and certain momentum fraction at given energy scale (called factorization scale, or μ^2_{Fac}). The PDF is measured experimentally, and is supplied by various groups worldwide in the form of data tables. For the collision with two proton beams, as taking place on the LHC, the center of mass energy of the colling protons $\sqrt{s}$ is known. μ^2_{Fac} is set in the event generator, usually at or near the energy scale of the concerned scattering process. For the VH production, $\mu_{\text{Fac}} = m_{VH}$ as adopted, which is the invariant mass of the V boson and the Higgs boson system, which is also the total invariant mass of the decay products of the V boson and the Higgs boson. Other options of μ^2_{Fac} are also available in the JHUGEN event generator. The only two degrees of freedom are then the momentum fractions $x_{1,2}$ of the incoming partons. $x_{1,2}$ can usually be sampled simply by two uniformly distributed random numbers $y_{1,2} \in [0, 1]$, but can also be sampled using importance sampling (see Section 2.1.3) so that the resulted invariant mass of the entire event roughly follows the expected distribution of the process, allowing the event generation to be slightly more efficient. For example, in the VH production, the cross section grows from 0 rapidly as $m_{VH} = \sqrt{\hat{s}} = \sqrt{sx_1x_2}$ approaches the sum of V mass and H mass $m_V + m_H$ (called threshold energy of the process), and

then is expected to decrease roughly as $\frac{1}{\sqrt{\hat{s}}}$, as the example shown in Fig. 2.3.

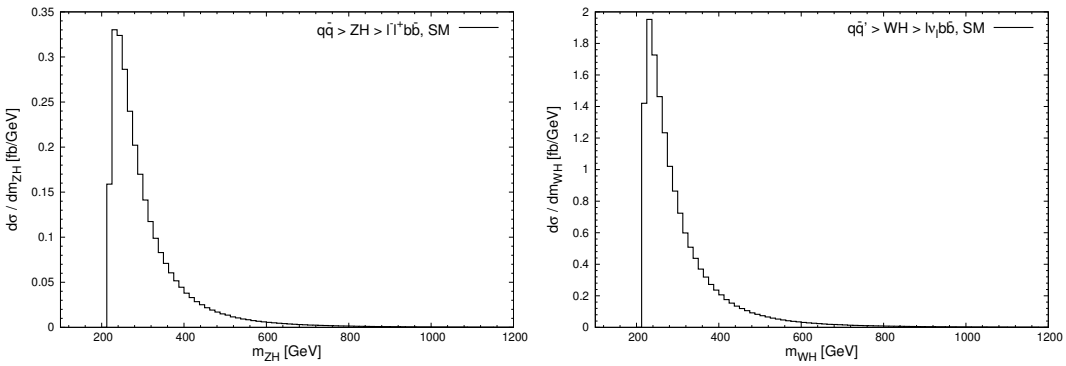

Figure 2.3: Distribution of m_{ZH} for simulated $q\bar{q} \to ZH \to \ell^-\ell^+ b\bar{b}$ events at 14 TeV, and that of m_{WH} for simulated $q\bar{q}' \to WH \to l\nu_l b\bar{b}$ events.

Define

$$\eta_{\min} = \frac{m_H + m_V - 5\Gamma_V}{\sqrt{s}}, \tag{2.106}$$

which is the minimum fraction of collider energy considered for the ZH production. The factor of 5 is arbitrary, which controls how far short of the threshold be considered due to finite width of the Z boson. Further define

$$z = \frac{1}{1 - \eta_{\min}}, \tag{2.107}$$

$$Y_{\min} = \ln\left|\frac{z-1}{z-y_1}\right| \tag{2.108}$$

$$Y_{\max} = -\ln\left|\frac{z-1}{z-y_1}\right| \tag{2.109}$$

$$\text{and} \quad Y = Y_{\min} + y_2(Y_{\max} - Y_{\min}). \tag{2.110}$$

$x_{1,2}$ can be generated via the transform

$$y_1 \to x_1 = \frac{z-1}{z-y_1} e^{Y} \tag{2.111}$$

$$y_2 \to x_2 = \frac{z-1}{z-y_1} e^{-Y}. \tag{2.112}$$

The Jacobian facilitating the transform

$$\mathrm{d}x_1 \mathrm{d}x_2 = \mathbf{J}_{x_{1,2}}(y_1, y_2) \mathrm{d}y_1 \mathrm{d}y_2 \tag{2.113}$$

is

$$\mathbf{J}_{x_{1,2}}(y_1, y_2) = \begin{pmatrix} \frac{\partial x_1}{\partial y_1} & \frac{\partial x_1}{\partial y_2} \\ \frac{\partial x_2}{\partial y_1} & \frac{\partial x_2}{\partial y_2} \end{pmatrix} = 2\frac{(z-1)^2}{(z-y_1)^3}(Y_{\max} - Y_{\min}). \tag{2.114}$$

Once $x_{1,2}$ are generated, they can be fed, along with μ^2_{Fac}, to a PDF data table and obtain its value for each of the proton beams. In JHUGEN, LHAPDF 6 [46] is used to interface the event generator with different PDF sets.

Furthermore, $x_{1,2}$ can be used to produce the Lorentz transformation along the beam (z) axis that boosts the event momenta from the center-of-mass frame to the laboratory frame with

$$\beta = \frac{x_2 - x_1}{x_2 + x_1} \quad \text{and} \quad \gamma = \frac{x_2 + x_1}{2\sqrt{x_1 x_2}}. \tag{2.115}$$

All of the initial- and final-state helicities in the VH production in JHUGEN are determined by random numbers. Although the helicities are usually not directly observable, electron and positron beams can be polarized by certain amount at proposed lepton colliders such as the International Linear Collider

(ILC) [47] and the Circular Electron-positron Collider (CepC) [48]. In JHUGEN, each of the colliding beams can be polarized by any percentage to certain helicity.

2.5.2 Writing Weighted and Unweighted Events

For proton-proton collisions, once the momentum fractions, four-momenta, helicities, and flavors[2] of an event is generated, and assuming that the momenta pass the kinematic selection, they can be applied to the integrand of Eq. (2.1) and obtain the weight of the event

$$\text{Weight}_{pp} = \frac{1}{\hat{s}}\text{PDF}_a\text{PDF}_b|\mathscr{M}_{ab}|^2\text{PS}. \tag{2.116}$$

For electron-positron collisions, the above expression simplifies to

$$\text{Weight}_{e^-e^+} = \frac{1}{s}|\mathscr{M}|^2\text{PS}. \tag{2.117}$$

JHUGEN presents the results of a simulation in two forms – histograms, and Les Houches event files [49].

The histograms are produced by feeding the final-state momenta, which are observed, to a subroutine that computes the kinematic variables, and by adding the associated weight into the bins where the values of the kinematic variables belong. Other than those in Chapter 5, the kinematic distributions in this thesis are presented with histograms created by JHUGEN. For the VH production, the built-in histograms in JHUGEN are for m_{VH}, m_V, m_H, p_V^{T}, p_{T}^H, $\cos\theta_1$, $\cos\theta_2$, ϕ, among which the angles are defined in Fig. 1.2.

[2] In the case where multiple decay channels are considered, a random number is used to decide which channel takes place in a certain event.

The Les Houches event files store events out of a simulation in a list. Each event in the list contains the particle identities, their associated four-momenta, weight of the event, and other relevant information such as helicities QCD colors, etc. While the weighted events are an immediate product of the event generator, unweighted events better resemble the hard process in high energy collisions, and are easier to be further processed for detector simulation and analysis to predict the outcome of a given theory. All of the unweighted events have the same weight$= 1$, but they occur according to the distribution of their weight. To generate unweighted events for proton-proton collisions,

- a first run of the event generator surveys the entire phase space and search for the maximum weight among all the events. This maximum weight can then be multiplied by a factor slightly greater than 1, so that no weight in the simulated process will exceed this value. As a result, one maximum weight for each of the incoming parton combination is stored.

- In the second run of the generator, one uniformly distributed random number will be used to select the parton combination, and each combination will be selected with the probability proportional to its maximum weight.

- Then the generator will generate an event with the selected parton combination.

- At last, another uniformly distributed random number between 0 and 1 will be compared to the ratio of the event weight and the maximum weight stored. If the former is greater than the latter, the event is discarded; and otherwise the event is written down or fed to the histograms with

weight $= 1$. By doing this, whether an event is kept is randomly decided, and the probability of the event being kept is proportional to its weight.

For electron-positron collisions, the steps regarding parton combination is omitted.

It is usually an option to treat multiple events as one and average or sum their weights. This is almost always done treating QCD colors, as they are not observable. In doing so, the average of the initial-state and the sum over the final-state are taken. Although not implemented for the VH processes in JHUGEN, helicities are usually treated in the same way, where the helicities of the incoming partons are averaged and those of the outgoing are summed. The combinations of incoming partons are often summed as well, as implemented for the weighted events in JHUGEN.

2.5.3 Event Selection

During event generation, event selection (also called kinematic cuts, or simply cuts) are performed each time when a set of four-momenta of an event is generated. The momenta are fed into a subroutine which computes the kinematic variables based on which the cuts are performed. If the selection criteria are not met, the set of momenta is discarded. The most common kinematic cuts are performed on the invariant masses of certain final-state particle combinations, the transverse momenta p_{T} of the final-state particles, as well as that of certain combination of two or more final-state particles, and the pseudorapidity η of the final-state particles. The p_{T} and η cuts are usually due to the energy resolution and geometry of the particle detector of the colliding

experiment. For example, when $|\eta|$ is beyond certain value, the particle would travel too close to the beamline and thus miss the component of the detector designed for its type. Another reason for kinematic cuts is to improve the physics analysis at the cost of utilizing less available event. For example, if the signal of a physical process and its background tend to be separated by an invariant mass, as in the case of Section 3.2.2, events with an invariant mass greater or smaller than certain cut value can be selected so that the selected events enjoy a greater signal-to-background ratio.

When the number of event of certain process is scarce, the utilization of all the available event is desired, and the method of matrix element likelihood approach (MELA) can be employed. Although beyond the scope of this chapter, JHUGEN provides the MELA tools for each of the processes it simulates. Some of the applications of MELA are presented in Ref. [35]. In Section 3.2.2 and Section 3.2.6, some of the applications of the matrix-element-based kinematic variables will be presented.

2.6 Collider Phenomenology

Many of the results of ZH at leading order have been presented in Ref. [35]. These results were produced by the event generator with PROCESS $= 50$ and the MELA tools of JHUGEN. In this section I present the validation of the ZH production simulated with with PROCESS $= 51$, as well as a few results not presented in Ref. [35]. The validation is done by overlaying the same distributions produced by PROCESS $= 50$ and 51 in the same figure, and having them adjusted to the same normalization according to the

cross sections calculated by PROCESS = 51. The distributions produced by PROCESS = 50 were taken from Ref. [35] with the tool EASYNDATA [50].

2.6.1 $q\bar{q} \to ZH$ at Leading Order

In Fig. 2.4, the theoretical uncertainties of the $q\bar{q} \to ZH$ simulation at leading order is presented. The theoretical uncertainty mainly consists of that from different PDF sets, and that from the varying energy scale of the calculation. The PDF sets used in this evaluation are CT14NNLO [51], MSTW2008LO90CL [52], and NNPDF31_LO_AS_0118 [53]. The energy scale most relevant to this simulation is the factorization scale μ^2_{Fac} used by the PDF, and has been set to $\mu_{\text{Fac}} = m_{ZH}$. To evaluate the uncertainty due to this scale, the simulation is repeated with $\mu_{\text{Fac}} = 2m_{ZH}$ and $\mu_{\text{Fac}} = m_{ZH}/2$. The cross section varies by

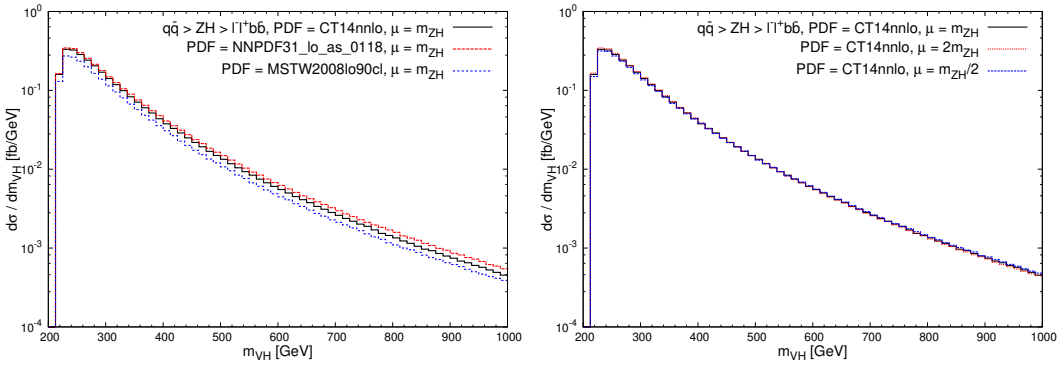

Figure 2.4: m_{ZH} distribution for simulated $q\bar{q} \to Z^* \to ZH \to \ell^-\ell^+ b\bar{b}$ events at 14 TeV with SM, created with three PDF sets (left) as well as using three factorization scales (right).

approximately 13% with the selected PDF sets, and 3% with the scale.

In Fig. 2.5, the distributions of m_{ZH}, $\cos\theta_1$, $\cos\theta_2$ and Φ from proton-proton collision at $\sqrt{s} = 14$ TeV assuming Standard Model (SM) and pseudoscalar are presented on top of those presented in Ref. [35].

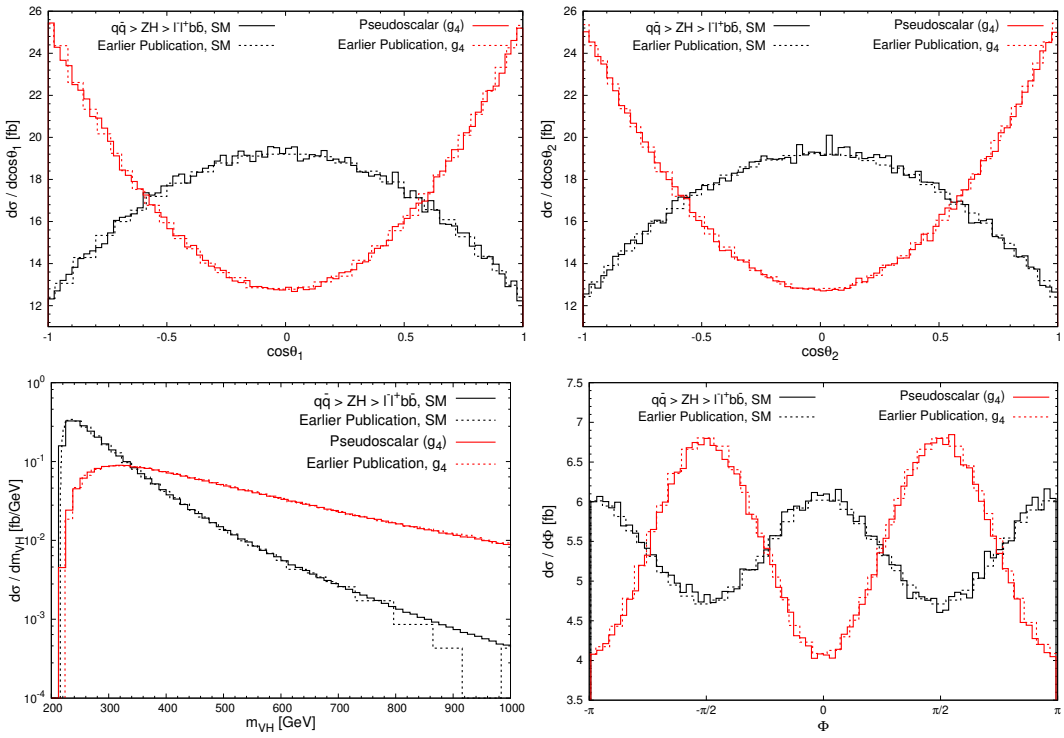

Figure 2.5: Selected kinematic distributions for simulated $q\bar{q} \to Z^* \to ZH \to \ell^-\ell^+ b\bar{b}$ events at 14 TeV with SM or with H being a pseudoscalar, in comparison with Ref. [35].

The discussion of the VH production involving anomalous couplings in proton-proton scattering is left to Chapter 3, where the $gg \to ZH$ contribution is included. The phenomenological results of the $q\bar{q} \to Z^* \to ZH$ process can be found in Ref. [35].

2.6.2 $e^-e^+ \to ZH \to \ell^-\ell^+ b\bar{b}$ with Anomalous Couplings

When selecting the representative values of anomalous couplings to study, the combinations of g_1, g_2, and g_4 for the HVV couplings, as well as the κ and $\tilde{\kappa}$ for the Htt and Hbb couplings are chosen such that the cross section at

$\sqrt{s} = 250$ GeV is maintained at the SM value, and that

$$|\kappa|^2 + |\tilde{\kappa}|^2 = 1. \tag{2.118}$$

In the Table 2.1, the theoretical scenarios considered are listed with the corresponding coupling constants.

Scenario	g_1	g_2	g_4	κ	$\tilde{\kappa}$	Λ
Standard Model	2	0	0	1	0	–
$g_2(s)$	0	≈ 0.364	0	1	0	1 TeV
Pseudoscalar	0	0	≈ 0.751	0	1	1 TeV
50% pseudoscalar	$\sqrt{2}$	0	$\approx \frac{0.751}{\sqrt{2}}$	$\frac{1}{\sqrt{2}}$	$\frac{1}{\sqrt{2}}$	1 TeV
50% pseudoscalar, with $\pi/2$ relative phase with SM	$\sqrt{2}$	0	$\approx \frac{0.751\ \mathrm{i}}{\sqrt{2}}$	$\frac{1}{\sqrt{2}}$	$\frac{\mathrm{i}}{\sqrt{2}}$	1 TeV

Table 2.1: Coupling constants of theoretical scenarios considered in this section.

Because of the non-renormalizable nature of the operators $g_2 H Z_{\mu\nu} Z^{\mu\nu}$ and $g_4 H Z_{\mu\nu} \tilde{Z}^{\mu\nu}$, the coupling "constants" g_2 and g_4 cannot remain constant at arbitrary high energy, and these "constants" should eventually become energy-dependent form factors. To account for this, the simple ad hoc prescriptions

$$g_2 \ \rightarrow \ g_2(s) = g_2 \frac{\Lambda^2}{\Lambda^2 + s} \quad , \tag{2.119}$$

$$\text{and} \quad g_4 \ \rightarrow \ g_4(s) = g_4 \frac{\Lambda^2}{\Lambda^2 + s} \tag{2.120}$$

are introduced, both of which have been implemented in JHUGEN. The choice of cutoff energy scale $\Lambda = 1\,\text{TeV}$, where beyond-SM physics may emerge, is arbitrary. These prescriptions are introduced in consistence with those in Chapter 3. However, because the electron-positron scattering takes place at constant s, these prescriptions do not alter any kinematic distribution of the scattering process.

In Fig. 2.6, the distributions of $\cos\theta_1$, $\cos\theta_2$ and Φ from simulated events of unpolarized electron-positron collisions at $\sqrt{s} = 250$ GeV assuming Standard Model and pseudoscalar are presented on top of those presented in Ref. [35]. In addition, these distributions with 100% polarized beams are also produced and presented in the same figures.

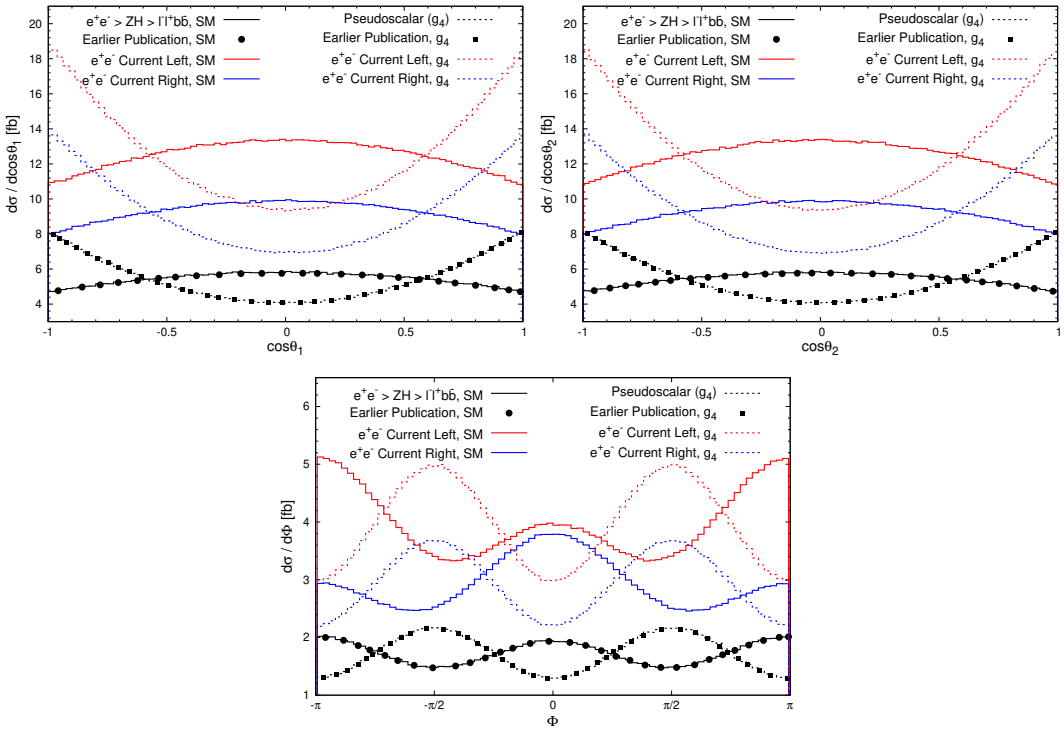

Figure 2.6: Selected kinematic distributions for simulated $e^+e^- \to Z^* \to ZH \to \ell^-\ell^+b\bar{b}$ events at 250 GeV with SM or with H being a pseudoscalar, in comparison with Ref. [35]. In addition, the distributions resulted by 100% polarized electron and positron beams are also shown.

The distributions of $\cos\theta_1$ and $\cos\theta_2$ appear identical, because of the crossing symmetry in the incoming electron current and the outgoing lepton current. For both SM and with pseudoscalar, the effect of the bean polarizations is scaling the cross sections up from the unpolarized collisions. The left-handed current is associated with a larger cross section than the right-handed one, which reflects the fact that the left current couples to the Z boson stronger. The distributions of Φ receive different enhancement from the beam polarizations in SM and with pseudoscalar. In SM, beam polarizations not only increase

the cross section, but also distort the distribution, making the difference between the peaks at $\Phi = 0$ and $\Phi = \pi$ greater. With pesudoscalar, the beam polarizations improve the cross section, but do not change the shape of the distribution.

In Fig. 2.7, the kinematic distributions for simulated $e^-e^+ \to ZH \to \ell^-\ell^+b\bar{b}$ events are presented for selected theoretical scenarios. Among the shown angular distributions, other than that of Φ_1, which is expected to be flat, all are capable of resolving the chosen theoretical scenarios. It is also worth noting that the Higgs boson, which will be produced predominantly via the $Z \to ZH$ vertex on the electron-positron colliders, will travel in the region with low pseudorapidity, giving the detector better chance of detecting its decay product.

2.6.3 Matrix-Element-Based Kinematic Discriminants

Before turning to the chapters of VH production at hadron colliders, it is beneficial to introduce here the matrix-element-based kinematic variables called discriminants, and demonstrate their applications to the $e^-e^+ \to ZH \to \ell^-\ell^+b\bar{b}$ process.

When data is scarce or there is not sufficient data to populate the histograms of the presented kinematic distributions to a desired precision, it is desired to find a single or a smaller set of kinematic variables that are sensitive to specific theoretical scenarios. Fortunately, discriminants are the most optimal observables to separate theoretical scenarios [54]. By directly relating to probabilities, matrix element can be taken advantaged of in constructing

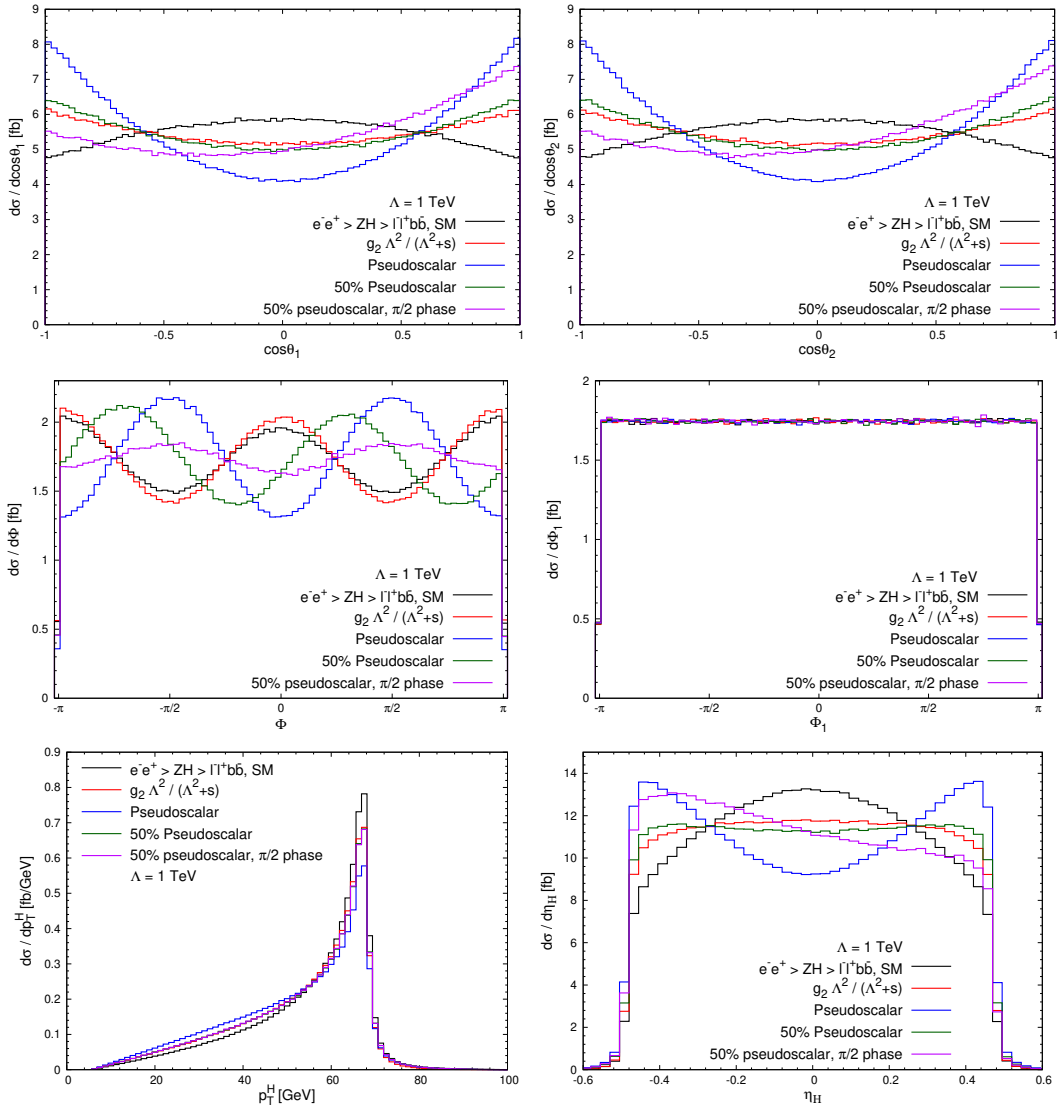

Figure 2.7: Selected kinematic distributions for simulated $e^-e^+ \to ZH \to \ell^-\ell^+b\bar{b}$ events at 250 GeV with selected theoretical scenarios, the coupling constants are listed in Table 2.1.

such variables. Define

$$D_{\mathrm{A/B},\,(e^-e^+}(\{p\}) = \frac{1}{1+\left(\frac{\sigma_B}{\sigma_A}\right)\frac{\mathscr{P}_{A,\,e^-e^+}(\{p\})}{\mathscr{P}_{B,\,(e^-e^+}(\{p\})}}, \tag{2.121}$$

where A and B denotes the theoretical scenarios to be resolved, $\mathscr{P}_A(\{p\})$ and $\mathscr{P}_B(\{p\})$ are the weights of a set of final-state four-momenta $\{p\}$ belonging to an event of the A or B scenario, and the subscripts of e^-e^+ indicates that the discriminant is for $e^-e^+ \to ZH$ events. In fact,

$$\mathscr{P}_{A,\,e^-e^+}(\{p\}) = \sum_{\text{helicities}} \frac{1}{s}|\mathscr{M}_{A,\,e^-e^+}(\{p\})|^2 \mathrm{PS}(\{p\}). \tag{2.122}$$

Because of the shared phase space weight, $\frac{1}{s}$ and $\mathrm{PS}(\{p\})$ get canceled in the fraction. The ratio of the cross sections $\frac{\sigma_B}{\sigma_A}$ serves as a normalization such that A and B have the same total area filling the histograms of the discriminant. In resolving the theoretical scenarios listed in Table 2.1 the cross section ratio can be set to 1. Therefore the discriminant simplifies to

$$D_{\mathrm{A/B},\,e^-e^+}(\{p\}) = \frac{|\mathscr{M}_{B,\,e^-e^+}(\{p\})|^2}{|\mathscr{M}_{A,\,e^-e^+}(\{p\})|^2 + |\mathscr{M}_{B,\,e^-e^+}(\{p\})|^2} \quad \in [0,1]. \tag{2.123}$$

In Fig. 2.8, the distributions of $D_{\mathrm{SM}/g_2,\,e^-e^+}$ are presented for simulated $e^-e^+ \to ZH \to \ell^-\ell^+ b\bar{b}$ events assuming SM and pure g_2. As will be shown in Section 3.2.6, the discriminant $D_{\mathrm{SM}/g_2,\,pp}$, which is applied to events of proton scattering, will provide even better separation between the SM and g_2 contributions.

On the left of Fig. 2.9, the distributions of $D_{\mathrm{SM/Pseudoscalar},\,e^-e^+}$ are presented for simulated $e^-e^+ \to ZH \to \ell^-\ell^+ b\bar{b}$ events at 250 GeV assuming SM

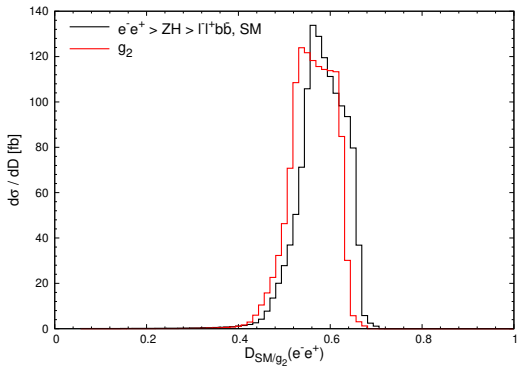

Figure 2.8: $D_{\mathrm{SM}/g_2,\, e^-e^+}$ for simulated $e^-e^+ \to ZH \to \ell^-\ell^+ b\bar{b}$ events at 250 GeV with SM and with pure g_2.

and a few theoretical scenarios involving pseudoscalar.

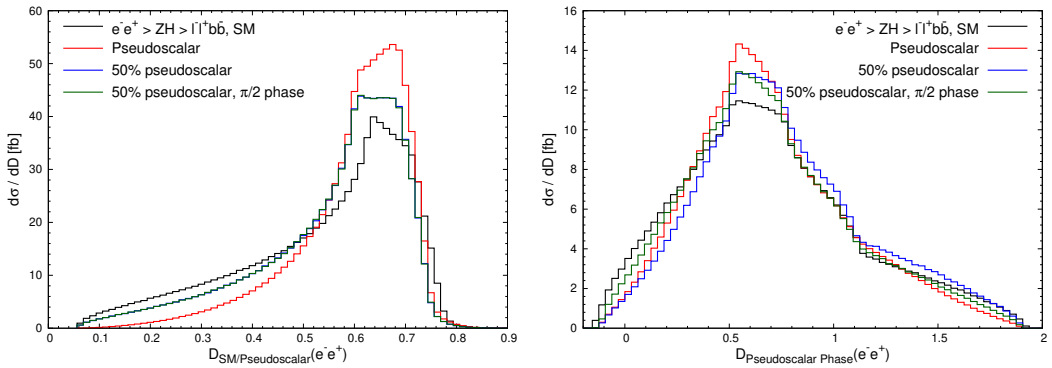

Figure 2.9: $D_{\mathrm{SM/Pseudoscalar},\, e^-e^+}$ for simulated $e^-e^+ \to ZH \to \ell^-\ell^+ b\bar{b}$ events with SM and relevant theoretical scenarios. The coupling constants are listed in Table 2.1.

As shown on the left of Fig. 2.9, most of the scenarios can be separated from one another using the $D_{\mathrm{SM/Pseudoscalar},\, e^-e^+}$ discriminant. However, it has no sensitivity to the relative phase between SM and pseudoscalar contributions. In attempt to gain some sensitivity of the relative phase, the D_{CP} discriminant was introduced in Ref. [35], and I am applying it here as

$$D_{\mathrm{Phase},\, e^-e^+}(\{p\}) \sim \frac{\mathscr{P}_{\mathrm{Interference},\, e^-e^+}(\{p\})}{\mathscr{P}_{\mathrm{Pseudoscalar},\, e^-e^+}(\{p\}) + \mathscr{P}_{\mathrm{SM},\, e^-e^+}(\{p\})}, \tag{2.124}$$

where

$$\mathscr{P}_{\text{Interference}}(\{p\}) \sim 2\Re\big(\mathscr{M}^{*}_{\text{Pseudoscalar}}(\{p\})\mathscr{M}_{\text{SM}}(\{p\})\big). \tag{2.125}$$

The distributions of $D_{\text{SM/Pseudoscalar Phase, } e^-e^+}$ are presented on the right of Fig. 2.9 for simulated $e^-e^+ \to ZH \to \ell^-\ell^+ b\bar{b}$ events with the same theoretical scenarios, and one can observe the difference between 50% pseudoscalar with and without $\pi/2$ relative phase between the SM and pseudoscalar contributions.

Chapter 3

Event Generation and Collider Phenomenology of the $gg \to ZH$ Production

Higgs boson production in association with a Z boson also takes place in gluon fusion, whose leading order Feynman diagrams are shown in the figure below.

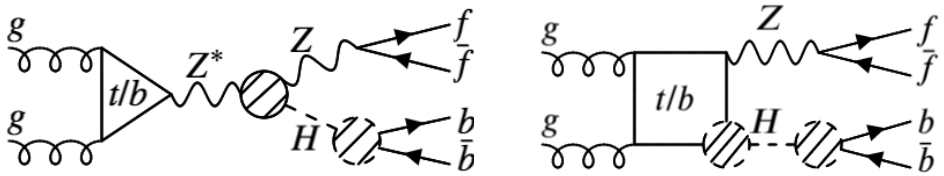

Figure 3.1: Leading order Feynman diagrams of the $gg \to ZH \to \ell^-\ell^+ b\bar{b}$ process. The solid shaded bulb indicates the HZZ interaction with anomalous couplings, and the shaded bulbs with dashed contour indicate the Hqq interactions with anomalous couplings.

Although the leading order matrix element of the $gg \to ZH$ process is

proportional to g_S^2, making it the next-to-next-to-leading order in the proton-proton process; as Ref. [55] pointed out, the large gluon-gluon parton luminosity makes the $gg \to ZH$ production numerically relevant in the study of $q\bar{q} \to ZH$ even at leading order. Ref. [55] also pointed out that with suitable kinematic requirements, e.g. at high m_{ZH} or p_T^H, the relative contribution of $gg \to ZH$ can be enhanced. Furthermore, as I will demonstrate, the anomalous couplings considered in this thesis have different effects in the $q\bar{q}$- and gg-initiated processes, and the study of both simultaneously can provide additional means of determining these anomalous couplings.

The left diagram of Fig. 3.1 is commonly referred as the triangle diagram, and the right diagram as the box diagram. Each "diagram" refers to the sum of diagrams with the same shape of fermion loop – in both the triangle and box diagrams, the loop momentum can be either clockwise or counterclockwise; and in the box diagram, two gluons, one Z boson and one Higgs boson can be attached to the fermion loop with different permutations. The non-vanishing box diagrams of the $gg \to ZH$ processes are listed in Fig. 3.2.

As shown in Fig. 3.1, the bosonic anomalous couplings can be present only in the triangle diagram, and the fermionic anomalous coupling can be present in both the triangle and the box diagrams. Four more key features of the triangle diagrams will be found out:

i. The vector coupling of the triangular fermion loop to the Z boson leads to zero contribution to the amplitude, and only the axial-vector coupling makes nonzero contribution, a consequence of Furry's Theorem [56]. As a result, a off-shell photon cannot be coupled to the triangular fermion

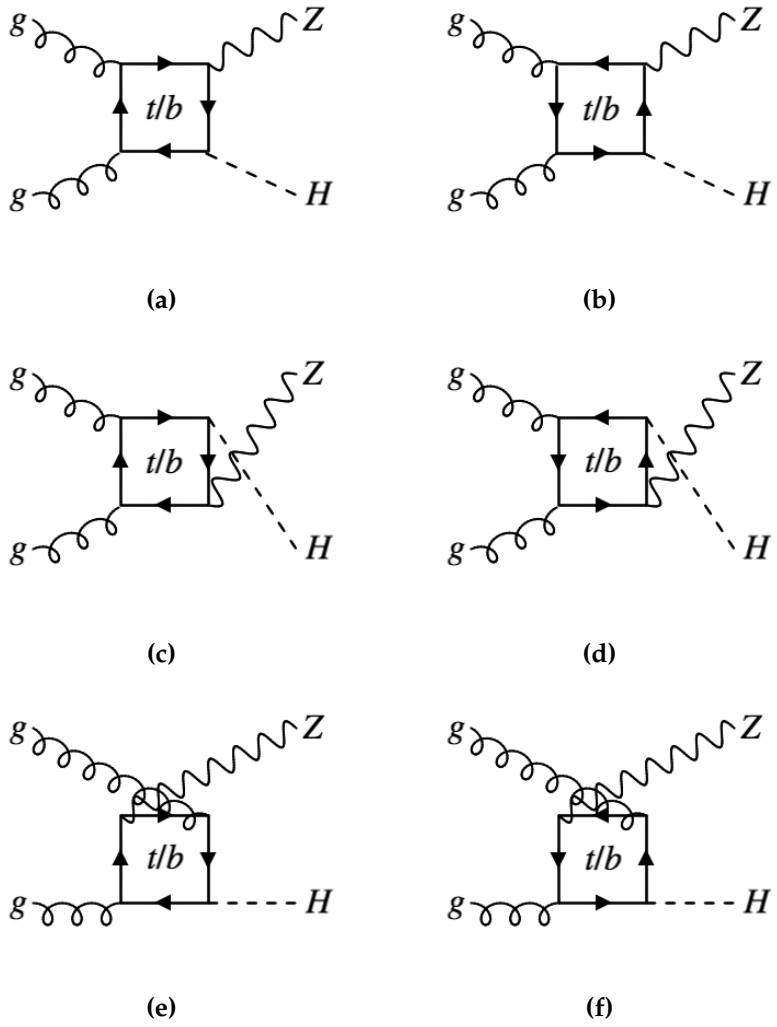

Figure 3.2: Non-vanishing box diagrams of the $gg \to ZH$ processes.

loop.

ii. The triangle diagram is nonzero only when both gluons have the same polarization, namely, when the expressions of both gluon polarization vectors take Eq. (2.104) or (2.105) at the same time, each with the reference momentum being that of the other gluon.

iii. The g_2 coupling leads to zero contribution to the triangle diagram, which is due to the cancellation of the a_1 and a_2 tensor structures in Eq. (1.29).

iv. The g_4 coupling leads to zero contribution to the triangle diagram, which is solely due to the tensor structure of the a_3 term in Eq. (1.29).

The leading order Feynman diagrams of $gg \to ZH$ processes are one-loop induced, and their sum expected to be finite. Therefore all of the techniques of constructing a leading order event generator introduced in Chapter 2 apply, with the exception of the calculation in the one-loop amplitudes.

3.1 Calculating One-Loop Matrix Elements

Working with dimensional regularization in dimension $\mathrm{Dim} = 4 - 2\epsilon$, the amplitude of a triangle diagram with the loop momentum in one direction is

$$\begin{aligned} i\mathscr{M}_{\triangleright} = {} & \varepsilon^{\alpha}_{\lambda_1}(p_{g_1})\, \varepsilon^{\beta}\lambda_2(p_{g_2})\, \left(\mathscr{M}^{\mu}_{Z^*\to ZH\to \ell^-\ell^+ b\bar{b}}\right)\, \mu^{2\epsilon}_{\mathrm{Ren}}(-1) \\ & \times \int \frac{d^{\mathrm{Dim}}k}{(4\pi)^{\mathrm{Dim}}} \mathrm{Tr}\Big[(\mathrm{i}g_S t^b)\gamma_\beta \frac{\mathrm{i}(\not{k} - \not{p}_{g_2} + m_f)}{(k-p_{g_2})^2 - m_f^2} \big(\mathrm{i}\frac{2m_Z}{v}\gamma_\mu (g_V^{Zff} - g_A^{Zff}\gamma^5)\big) \\ & \times \frac{\mathrm{i}(\not{k} + \not{p}_{g_1} + m_f)}{(k+p_{g_1})^2 - m_f^2} (\mathrm{i}g_S t^a)\gamma_\alpha \frac{\mathrm{i}(\not{k} + m_f)}{k^2 - m_f^2}\Big] \end{aligned} \tag{3.1}$$

$$= 4\pi\alpha_S \frac{2m_Z}{v} \mathrm{Tr}[t^a t^b]\, \varepsilon^\alpha_{\lambda_1}(p_{g_1})\, \varepsilon^\beta \lambda_2(p_{g_2})\, \left(\mathscr{M}^\mu_{Z^*\to ZH\to \ell^-\ell^+ b\bar{b}}\right) \mu^{2\epsilon}_{\mathrm{Ren}}$$

$$\times \int \frac{d^{\mathrm{Dim}}k}{(4\pi)^{\mathrm{Dim}}} \frac{1}{(k-p_{g_2})^2 - m_f^2} \frac{1}{(k+p_{g_1})^2 - m_f^2} \frac{1}{k^2 - m_f^2}$$

$$\times \Big(g_V^{Zff} \mathrm{Tr}\big[\gamma_\beta (\not{k} - \not{p}_{g_2}) \gamma_\mu (\not{k} + \not{p}_{g_1}) \gamma_\alpha \not{k}\big]$$

$$- g_A^{Zff} \mathrm{Tr}\big[\not{k} - \not{p}_{g_2}) \gamma_\mu \gamma^5 (\not{k} + \not{p}_{g_1}) \gamma_\alpha \not{k}\big] \Big) \quad , \tag{3.2}$$

where $g_{1,2}$ denotes the two scattering gluons with $\lambda_{1,2}$ being their polarizations; $\mathscr{M}^\mu_{Z^*\to ZH\to \ell^-\ell^+ b\bar{b}}$ is the decay chain of the Z^* boson with its Lorentz index μ, which is shared with the $q\bar{q} \to ZH$ process (see Fig. 1.1); μ_{Ren} is the renormalization scale; (-1) is for the fermion loop; $f = b, t$; and g_V^{Zff} and g_A^{Zff} are the vector and axial-vector coupling constants respectively of the Z boson to fermion f, defined in Eq. (2.92). The integral of loop momentum k is over its entire phase space, which takes into account all the path the virtual gluon can take.

The representative amplitude of Fig. 3.2(a) is

$$i\mathscr{M}_\square = \varepsilon^\alpha_{\lambda_1}(p_{g_1})\, \varepsilon^\beta \lambda_2(p_{g_2})\, \left(\mathscr{M}^\mu_{Z^*\to ZH\to \ell^-\ell^+ b\bar{b}}\right) \mu^{2\epsilon}_{\mathrm{Ren}} (-1)$$

$$\times \int \frac{d^{\mathrm{Dim}}k}{(4\pi)^{\mathrm{Dim}}} \mathrm{Tr}\Big[(\mathrm{i}g_S t^b) \gamma_\beta \frac{\mathrm{i}(\not{k} - \not{p}_{g_2} + m_f)}{(k-p_{g_2})^2 - m_f^2} (-\mathrm{i}\frac{m_f}{v}) \frac{\mathrm{i}(\not{k} + \not{p}_{g_1} - \not{p}_Z + m_f)}{(k+p_{g_1}-p_Z)^2 - m_f^2}$$

$$\times (\mathrm{i}\frac{2m_Z}{v} \gamma_\mu (g_V^{Zff} - g_A^{Zff}\gamma^5)) \frac{\mathrm{i}(\not{k} + \not{p}_{g_1} + m_f)}{(k+p_{g_1})^2 - m_f^2} (\mathrm{i}g_S t^a) \gamma_\alpha \frac{\mathrm{i}(\not{k} + m_f)}{k^2 - m_f^2} \Big] \tag{3.3}$$

$$= 4\pi\alpha_S \frac{m_f}{v} \frac{2m_Z}{v} \mathrm{Tr}[t^a t^b]\, \varepsilon^\alpha_{\lambda_1}(p_{g_1})\, \varepsilon^\beta \lambda_2(p_{g_2})\, \left(\mathscr{M}^\mu_{Z^*\to ZH\to \ell^-\ell^+ b\bar{b}}\right) \mu^{2\epsilon}_{\mathrm{Ren}}$$

$$\times \int \frac{d^{\mathrm{Dim}}k}{(4\pi)^{\mathrm{Dim}}} \frac{1}{(k-p_{g_2})^2-m_f^2} \frac{1}{(k+p_{g_1}-p_Z)^2-m_f^2} \frac{1}{(k+p_{g_1})^2-m_f^2}$$

$$\times \frac{1}{k^2-m_f^2} \Big(g_V^{Zff} \mathrm{Tr}\big[\gamma_\beta(\not{k}-\not{p}_{g_2})(\not{k}+\not{p}_{g_1}-\not{p}_Z+m_f)\gamma_\mu(\not{k}+\not{p}_{g_1})\gamma_\alpha \not{k}\big]$$

$$- g_A^{Zff} \mathrm{Tr}\big[\not{k}-\not{p}_{g_2})(\not{k}+\not{p}_{g_1}-\not{p}_Z+m_f)\gamma_\mu\gamma^5(\not{k}+\not{p}_{g_1})\gamma_\alpha \not{k}\big]\Big) \quad , \tag{3.4}$$

in which the notations of Eq. (3.2) still apply.

3.1.1 Passarino-Veltman Tensor Integral Reduction

In calculating the amplitudes in Eq. (3.2) and (3.4), tensor integrals of the form

$$\mathrm{TI}^{\mu_1\mu_2\cdots\mu_N}(m_0,m_1,...,m_n;p_1,...,p_n;\mathrm{Dim})$$

$$\equiv \mu_{\mathrm{Ren}}^{2\epsilon} \int \frac{d^{\mathrm{Dim}}k}{(4\pi)^{\mathrm{Dim}}} \frac{k^{\mu_1}k^{\mu_2}...k^{\mu_N}}{\mathrm{D}(m_0)\mathrm{D}(m_1,p_1)\mathrm{D}(m_2,p_2)...\mathrm{D}(m_n,p_n)}, \tag{3.5}$$

where $0 < N < n$, need to be evaluated. This is achieved by the Passarino-Veltman reduction [57], reviewed in, e.g. Ref. [58], which expresses tensor integrals as the sum of the products of external momentum variables p_i, the metric $g^{\mu\nu}$, and some readily calculated scalar integrals, listed as follows[1]:

$$A_0(m_0;\mathrm{Dim}) = \mu_{\mathrm{Ren}}^{2\epsilon} \int \frac{d^{\mathrm{Dim}}k}{(4\pi)^{\mathrm{Dim}}} \frac{1}{\mathrm{D}(m_0)}, \tag{3.6}$$

$$B_0(m_0,m_1;p_1;\mathrm{Dim}) = \mu_{\mathrm{Ren}}^{2\epsilon} \int \frac{d^{\mathrm{Dim}}k}{(4\pi)^{\mathrm{Dim}}} \frac{1}{\mathrm{D}(m_0)\mathrm{D}(m_1,p_1)}, \tag{3.7}$$

[1]Note that the tensor and scalar integrals in Ref. [58], as well as those in many other references, have omitted a factor of $i\pi^2/(2\pi)^4$, which is not omitted in this thesis.

$$C_0(m_0, m_1, m_2; p_1, p_2; \mathrm{Dim}) = \mu_{\mathrm{Ren}}^{2\epsilon} \int \frac{d^{\mathrm{Dim}}k}{(4\pi)^{\mathrm{Dim}}} \frac{1}{\mathrm{D}(m_0)\mathrm{D}(m_1, p_1)\mathrm{D}(m_2, p_2)}, \tag{3.8}$$

$$D_0(m_0, m_1, m_2, m_3; p_1, p_2, p_3; \mathrm{Dim})$$

$$= \mu_{\mathrm{Ren}}^{2\epsilon} \int \frac{d^{\mathrm{Dim}}k}{(4\pi)^{\mathrm{Dim}}} \frac{1}{\mathrm{D}(m_0)\mathrm{D}(m_1, p_1)\mathrm{D}(m_2, p_2)\mathrm{D}(m_3, p_3)}, \tag{3.9}$$

where

$$\mathrm{D}(m_0) \equiv k^2 - m_0^2 + \mathrm{i}\epsilon, \quad \text{and} \quad \mathrm{D}(m_i, p_i) \equiv (k + p_i)^2 - m_i^2 + \mathrm{i}\epsilon \tag{3.10}$$

are the denominators of propagators in a loop. It should be noted that the p_i variables are defined in Fig. 4.1 of Ref. [58], and I will later identify them with the momenta involved in the $gg \to ZH \to \ell^-\ell^+ b\bar{b}$ process.

The highest rank tensor integral with the most propagators for the $gg \to ZH$ amplitude is

$$\mathrm{TI}^{\mu\nu\rho}(m_0, m_1, m_2, m_3; p_1, p_2, p_3; \mathrm{Dim})$$

$$\equiv \mu_{\mathrm{Ren}}^{2\epsilon} \int \frac{d^{\mathrm{Dim}}k}{(4\pi)^{\mathrm{Dim}}} \frac{k^\mu k^\nu k^\rho}{\mathrm{D}(m_0)\mathrm{D}(m_1, p_1)\mathrm{D}(m_2, p_2)\mathrm{D}(m_3, p_3)} \tag{3.11}$$

because of the four propagators in the fermion loop and the three Lorentz indices associated with two gluons and one Z boson. Consequently, with A, B, C, ... denoting TI with 1, 2, 3, ... propagators respectively, all of the tensor integrals needed for the $gg \to ZH$ process are

$$B^\mu(m_0, m_1; p_1; \mathrm{Dim}) = \mu_{\mathrm{Ren}}^{2\epsilon} \int \frac{d^{\mathrm{Dim}}k}{(4\pi)^{\mathrm{Dim}}} \frac{k^\mu}{\mathrm{D}(m_0)\mathrm{D}(m_1, p_1)}, \tag{3.12}$$

$$B^{\mu\nu}(m_0, m_1; p_1; \mathrm{Dim}) = \mu_{\mathrm{Ren}}^{2\epsilon} \int \frac{d^{\mathrm{Dim}}k}{(4\pi)^{\mathrm{Dim}}} \frac{k^\mu k^\nu}{\mathrm{D}(m_0)\mathrm{D}(m_1, p_1)}, \tag{3.13}$$

$$C^{\mu}(m_0, m_1, m_2; p_1, p_2; \mathrm{Dim}) = \mu_{\mathrm{Ren}}^{2\epsilon} \int \frac{d^{\mathrm{Dim}}k}{(4\pi)^{\mathrm{Dim}}} \frac{k^\mu}{\mathrm{D}(m_0)\mathrm{D}(m_1, p_1)\mathrm{D}(m_2, p_2)}, \tag{3.14}$$

$$C^{\mu\nu}(m_0, m_1, m_2; p_1, p_2; \mathrm{Dim}) = \mu_{\mathrm{Ren}}^{2\epsilon} \int \frac{d^{\mathrm{Dim}}k}{(4\pi)^{\mathrm{Dim}}} \frac{k^\mu k^\nu}{\mathrm{D}(m_0)\mathrm{D}(m_1, p_1)\mathrm{D}(m_2, p_2)}, \tag{3.15}$$

$$C^{\mu\nu\rho}(m_0, m_1, m_2; p_1, p_2; \mathrm{Dim}) = \mu_{\mathrm{Ren}}^{2\epsilon} \int \frac{d^{\mathrm{Dim}}k}{(4\pi)^{\mathrm{Dim}}} \frac{k^\mu k^\nu k^\rho}{\mathrm{D}(m_0)\mathrm{D}(m_1, p_1)\mathrm{D}(m_2, p_2)}, \tag{3.16}$$

$$\begin{aligned} &D^{\mu}(m_0, m_1, m_2, m_3; p_1, p_2, p_3; \mathrm{Dim}) \\ =&\mu_{\mathrm{Ren}}^{2\epsilon} \int \frac{d^{\mathrm{Dim}}k}{(4\pi)^{\mathrm{Dim}}} \frac{k^\mu}{\mathrm{D}(m_0)\mathrm{D}(m_1, p_1)\mathrm{D}(m_2, p_2)\mathrm{D}(m_3, p_3)}, \end{aligned} \tag{3.17}$$

$$\begin{aligned} &D^{\mu\nu}(m_0, m_1, m_2, m_3; p_1, p_2, p_3; \mathrm{Dim}) \\ =&\mu_{\mathrm{Ren}}^{2\epsilon} \int \frac{d^{\mathrm{Dim}}k}{(4\pi)^{\mathrm{Dim}}} \frac{k^\mu k^\nu}{\mathrm{D}(m_0)\mathrm{D}(m_1, p_1)\mathrm{D}(m_2, p_2)\mathrm{D}(m_3, p_3)}, \end{aligned} \tag{3.18}$$

$$\begin{aligned} &D^{\mu\nu\rho}(m_0, m_1, m_2, m_3; p_1, p_2, p_3; \mathrm{Dim}) \\ =&\mu_{\mathrm{Ren}}^{2\epsilon} \int \frac{d^{\mathrm{Dim}}k}{(4\pi)^{\mathrm{Dim}}} \frac{k^\mu k^\nu k^\rho}{\mathrm{D}(m_0)\mathrm{D}(m_1, p_1)\mathrm{D}(m_2, p_2)\mathrm{D}(m_3, p_3)}. \end{aligned} \tag{3.19}$$

The reductions of the tensor integrals above read

$$B^\mu = p_1^\mu B_1, \tag{3.20}$$

$$B^{\mu\nu} = g^{\mu\nu} B_{00} + p_1^\mu p_1^\nu B_{11}, \tag{3.21}$$

$$C^\mu = p_1^\mu C_1 + p_2^\mu C_2, \tag{3.22}$$

$$C^{\mu\nu} = g^{\mu\nu} C_{00} + \sum_{i,j=1}^{2} p_i^\mu p_j^\nu C_{ij}, \tag{3.23}$$

$$C^{\mu\nu\rho} = \sum_{i=1}^{2} (g^{\mu\nu} p_i^\rho + g^{\mu\rho} p_i^\nu + g^{\rho\nu} p_i^\mu) C_{00i} + \sum_{i,j,k=1}^{2} p_i^\mu p_j^\nu p_k^\rho C_{ijk}, \tag{3.24}$$

$$D^\mu = \sum_{i=1}^{3} p_i^\mu D_i, \tag{3.25}$$

$$D^{\mu\nu} = g^{\mu\nu} D_{00} + \sum_{i,j=1}^{3} p_i^\mu p_j^\nu D_{ij}, \tag{3.26}$$

$$D^{\mu\nu\rho} = \sum_{i=1}^{3} (g^{\mu\nu} p_i^\rho + g^{\mu\rho} p_i^\nu + g^{\rho\nu} p_i^\mu) D_{00i} + \sum_{i,j,k=1}^{3} p_i^\mu p_j^\nu p_k^\rho D_{ijk},, \tag{3.27}$$

where the scalar coefficients can be expressed in terms of scalar products of momenta, squared masses, and scalar integrals defined in Eq. (3.9). In determining the scalar coefficients, the following identities will be useful,

$$k p_i = \frac{1}{2}\left[\mathrm{D}(m_i, p_i) - \mathrm{D}(m_0) - f_i\right] \quad , \quad \text{with} \quad f_i \equiv p_i^2 - m_i^2 + m_0^2, \tag{3.28}$$

$$\text{and} \quad g^{\mu\nu} k_\mu k_\nu = k^2 = \mathrm{D}(m_0) + m_0^2 \quad . \tag{3.29}$$

As an example, to determine B_1, $p_{1\mu}$ is multiplied on both sides of Eq. (3.20),

$$p_{1\mu} B^\mu = p_{1\mu} p_1^\mu B_1, \tag{3.30}$$

$$\Rightarrow \quad \mu_{\mathrm{Ren}}^{2\epsilon} \int \frac{d^{\mathrm{Dim}} k}{(4\pi)^{\mathrm{Dim}}} \frac{p_1 k}{\mathrm{D}(m_0) D(\mathrm{m}_1, p_1)} = p^2 B_1, \tag{3.31}$$

$$\Rightarrow \quad \mu_{\mathrm{Ren}}^{2\epsilon} \int \frac{d^{\mathrm{Dim}} k}{(4\pi)^{\mathrm{Dim}}} \frac{\frac{1}{2}\left[\mathrm{D}(m_1, p_1) - \mathrm{D}(m_0) - f_1\right]}{\mathrm{D}(m_0)\mathrm{D}(m_1, p_1)} = p^2 B_1, \tag{3.32}$$

$$\Rightarrow \quad \frac{1}{2}\left[A_0(m_0) - A_0(m_1) - f_1 B_0(m_0, m_1, p_1)\right] = p^2 B_1, \tag{3.33}$$

$$\Rightarrow \quad B_1(m_0, m_1, p_1) = \frac{A_0(m_0) - A_0(m_1) - f_1 B_0(m_0, m_1, p_1)}{2p^2}. \tag{3.34}$$

Similarly, contracting Eq. (3.20)-(3.27) with external momenta and the metric tensor, and solving a linear system of equations for the scalar coefficients, a library for tensor integral reduction can be built. The analytical expressions of the scalar integrals A_0, B_0, C_0, and D_0 are listed in Section 4.3 of Ref. [58], and are implemented in FORTRAN libraries QCDLOOP [59] and COLLIER [60]. It is worth noting that some of the scalar integrals and scalar coefficients carry ultraviolet and/or inferred divergences. The former are listed in Section 4.5 of Ref. [58] and those needed for this thesis can be found in Appendix B of Ref. [61]. For the one-loop $gg \to ZH$ amplitudes, these divergences are expected to cancel and thus do not need any treatment. However, their cancellation can be used to check if mistakes exist in the calculation.

Once the tensor integrals are fully reduced, they can be combined with the Dirac structures to form amplitudes.

3.1.2 Assembling One-Loop Matrix Elements

The amplitudes of the $gg \to ZH \to \ell^-\ell^+ b\bar{b}$ process are implemented in the following steps.

- The fermion triangle and box loops with Lorentz indices for the two gluon and one Z boson uncontracted are first expressed in FORM [44], and their traces are taken in Dim= 4 dimension.

- Then the terms from the above step are grouped according to the power of loop momentum k, with each group of terms being proportional to one of the tensor integrals listed in Eqs. (3.12)-(3.19). At this stage, k does not make explicit appearance in the expression.

- Eqs. (3.20)-(3.27) are then applied and the the tensor integrals are substituted by linear combinations of scalar coefficients.

- The fermion loops with open Lorentz indices are then contracted with the rest parts of the amplitude, namely the polarization vectors of the gluons, the decay chain of $Z^* \to ZH \to \ell^-\ell^+ b\bar{b}$ from the triangle diagrams, and $Z \to \ell^-\ell^+$ and $H \to b\bar{b}$ from the box diagrams.

- The SPINNEY package [45] of FORM is used expressed the $gg \to (\text{triangle} \to Z^*)/\text{box} \to ZH \to \ell^-\ell^+ b\bar{b}$ amplitudes in spinor-helicity formalism, in which the polarization vectors of the gluons are expressed by Eqs. (2.104) and (2.105), the $\ell^-\ell^+$ current by Eqs. (2.100) and (2.101), and the spinor product of $b\bar{b}$ by Eqs. (2.64)-(2.69). SPINNEY is also used to contract any Lorentz indices sandwiched between spinors. In the end, no Lorentz index makes appearance in the expressions of the amplitudes.

- Because in the Dirac structure there is no correlation between the decay chain of $H \to b\bar{b}$ and the rest of the amplitudes, it is multiplied to the amplitudes as an option if the Higgs boson is set to decay to b-quark pair in JHUGEN[2]. Otherwise, one helicity amplitude is needed for each helicity combination of the external particles, each (SM or anomalous)

[2]JHUGEN allows the Higgs boson be produced on-shell, and can have it decay to a pair of vector bosons and their subsequent decay products or a pair of fermions

coupling, and each Feynman diagram (for "the triangle diagram", the loop momentum can be clockwise or counterclockwise, and for "the box diagram", there are six diagrams listed in Fig. 3.2).

- By this stage, all of the p_i momenta appeared in the discussion above have been expressed in terms of momenta of the $gg \to (\text{triangle} \to Z^*)/\text{box} \to ZH \to \ell^-\ell^+ b\bar{b}$ process according to the convention specified in Figure 4.1 of Ref. [58]. For the triangle amplitude in Eq. (3.2),

$$p_1 = p_{g_1}, \quad \text{and} \quad p_2 = p_{g_2}, \tag{3.35}$$

and for the other triangle amplitude,

$$p_1 = p_{g_2}, \quad \text{and} \quad p_2 = p_{g_1}. \tag{3.36}$$

Because all momenta in the spinor-helicity formalism need to be massless, the momenta of the Z^* and Z bosons, appearing in the propagators and anomalous couplings, are expressed as the sum of the massless momenta they attach to,

$$p_{Z^*} = p_{g_1} + p_{g_2} \quad \text{and} \quad p_Z = p_{\ell^-} + p_{\ell^+}. \tag{3.37}$$

For each box diagram in Fig. 3.2, the p_i momenta are expressed as

$$\text{(a):} \quad p_1 = p_{g_1}, \quad p_2 = p_{g_1} - p_{\ell^-} - p_{\ell^+}, \quad p_3 = -p_{g_2}; \tag{3.38}$$

$$\text{(b):} \quad p_1 = p_{g_2}, \quad p_2 = p_{\ell^-} + p_{\ell^+} - p_{g_1}, \quad p_3 = -p_{g_1}; \tag{3.39}$$

$$\text{(c):} \quad p_1 = p_{g_1}, \quad p_2 = p_{\ell^-} + p_{\ell^+} - p_{g_2}, \quad p_3 = -p_{g_2}; \tag{3.40}$$

$$\text{(d):}\quad p_1 = p_{g_2},\quad p_2 = p_{g_2} - p_{\ell^-} - p_{\ell^+},\quad p_3 = -p_{g_1}; \tag{3.41}$$

$$\text{(e):}\quad p_1 = -p_{\ell^-} - p_{\ell^+},\quad p_2 = p_{g_1} - p_{\ell^-} - p_{\ell^+},\quad p_3 = -p_{g_2}; \tag{3.42}$$

$$\text{(f):}\quad p_1 = p_{g_2},\quad p_2 = p_{\ell^-} + p_{\ell^+} - p_{g_1},\quad p_3 = p_{\ell^-} + p_{\ell^+}. \tag{3.43}$$

- The triangle amplitudes are then exported in the format of MATHEMATICA [62], in which the scalar coefficients are further reduced to linear combinations of scalar integrals. When the sum over bottom and top quarks, as well as over the direction of loop momentum, is taken, the the b quark part of the amplitude, where the b quark is treated massless, cancels with the massless terms from the t quark part of the amplitude; and only terms proportional to m_t^2 survive. Here I arrive at the conclusions listed in the first, second, and fourth bullet points at the beginning of this Chapter.

- It is noticed that each pair of amplitudes in Fig. 3.2(a and b), (c and d), and (e and f) shares the same scalar coefficients with the same arguments (expressed as an equivalent set of Mandelstam variables), and thus can be combined and further simplified in FORM.

- Both triangle and box amplitudes are exported in the format of the FORTRAN language, in which JHUGEN is written. While QCDLOOP and COLLIER have both been used to provide and crosscheck the numerical values of the tensor integrals, in the final implementation of the generator, COLLIER is used to supply the generator with the numerical values of both the scalar integrals (for the triangle amplitudes) as well as the scalar

coefficients (for the box amplitudes).

- At last, the sum of the two triangle amplitudes and that of the six box amplitudes are checked to be gauge-invariant explicitly by replacing the polarization vectors of the gluons with the corresponding momentum; and the numerical values of the amplitudes at a few phase space points are crosschecked to machine precision (10-12 digits for double precision) with the values independently calculated by Dr. Markus C. Schulze, another collaborator of the JHUGEN project.

3.2 Collider Phenomenology

3.2.1 $gg \to ZH$ in the Standard Model

The simulation of $gg \to ZH$ by JHUGEN within the Standard Model is validated against existing publication [55], as shown in Fig. 3.3.

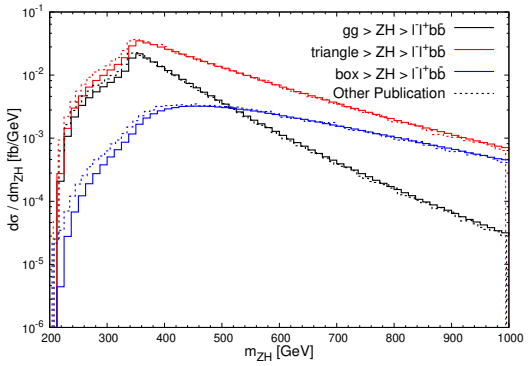

Figure 3.3: The m_{ZH} distribution for simulated $gg \to ZH \to \ell^-\ell^+ b\bar{b}$ events at 14 TeV in SM, in comparison with Ref. [55]. The distributions for the individual diagrams of triangle and box are also shown.

A significant destructive interference between the triangle and box diagrams can be seen. Both contributions from the triangle and the box diagrams peak at around $2m_t \approx 345\,\text{GeV}$, due to the top quark in the fermion loop. The slight deviation at low m_{ZH} in the comparison may be attributed to the fact that the bottom quark in the loop in Ref. [55] is treated massive while in JHUGEN massless so far. Ref. [55] also studied the effect due to the finite top quark width, which was found negligible. As a result, the finite top quark width was not implemented in JHUGEN.

In Fig. 3.4, the theoretical uncertainties of the $gg \to ZH$ simulation at leading order are presented. The theoretical uncertainty mainly consists of that from different PDF sets, and that from the varying energy scale of the calculation. The PDF sets used in this evaluation are CT14NNLO [51], MSTW2008LO90CL [52], and NNPDF31_LO_AS_0118 [53]. The energy scale most relevant to this simulation is the factorization scale μ^2_{Fac} used by the PDF, and has been set to $\mu_{\text{Fac}} = m_{ZH}$. To evaluate the uncertainty due to this scale, the simulation is repeated with $\mu_{\text{Fac}} = 2m_{ZH}$ and $\mu_{\text{Fac}} = m_{ZH}/2$.

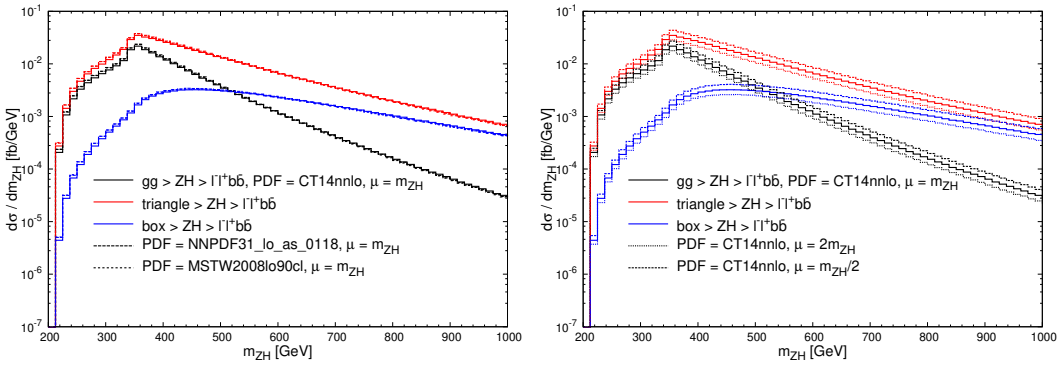

Figure 3.4: The m_{ZH} distribution for simulated $gg \to Z^* \to ZH \to \ell^-\ell^+ b\bar{b}$ SM events at 14 TeV, created with three PDF sets (left) as well as using three factorization scales (right).

The cross section varies by approximately 4% with the selected PDF sets, and 21% with the scale.

More kinematic distributions of the $gg \to ZH \to \ell^-\ell^+b\bar{b}$ process are shown in Fig. 3.5, among which the angles are defined in the same way as in Fig. 1.2.

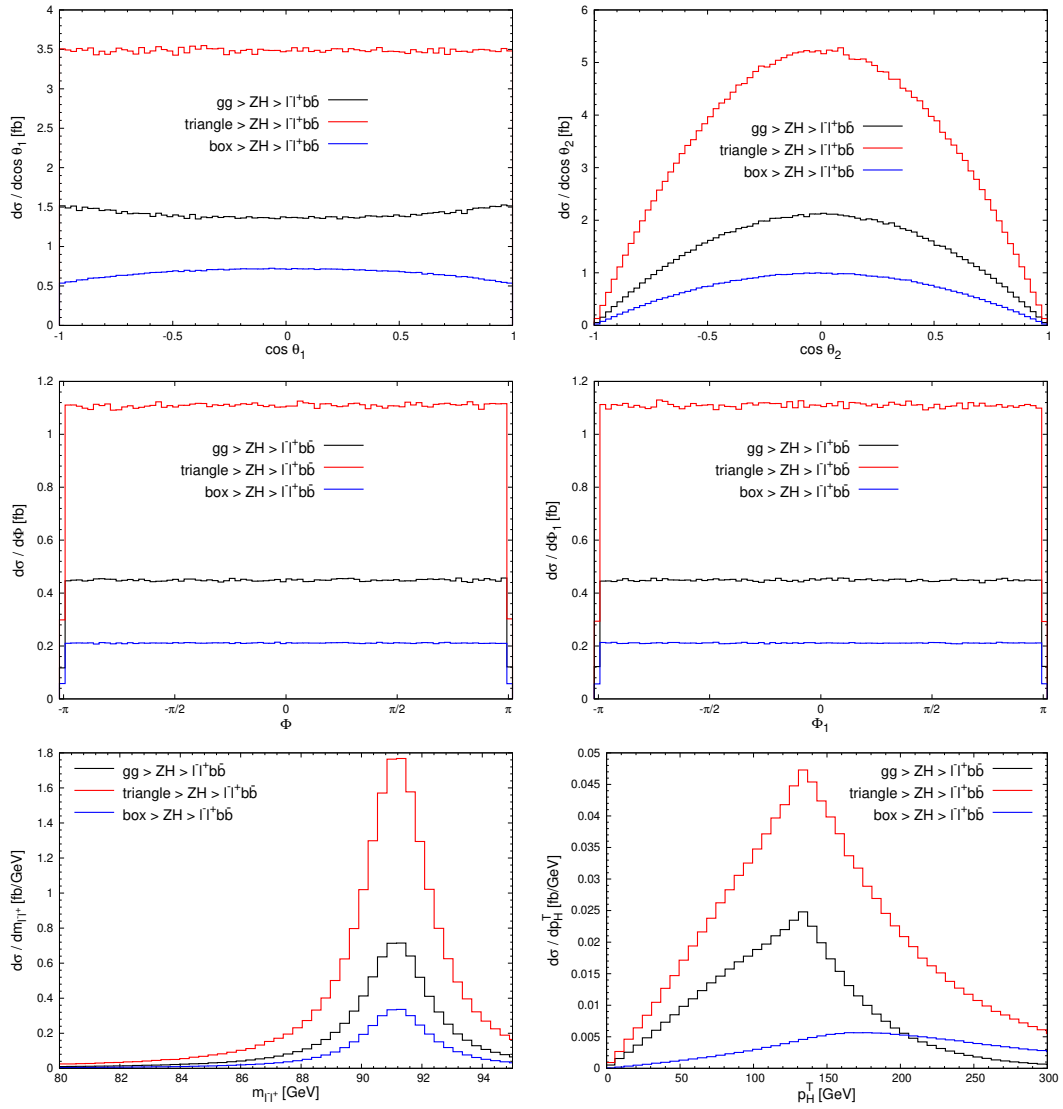

Figure 3.5: Selected kinematic distributions for simulated $gg \to ZH \to \ell^-\ell^+b\bar{b}$ SM events at 14 TeV.

The trivial flatness in Φ_1 and $\cos\theta^*$ (defined in Fig. 1.2 but not shown in Fig. 3.5) is a shared feature with the $q\bar{q} \to ZH$ processes and an outcome of the Higgs boson being a scalar particle. While the destructive interference between the triangle and the box diagrams are apparent in the figures above, the interplay between the interference and kinematic distributions may be exploited. For instance, the distribution of $\cos\theta_1$ is nearly flat for the triangle diagram alone as shown in the top left of Fig. 3.5, and it remains so across the entire range of m_{ZH}. This distribution for the box diagram, however, varies with m_{ZH}, which is shown on the left plot of Fig. 3.6. As a result, the $\cos\theta_1$ distribution of the total gg-initiated process varies with different m_{ZH} requirements, shown in the right of Fig. 3.6.

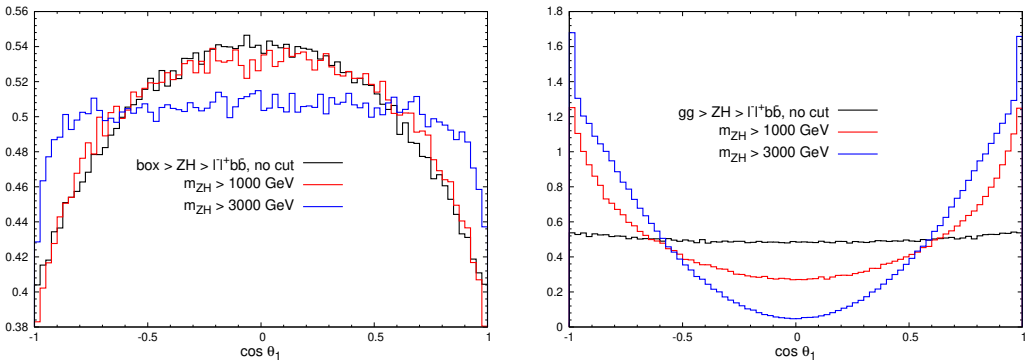

Figure 3.6: Distribution of $\cos\theta_1$ for simulated $gg \to ZH \to \ell^-\ell^+b\bar{b}$ events at 14 TeV with SM. The left plot is the distribution for the box diagram alone, and the right is that for the total gg-initiated process. All of the histograms have been normalized to an area of 1.

Notice that although the $\cos\theta_1$ distribution for the box diagram remains similar before and after the requirement of $m_{ZH} > 1000$ TeV, the distribution changes noticeably for the total gg-initiated process. In addition, while the distribution for the box diagram is somewhat flat with a requirement of $m_{ZH} >$

3000 TeV, the distribution becomes curved after interference. Of course, the m_{ZH} requirements made in Fig. 3.6 would reduce the cross sections too small to observe (4.32×10^{-3} fb for $m_{ZH} > 1000$ TeV and 9.98×10^{-7} fb for $m_{ZH} > 3000$ TeV), and only serve to show the level of interference changing against m_{ZH}. In Fig. 3.7, the same plots are made with more values of m_{ZH} requirements. The discussion of the $\cos\theta_1$ distribution is inspired by that around Fig. 4 of Ref [55].

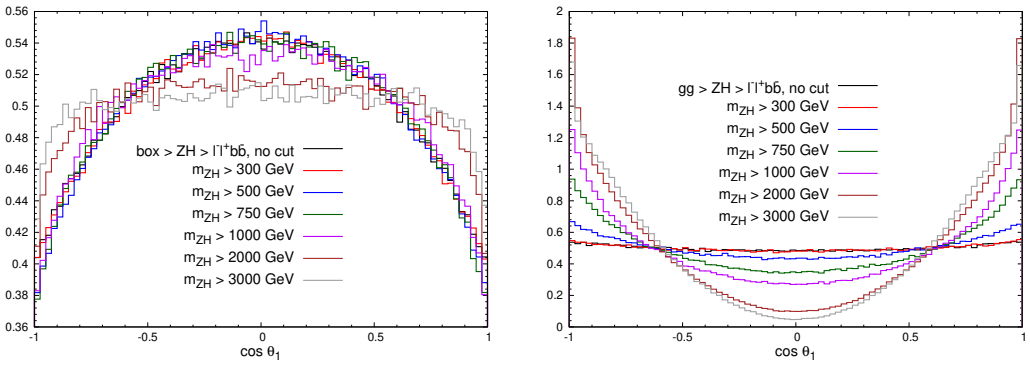

Figure 3.7: Distribution of $\cos\theta_1$ for simulated $gg \to ZH \to \ell^-\ell^+ b\bar{b}$ events at 14 TeV in SM, with various m_{ZH} requirements. The left plot is the distribution for the box diagram alone, and the right is that for the total gg-initiated process. All of the histograms have been normalized to an area of 1.

3.2.2 Isolating $gg \to ZH$ from $q\bar{q} \to ZH$

To put the gg-initiated process in the context of the pp scattering, in Fig. 3.8, I present the distributions of m_{ZH} and p_{T}^H for the $q\bar{q}$-, gg-initiated ZH processes, as well as their sum. These plots not only show the relative contribution of gg- and $q\bar{q}$-initiated process to the total $pp \to ZH$ process, but also have suggested possibilities to suppress the contribution of $q\bar{q}$ and boost the ratio of number of events of $gg \to ZH$ to that of $q\bar{q} \to ZH$. From the left plot of

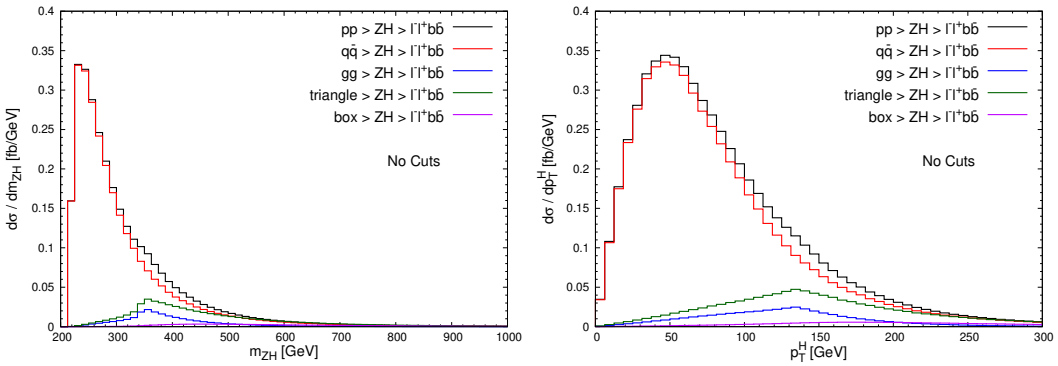

Figure 3.8: Distributions of m_{ZH} and p_{T}^{H} for simulated $ZH \to \ell^{-}\ell^{+}b\bar{b}$ SM events at 14 TeV.

Fig. 3.8, it can be expect that a requirement of $m_{ZH} > 2m_t$, where the $gg \to ZH$ cross section peaks, can significantly reduce the relative contribution of the $q\bar{q}$-initiated process. Likewise, from the right plot of Fig. 3.8, it can be expect that a requirement of $p_{\mathrm{T}}^{H} \gtrsim 100$ GeV can do the same. In Figs. 3.9 and 3.10, the non-flat kinematic distributions in Fig. 3.5 are shown with these kinematic requirements applied respectively. In Fig. 3.8, where requirements were not applied to suppress $q\bar{q} \to ZH$ contribution, the $gg \to ZH$ production contributes about 8% to the total ZH cross section, or

$$\frac{\sigma_{gg}}{\sigma_{gg+q\bar{q}}} \equiv \frac{\sigma_{gg}}{\sigma_{pp}} \approx 8\%, \quad \text{with no cuts.} \tag{3.44}$$

After the requirement of $m_{ZH} > 2m_t$ is applied,

$$\frac{\sigma_{gg}}{\sigma_{pp}} \approx 22\%, \quad \text{with } m_{ZH} > 2m_t. \tag{3.45}$$

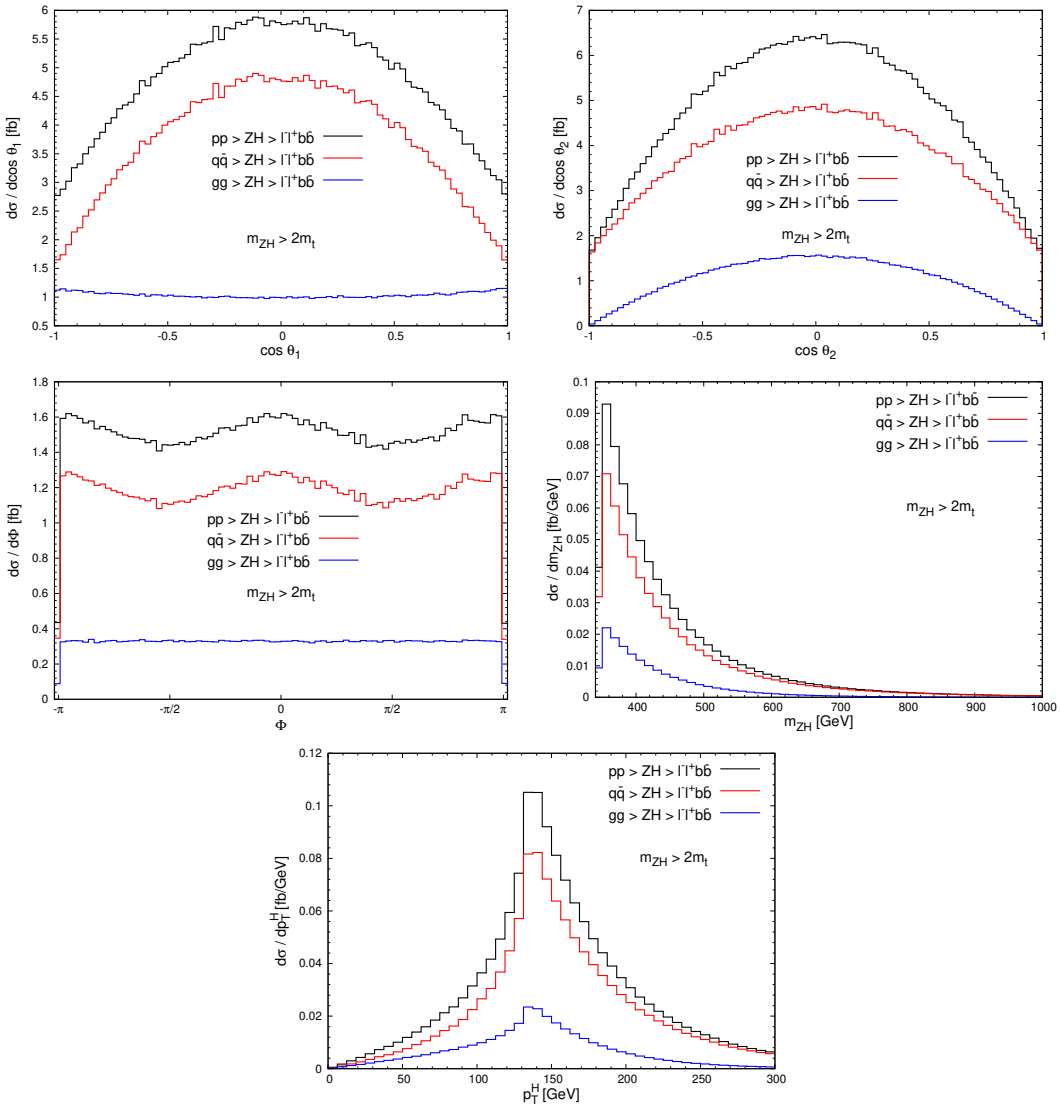

Figure 3.9: Selected kinematic distributions for simulated $gg \to Z^* \to ZH \to \ell^-\ell^+b\bar{b}$ SM events at 14 TeV, with requirements of $m_{ZH} \gtrsim 2m_t$.

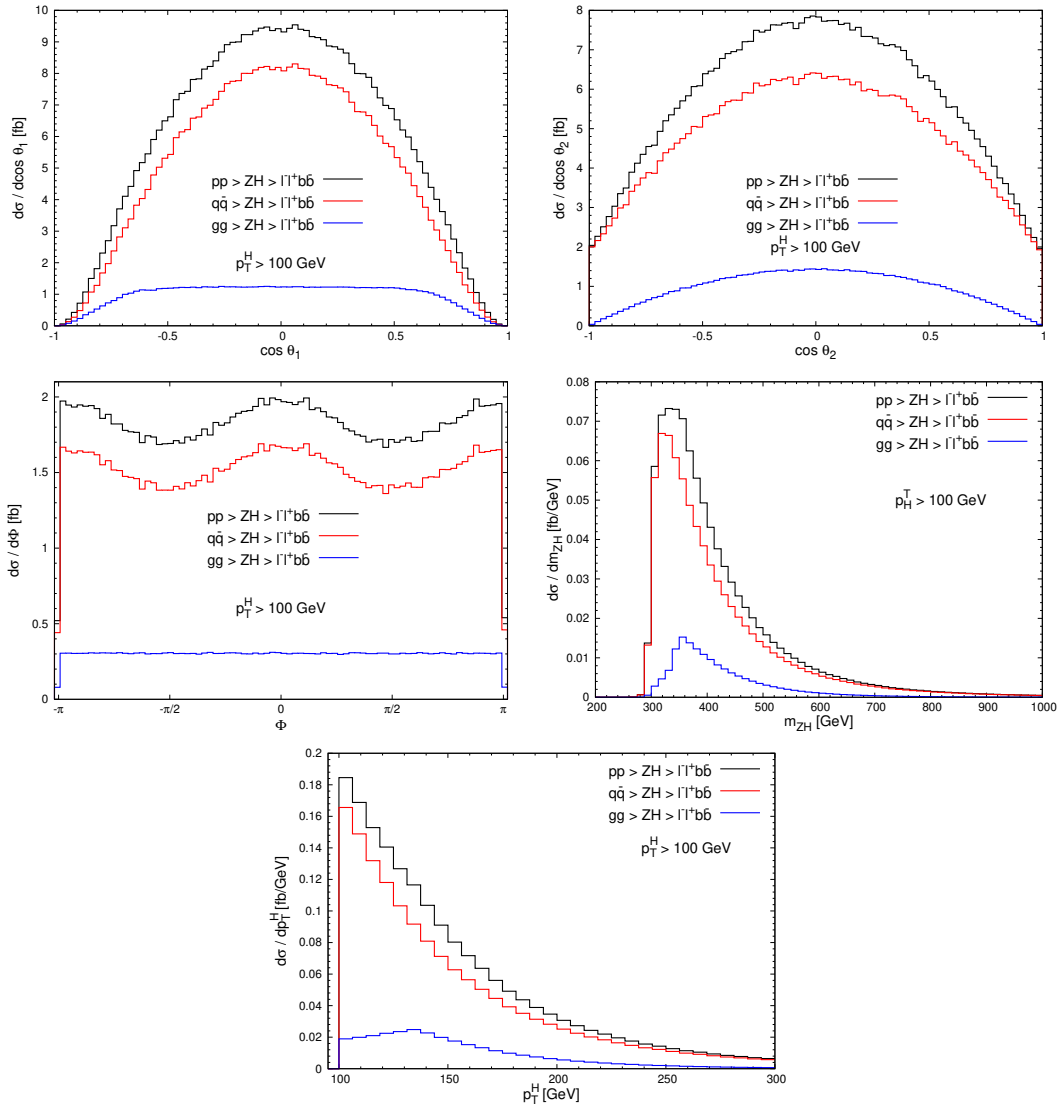

Figure 3.10: Selected kinematic distributions for simulated $gg \to Z^* \to ZH \to \ell^-\ell^+ b\bar{b}$ SM events at 14 TeV, with requirements of $p_{\mathrm{T}}^H > 100\,\mathrm{GeV}$.

The price paid was a reduction by about 27% of the $gg \to ZH$ cross section. Similarly, a cut of $p_{\mathrm{T}}^{H} > 100\,\mathrm{GeV}$ achieves

$$\frac{\sigma_{gg}}{\sigma_{pp}} \approx 17\%, \quad \text{with } p_{\mathrm{T}}^{H} > 100\,\mathrm{GeV}, \tag{3.46}$$

with a reduction by about 32% of the $gg \to ZH$ cross section.

A stronger option to suppress the $q\bar{q}$-initiated events is to apply a requirement on the matrix-element-based kinematic variable

$$D_{gg/q\bar{q}}(\{p\}) = \frac{1}{1 + \left(\frac{\sigma_{q\bar{q}}}{\sigma_{gg}}\right)\frac{\mathscr{P}_{gg}(\{p\})}{\mathscr{P}_{q\bar{q}}(\{p\})}} \quad \in [0,1], \tag{3.47}$$

where $\mathscr{P}_{gg}(\{p\})$ and $\mathscr{P}_{q\bar{q}}(\{p\})$ are the weights of a set of final-state four-momenta $\{p\}$ belonging to an event of the gg- or $q\bar{q}$-initiated process,

$$\mathscr{P}_{gg}(\{p\}) = \sum_{\text{helicities}} \frac{1}{\hat{s}} \mathrm{PDF}_{g}(x_1)\mathrm{PDF}_{g}(x_2)|\mathscr{M}_{gg}(\{p\})|^2 \mathrm{PS}(\{p\}), \tag{3.48}$$

$$\mathscr{P}_{q\bar{q}}(\{p\}) = \sum_{\text{helicities}} \sum_{q} \frac{1}{\hat{s}} \mathrm{PDF}_{q}(x_1)\mathrm{PDF}_{\bar{q}}(x_2)|\mathscr{M}_{q\bar{q}}(\{p\})|^2 \mathrm{PS}(\{p\}), \tag{3.49}$$

in which $\frac{1}{\hat{s}}$ and $\mathrm{PS}(\{p\})$ gets canceled in the fraction and $x_{1,2}$ can be deduced from $(\{p\})$. The ratio of the cross sections $\frac{\sigma_{q\bar{q}}}{\sigma_{gg}}$ is there to mitigate that $P_{q\bar{q}}(\{p\})$ is typically much larger than $P_{gg}(\{p\})$, and can be tuned to other reasonable factors such that a value of $D_{gg/q\bar{q}}$ not too close to 0 or 1 can be used to separate gg- and $q\bar{q}$-initiated events. The distribution of $D_{gg/q\bar{q}}$ for the gg- or $q\bar{q}$-initiated processes are shown in Fig. 3.11.

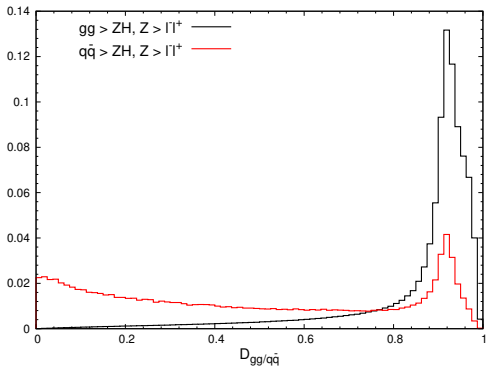

Figure 3.11: Distribution of kinematic discriminant $D_{gg/q\bar{q}}$ for simulated gg or $q\bar{q} \to ZH,\ Z \to \ell^-\ell^+$ SM events at 14 TeV.

As shown in Fig. 3.11, the gg-initiated events gather in the region of $D_{gg/q\bar{q}} \gtrsim 0.8$, while the region of $D_{gg/q\bar{q}} \lesssim 0.8$ keeps the majority of the $q\bar{q}$-initiated events. To compare the performance of $D_{gg/q\bar{q}}$ to those of the requirements of m_{ZH} and p_{T}^H (see Eq. (3.44,3.45,3.46)), a requirement of $D_{gg/q\bar{q}} \gtrsim 0.81$ is applied on both gg and $q\bar{q}$ to achieve the same effect of improving the ratio of $\frac{\sigma_{gg}}{\sigma_{pp}}$ from 8% to 28% as with the requirement of $m_{ZH} > 2m_t$. The price paid was a reduction of σ_{gg} by 20%, which is smaller compared to that of the $m_{ZH} > 2m_t$ requirement (27%).

3.2.3 A Note on $\cos\theta_1$

Unless the gluon-initiated events are isolated for analysis, all of the events produced in proton-proton scattering will be utilized in studying the ZH processes. Therefore it is natural to include both gg- and $q\bar{q}$-initiated processes in the analysis. Before doing so, the kinematic variable of $\cos\theta_1$ shall be revisited.

As defined in Chapter 1 and applied in Section 2.6, θ_1 is the angle between

the Z boson and one of the scattering fermions. At the electron-positron collider, electron and positron each travel in a fixed and known direction, so the directions of both rays of θ_1 are known. At a proton-proton collider, however, the scattering parton flavors are unknown, and, a parton of any flavor has the same probability of traveling to the $+z$ or $-z$ direction. Therefore up to now, as done in Ref. [35], $+z$ or $-z$ direction has been chosen randomly when computing θ_1. As a result, $\cos\theta_1$ will always be symmetric about 0, no matter the theoretical scenario. However, in proton-proton scattering, the overall boost of an event can be correlated with the direction of the scattering quark, as opposed to antiquark. In fact, when the hard process is quark-antiquark-initiated, the quark is more likely to carry a larger momentum fraction of its constituting proton. One can thus take advantage of this and redefine θ_1 to be the angle between the Z boson and the direction of the boost of the $Z^* \to ZH \to \ell^-\ell^+ b\bar{b}$ system:

$$\cos\theta_1 \equiv \cos\angle \mathbf{p}_Z, \mathbf{p}_{Z^*} \equiv \frac{\mathbf{p}_Z \cdot \mathbf{p}_{Z^*}}{|\mathbf{p}_Z||\mathbf{p}_{Z^*}|}. \tag{3.50}$$

In Fig. 3.12, the distribution of $\cos\theta_1$ is presented in 3 different definitions for simulated $q\bar{q} \to ZH \to \ell^-\ell^+ b\bar{b}$ events at 14 TeV assuming the theoretical scenario of 50% pseudoscalar with $\pi/2$ relative phase between the SM and pseudoscalar contributions. In Fig. 3.12, the symmetric distribution is for the definition of $\cos\theta_1$ that identifies one of its rays fixed with one direction of the scattering beam. This is the definition used in Ref. [35]. The definition which identifies one ray of the θ_1 angle with the boost of the event produces an asymmetric $\cos\theta_1$, which would be observable. The last definition assumes

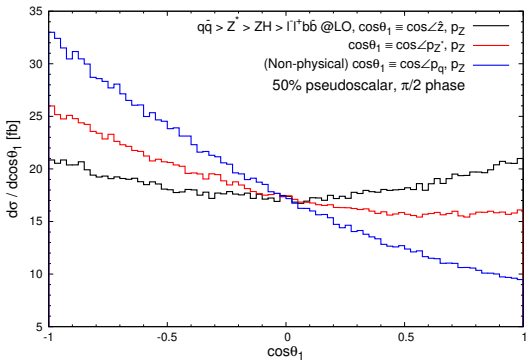

Figure 3.12: Distribution of $\cos\theta_1$ in 3 definitions for simulated $q\bar{q} \to ZH \to \ell^-\ell^+ b\bar{b}$ events assuming the theoretical scenario of 50% pseudoscalar with $\pi/2$ relative phase between the SM and pseudoscalar contributions. See Table 3.1 for couplings used.

knowledge of the scattering parton flavor, and identifies one ray of the θ_1 angle with the direction of the quark. This results in an even more pronounced asymmetry in $\cos\theta_1$, which is of course possible only in a simulation where flavors of the scattering partons are known. In the remaining of the chapter, the second definition, or that in Eq. (3.50), will be used.

3.2.4 $gg \to ZH$ with Anomalous Couplings

As pointed out in the bullet points (iii) and (iv) at the beginning of this chapter, the anomalous Higgs boson couplings to weak bosons, parameterized by g_2 and g_4, do not contribute to the $gg \to ZH$ production. Therefore, if the HZZ coupling is entirely g_2 or g_4, the contribution of the triangle diagrams simply vanishes, and only that from the box diagrams survives. The box-only results have been presented in Section 3.2.1, with the Higgs boson couplings to fermions assumed to have SM couplings.

It is my intention then to study the experimental effect of the Higgs boson anomalous couplings to heavy quarks, Htt and Hbb exclusively, in the

$gg \to ZH \to \ell^-\ell^+ b\bar{b}$ process. The HZZ coupling is assumed SM, and representative combinations of κ and $\tilde{\kappa}$, which parameterize the Higgs boson Yukawa coupling according to Eq. (1.30), are chosen in this study. The overall strength of the Higgs boson Yukawa coupling is kept at the SM value, namely,

$$|\kappa|^2 + |\tilde{\kappa}|^2 = 1, \tag{3.51}$$

and the same κ and $\tilde{\kappa}$ are assumed for both Htt and Hbb couplings. Again, the Htt and Hbb couplings enter the $gg \to ZH \to \ell^-\ell^+ b\bar{b}$ process as indicated by the shaded bulbs with dashed contour in Fig. 3.1. However, it should be noted that the $H \to b\bar{b}$ decay is shared by both the triangle and box diagrams, and because of the scalar nature of the Higgs boson, the choice of κ and $\tilde{\kappa}$ does not affect the kinematics through the blob of the $H \to b\bar{b}$ decay except for the normalization if Eq. 3.51 is violated.

In Fig. 3.13, the kinematic distributions of the simulated $gg \to ZH \to \ell^-\ell^+ b\bar{b}$ events at 14 TeV are presented for selected combinations of κ and $\tilde{\kappa}$. As shown in Fig. 3.13, all of the non-SM combinations of κ and $\tilde{\kappa}$ result in larger cross sections of the $gg \to ZH \to \ell^-\ell^+ b\bar{b}$ process. Among all, the "wrong sign" scenario of $\kappa = -1$ results in the largest cross section by turning the destructive interference between the triangle diagrams and the box diagrams in SM into a constructive one. The "wrong sign" scenario boosts the cross section of the $gg \to ZH \to \ell^-\ell^+ b\bar{b}$ from 2.9 fb to 14.0 fb. This boost is significant compared to the $q\bar{q} \to ZH \to \ell^-\ell^+ b\bar{b}$ cross section of 34.0 fb, which is not affected by the choice of κ and $\tilde{\kappa}$ as long as Eq. (3.51) holds.

While it is impossible to separate the contributions from the triangle and

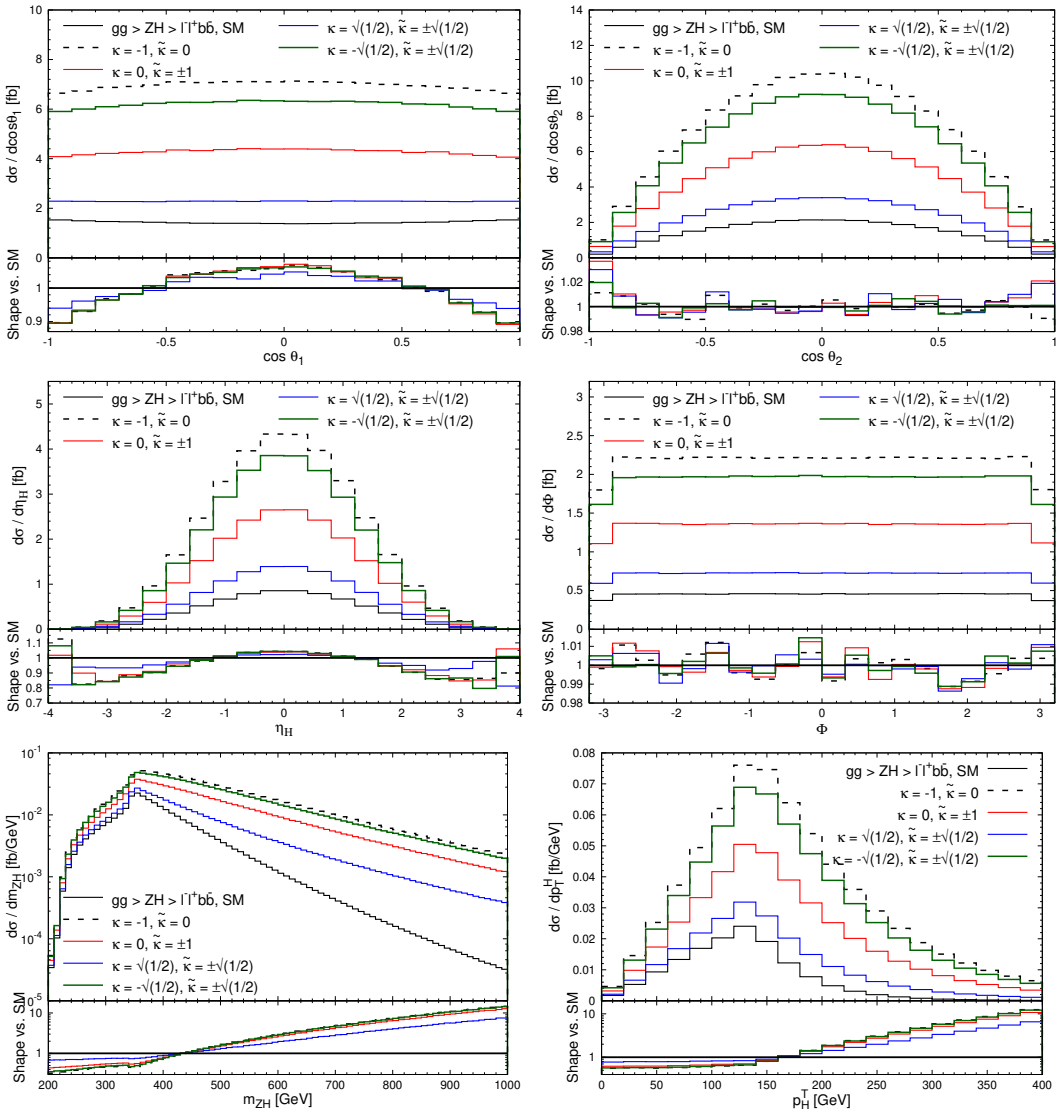

Figure 3.13: Selected kinematic distributions of simulated $gg \to ZH \to \ell^-\ell^+b\bar{b}$ events at 14 TeV with selected combinations of κ and $\tilde{\kappa}$. The definition of $\cos\theta_1$ is in Eq. (3.50). The bottom panels present the shapes of the distributions relative to the SM distribution, or more precisely, $\frac{\sigma_{SM}}{\sigma}\frac{d\sigma/dx}{d\sigma_{SM}/dx}$, where x is any selected kinematic variable.

the box diagrams, in Fig. 3.14, the kinematic distributions of the simulated $box \to ZH \to \ell^-\ell^+b\bar{b}$ events at 14 TeV are presented for selected combinations of κ and $\tilde{\kappa}$.

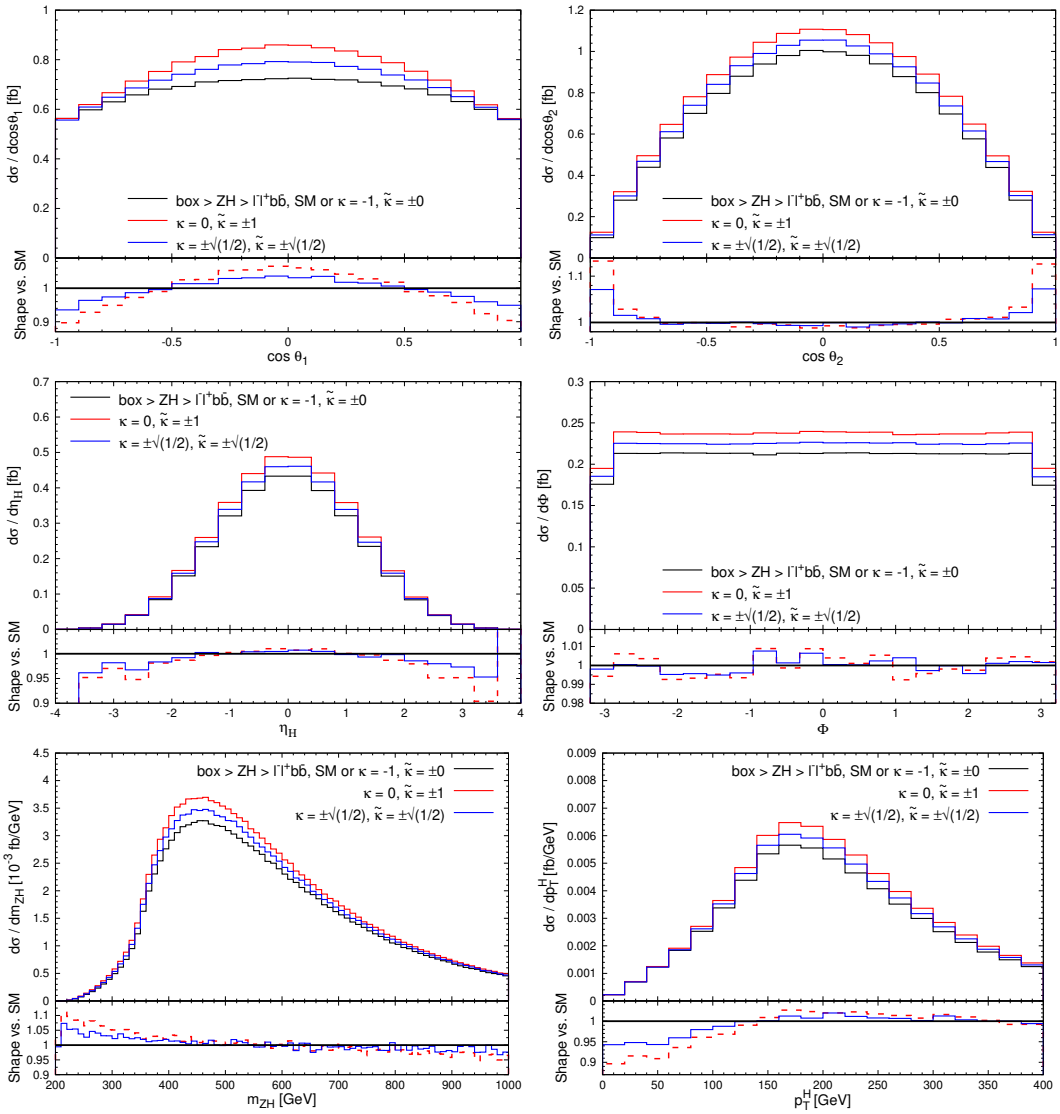

Figure 3.14: Selected kinematic distributions of simulated $gg \to$ box only $\to ZH \to \ell^-\ell^+b\bar{b}$ events at 14 TeV with selected combinations of κ and $\tilde{\kappa}$. The definition of $\cos\theta_1$ is in Eq. (3.50). The bottom panels present the shapes of the distributions relative to the SM distribution, or more precisely, $\frac{\sigma_{SM}}{\sigma}\frac{d\sigma/dx}{d\sigma_{SM}/dx}$, where x is any selected kinematic variable.

As shown in Fig. 3.14, the pseudoscalar coupling between the quark loop and the Higgs boson results in difference from the (SM) scalar coupling in both the cross section and the shape of the kinematic distributions. The signs of the κ and $\tilde{\kappa}$ parameter do not matter, because there is no interference when the box diagram is considered along.

The choices of κ and $\tilde{\kappa}$ do not only affect the cross section of the $gg \to ZH \to \ell^-\ell^+ b\bar{b}$ process, but also change the kinematic distributions as well. This is not unexpected. As I have shown in Section 3.2.1, the triangle diagrams and the box diagrams interfere at different levels in different kinematic region. The choice of κ and $\tilde{\kappa}$ affects the interference, and is unlikely to result in kinematic distributions that are simply scaled from those of the SM case.

Another observation from the distributions is that the sign of $\tilde{\kappa}$ does not affect the distribution. This suggests that the $\tilde{\kappa}$ contribution does not interfere with other contributions, and is proportional to $|\tilde{\kappa}|^2$ only. This speculation is found true using repeated simulations with $\tilde{\kappa}$ rotated around the complex plane. In other word, the $gg \to ZH \to \ell^-\ell^+ b\bar{b}$ process is insensitive to the relative phase between κ and $\tilde{\kappa}$.

3.2.5 Combined $gg + q\bar{q} \to ZH$ with Anomalous Couplings

In this and the next subsections, I extend the study of the ZH production in Ref. [35] by combining the (LO) $q\bar{q} \to ZH$ production with the $gg \to ZH$ production. In selecting the representative values of anomalous couplings to study, I adopt a similar way used in Ref. [35] when mixing the Standard Model couplings with anomalous couplings. In mixing SM and the g_2 contribution,

I started by calculating the contribution due to g_2 alone, and finding the value of g_2, or $g_{2,\max}$, such that the proton-proton (sum of gluon-gluon and quark-antiquark) cross section equals to the SM value. Then the relation of

$$\left(\frac{g_1}{2}\right)^2 + \left(\frac{g_2}{g_{2,\max}}\right)^2 = 1 \tag{3.52}$$

is maintained while selecting tentative $(g_1,\ g_2)$ pairs, where the 2 beneath g_1 is there because in SM $g_1 = 2$. Because of the interferences between g_1 and g_2 amplitudes, the relation in Eq. (3.52) does not maintain the cross section at the SM value exactly, and fine adjustment of the coupling constants is needed to keep the total cross section constant.

The selection of the values of g_4 is similar to that of g_2, but since the interference between g_1 and g_4 and that between κ and $\tilde{\kappa}$ is zero, the following relations are kept exactly,

$$\left(\frac{g_1}{2}\right)^2 + \left(\frac{|g_4|}{g_{4,\max}}\right)^2 = 1 \quad , \tag{3.53}$$

$$|\kappa|^2 + |\tilde{\kappa}|^2 = 1 \quad , \tag{3.54}$$

$$\frac{g_1}{2} = \frac{|\kappa|}{1} \quad , \tag{3.55}$$

$$\frac{|g_4|}{g_{4,\max}} = \frac{|\tilde{\kappa}|}{1} \quad . \tag{3.56}$$

The absolute sign in Eq. (3.56) signifies that the anomalous coupling constants can be complex, and there can be a relative phase between SM and anomalous amplitudes.

In the following table, the theoretical scenarios I am considering are listed

with the corresponding coupling constants.

Scenario	g_1	g_2	g_4	κ	$\tilde{\kappa}$	Λ
Standard Model	2	0	0	1	0	–
$g_2(\hat{s})$	0	≈ 0.283	0	1	0	1 TeV
Pseudoscalar	0	0	≈ 0.386	0	1	1 TeV
50% pseudoscalar	$\sqrt{2}$	0	$\approx \frac{0.386}{\sqrt{2}}$	$\frac{1}{\sqrt{2}}$	$\frac{1}{\sqrt{2}}$	1 TeV
50% pseudoscalar, with $\pi/2$ relative phase with SM	$\sqrt{2}$	0	$\approx \frac{0.386\,\mathrm{i}}{\sqrt{2}}$	$\frac{1}{\sqrt{2}}$	$\frac{\mathrm{i}}{\sqrt{2}}$	1 TeV

Table 3.1: Coupling constants of theoretical scenarios considered in this chapter. Note that these values are not the same as those in Table 2.1.

Because of the non-renormalizable nature of the operators $g_2 H Z_{\mu\nu} Z^{\mu\nu}$ and $g_4 H Z_{\mu\nu} \tilde{Z}^{\mu\nu}$, the coupling "constants" g_2 and g_4 cannot remain constant at arbitrary high energy, and these "constants" should eventually become energy-dependent form factors. To account for this, the simple ad hoc prescriptions

$$g_2 \;\to\; g_2(\hat{s}) = g_2 \frac{\Lambda^2}{\Lambda^2 + \hat{s}} \quad , \tag{3.57}$$

$$\text{and} \quad g_4 \;\to\; g_4(\hat{s}) = g_4 \frac{\Lambda^2}{\Lambda^2 + \hat{s}} \tag{3.58}$$

are introduced, both of which have been implemented in JHUGEN. The choice of cutoff energy scale $\Lambda = 1\,\mathrm{TeV}$, where beyond-SM physics may emerge, is arbitrary. In the Fig. 3.15, the kinematic distributions for simulated $pp(gg + q\bar{q}) \to ZH \to \ell^-\ell^+ b\bar{b}$ events are presented for selected theoretical

scenarios. The scenario of 50% pseudoscalar with $\pi/2$ relative phase with SM is presented because of its noticeable distinction in the $\cos\theta_1$, $\cos\theta_2$ and Φ distributions from those without the relative phase. To be specific, in the $\cos\theta_1$ and $\cos\theta_2$ distributions, the $\pi/2$ relative phase leads to asymmetry about $\cos\theta_2 = 0$; and in the Φ distribution, the $\pi/2$ relative phase leads to symmetry about $\Phi = 0$ while the absence of the $\pi/2$ relative phase leads to asymmetry about $\Phi = 0$.

3.2.6 Application of Matrix-Element-Based Kinematic Discriminants

Although with sufficiently large amount of experimental data, one should be able to resolve different theoretical scenarios or set constraints on the anomalous coupling constants using the presented kinematic distributions, even with an integrated luminosity of $3000\,\text{fb}^{-1}$ at $s = 14\,\text{TeV}$ from the High-Luminosity LHC, the number of ZH events implied from the cross sections listed in Ref. [63] is expected to be a fraction of 0.1 million, which will be much less than the number of unweighted events, which is 10 million, that can populate the above histograms to their precisions. It is therefore desired to find kinematic variables that are much more sensitive to the theoretical scenarios. The superior performance of the matrix-element-based discriminant in separating the gluon-initiated events from the quark-initiated events, shown in Fig.3.11, suggests that it may be applied here.

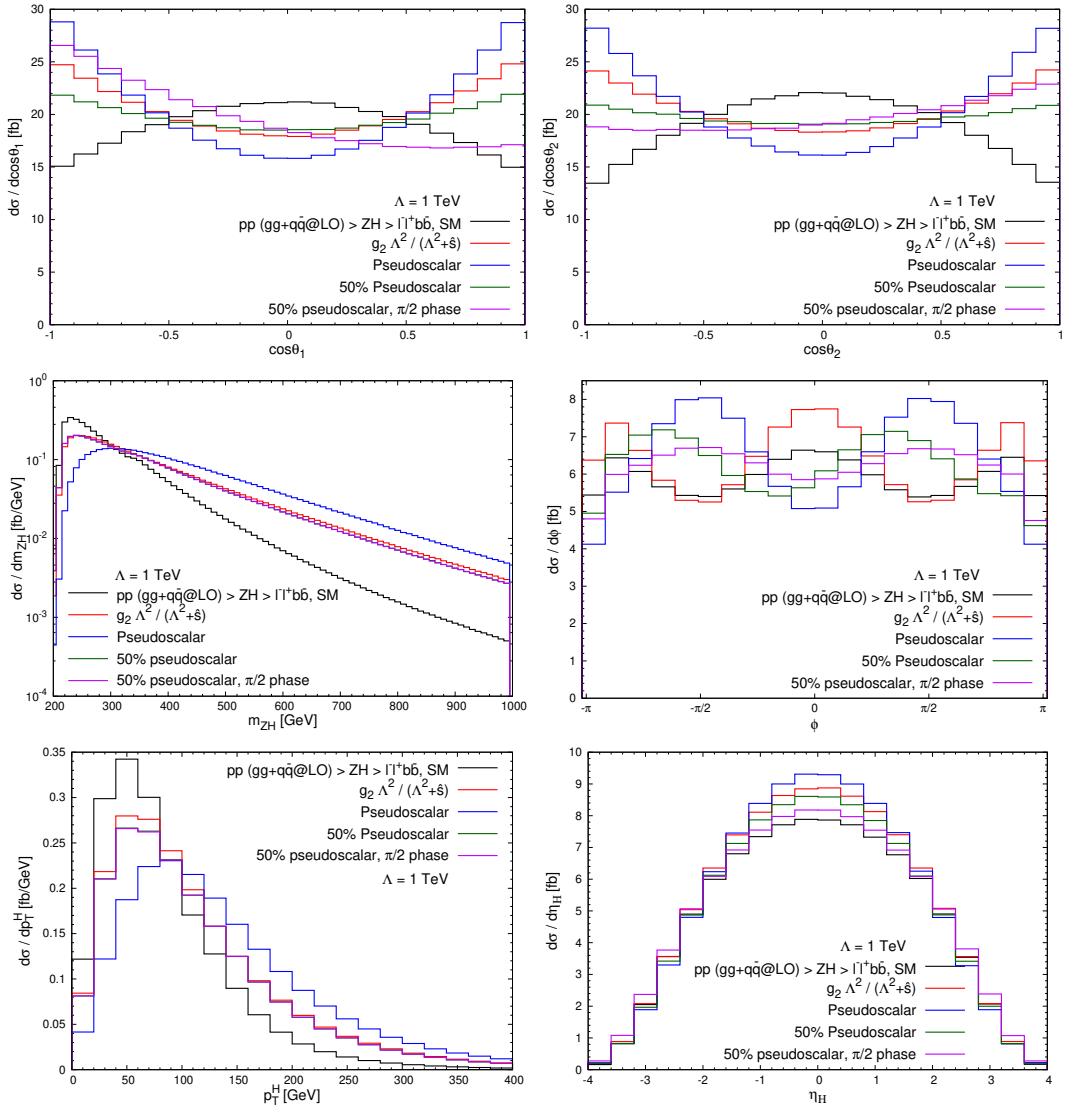

Figure 3.15: Selected kinematic distributions for simulated $pp\ (gg + q\bar{q}) \to ZH \to \ell^-\ell^+ b\bar{b}$ events at 14 TeV with selected theoretical scenarios, the coupling constants are listed in Table 3.1. The definition of $\cos\theta_1$ is in Eq. (3.50).

Define

$$D_{\text{A/B, }(gg \text{ or } q\bar{q} \text{ or } pp)}(\{p\}) = \frac{1}{1 + \left(\frac{\sigma_B}{\sigma_A}\right)\frac{\mathscr{P}_{A,\,(gg \text{ or } q\bar{q} \text{ or } pp)}(\{p\})}{\mathscr{P}_{B,\,(gg \text{ or } q\bar{q} \text{ or } pp)}(\{p\})}} \quad \in [0,1], \tag{3.59}$$

where A and B denotes the theoretical scenarios to be resolved, $\mathscr{P}_A(\{p\})$ and $\mathscr{P}_B(\{p\})$ are the weights of a set of final-state four-momenta $\{p\}$ belonging to an event of the A or B scenario, and the subscripts of gg, $q\bar{q}$, or pp denotes whether the discriminant is for gg- or $q\bar{q}$-initiated events only, or for all of the $pp \to ZH$ events. Correspondingly,

$$\mathscr{P}_{A,\,gg}(\{p\}) = \sum_{\text{helicities}} \frac{1}{\hat{s}} \text{PDF}_g(x_1)\text{PDF}_g(x_2)|\mathscr{M}_{A,\,gg}(\{p\})|^2 \text{PS}(\{p\}), \tag{3.60}$$

$$\mathscr{P}_{A,\,q\bar{q}}(\{p\}) = \sum_{\text{helicities}} \sum_{q} \frac{1}{\hat{s}} \text{PDF}_q(x_1)\text{PDF}_{\bar{q}}(x_2)|\mathscr{M}_{A,\,q\bar{q}}(\{p\})|^2 \text{PS}(\{p\}), \tag{3.61}$$

$$\mathscr{P}_{A,\,pp}(\{p\}) = \sum_{\text{helicities}} \sum_{a,b} \frac{1}{\hat{s}} \text{PDF}_a(x_1)\text{PDF}_b(x_2)|\mathscr{M}_{A,\,a,b}(\{p\})|^2 \text{PS}(\{p\}), \tag{3.62}$$

where the sum over a and b is the sum over all applicable parton combinations for the ZH processes. Similar to that with Eqs. (3.48) and (3.49), because of the shared phase space weight, $\frac{1}{\hat{s}}$ and $\text{PS}(\{p\})$ gets canceled in the fraction. Again, $x_{1,2}$ can be deduced from $(\{p\})$. In resolving the theoretical scenarios listed in Table 3.1 the cross section ratio can be set to 1.

In Fig. 3.16, the distributions of kinematic discriminants $D_{g_2/\text{SM},\,gg}$ and $D_{\text{Pseudoscalar/SM},\,gg}$ for simulated $gg \to ZH \to \ell^-\ell^+ b\bar{b}$ events are presented

with relevant theoretical scenarios.

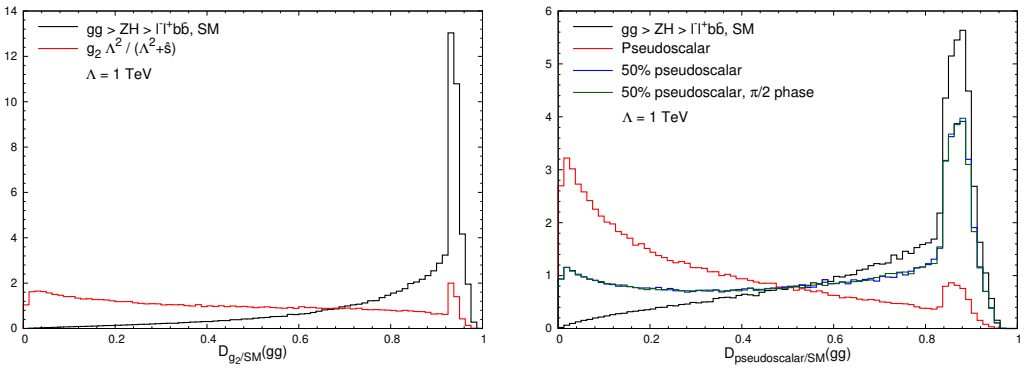

Figure 3.16: Distributions of kinematic discriminants $D_{g_2/\mathrm{SM},\,gg}$ (left) and $D_{\mathrm{Pseudoscalar/SM},\,gg}$ (right) for simulated $gg \to ZH \to \ell^-\ell^+ b\bar{b}$ events at 14 TeV with relevant theoretical scenarios, the coupling constants are listed in Table 3.1. All of the histograms have been normalized to an area of 1.

On the left plot of Fig. 3.16, because g_2 is known for resulting in zero contribution from the triangle diagram, the distribution of g_2 is really that of the SM box diagrams, and the discriminant is separating the entire $gg \to (\text{triangle} + \text{box}) \to ZH$ process from the $gg \to (\text{box}) \to ZH$ process.

On the right plot of Fig. 3.16, the value of $D_{\mathrm{Pesudoscalar/SM},\,gg}$ tends to gather around 0.9 for Standard Model $gg \to ZH$ events, and 0 for pseudoscalar. The scenarios of 50% pseudoscalar with and without relative phase both share some features with both the SM and pseudoscalar distributions, but are indistinguishable from each other. To identify the relative phase, a dedicated discriminant may be constructed. Notice the similarity between figures on the left and right. It is due to the fact that both the g_2 and pseudoscalar scenarios receive contribution only from the box diagrams, except that the Htt and Hbb couplings are not SM.

In Fig. 3.17, the distributions of kinematic discriminants $D_{g_2/\mathrm{SM},\,pp}$ and

$D_{\text{Pseudoscalar/SM, }pp}$ for simulated $pp(gg + q\bar{q}) \rightarrow ZH \rightarrow \ell^-\ell^+ b\bar{b}$ events are presented with relevant theoretical scenarios. With the addition of $q\bar{q}$ events,

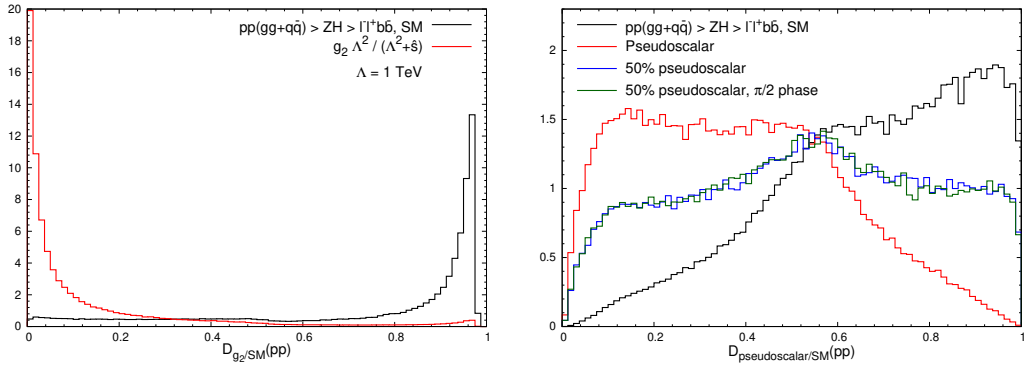

Figure 3.17: Distributions of kinematic discriminants $D_{g_2/\text{SM, }pp}$ (left) and $D_{\text{Pseudoscalar/SM, }pp}$ (right) for simulated $pp(gg + q\bar{q}) \rightarrow ZH \rightarrow \ell^-\ell^+ b\bar{b}$ events at 14 TeV with relevant theoretical scenarios. The coupling constants are listed in Table 3.1. All of the histograms have been normalized to an area of 1.

in the distribution of $D_{g_2/\text{SM, }pp}$, the SM events are seem to be tightly packed around 1, and those due to g_2 contribution around 0. The separation between SM and pseudoscalar events are not as dramatic as that on the right plot of Fig. 3.16 or the left plot of Fig. 3.17, but is still much more apparent than that in the kinematic distributions presented in Fig. 3.13 or Fig. 3.15. Again, the discriminant $D_{\text{Pseudoscalar/SM, }pp}$ is incapable of determining the relative phase between SM and the pseudoscalar couplings, and the distributions of $\cos\theta_2$ and Φ with the pp events, or a dedicated kinematic discriminant such as D_{CP} used in Ref. [35] is needed.

The application of kinematic discriminant on $q\bar{q}$-initiated events can be found in Ref. [35]. It is worth noting that in determining the relative phase between two coupling constants, which is left to accomplish, a kinematic discriminant that involves two matrix elements and their interference can be

constructed. Inspired by Eq. (B4) of Ref. [35], and with $\frac{\sigma_B}{\sigma_A}$ set to 1,

$$D_{\text{Phase,=}(gg \text{ or } q\bar{q} \text{ or } pp)}(\{p\}) \sim \frac{\mathscr{P}_{\text{Interference, }(gg \text{ or } q\bar{q} \text{ or } pp)}(\{p\})}{\mathscr{P}_{A,\,(gg \text{ or } q\bar{q} \text{ or } pp)}(\{p\}) + \mathscr{P}_{B,\,(gg \text{ or } q\bar{q} \text{ or } pp)}(\{p\})}, \tag{3.63}$$

where

$$\mathscr{P}_{\text{Interference}}(\{p\}) \sim 2\Re\big(\mathscr{M}_A^*(\{p\})\mathscr{M}_B(\{p\})\big), \tag{3.64}$$

and the subscripts of gg, $q\bar{q}$, or pp correspond to the treatments in Eq. (3.60, 3.61, and 3.62) respectively, may be applied to the gg-initiated or all of the proton-proton events.

To resolve the relative phase between the Standard Model amplitude and that of the pseudoscalar contribution, in the Fig. 3.18, the distributions of kinematic discriminants $D_{\text{phase, pseudoscalar, }gg}$ and $D_{\text{phase, pseudoscalar, }pp}$ for simulated $gg \to ZH \to \ell^-\ell^+ b\bar{b}$ and $pp(gg + q\bar{q}) \to ZH \to \ell^-\ell^+ b\bar{b}$ events respectively are presented with the theoretical scenarios "50% pseudoscalar" and "50% pseudoscalar, with $\pi/2$ relative phase with SM". The $D_{\text{phase, pseudoscalar, }gg}$ distribution, which utilizes the $gg \to ZH$ process alone, is not sensitive to the relative phase between SM and the pseudoscalar amplitudes. This is consistent with the last statement made in Section 3.2.4. With the addition of the $q\bar{q} \to ZH$ process, which by itself is sensitive to the relative phase (seen in Fig. 18 of Ref. [35]), the $D_{\text{phase, pseudoscalar, }pp}$ distribution indeed shows noticeable difference between the theoretical scenarios with and without the $\pi/2$ phase difference.

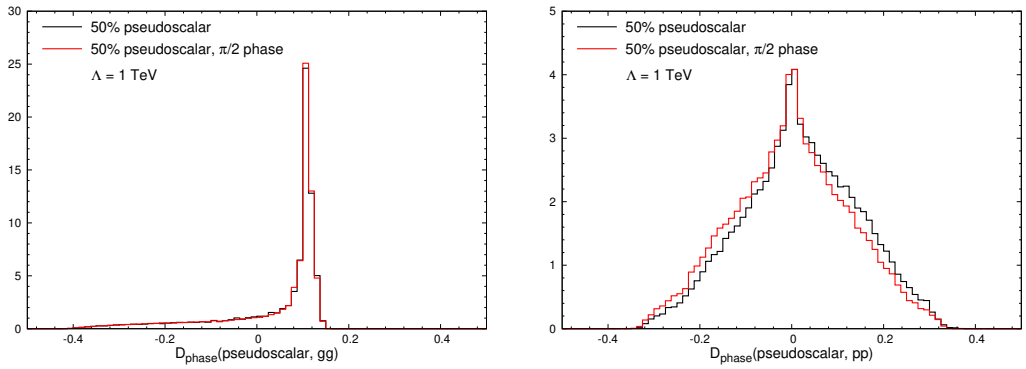

Figure 3.18: Distributions of kinematic discriminants $D_{\text{phase, pseudoscalar, }gg}$ (left) and $D_{\text{phase, pseudoscalar, }pp}$ (right) for simulated $gg/pp(gg + q\bar{q}) \to ZH \to \ell^-\ell^+ b\bar{b}$ events at 14 TeV with relevant theoretical scenarios, the coupling constants are listed in Table 3.1. All of the histograms have been normalized to an area of 1.

3.2.7 Exploiting the ZH/WH (A)symmetry

This section is inspired by Ref. [64]. It argues that the ratio of the Drell-Yan-like component of the ZH and WH cross sections can be calculated to high precision. Since WH does not have any non-Drell-Yan-like component, by comparing that ratio to the experimentally measured ZH/WH cross-section ratio, which allows for the cancellation of many systematical uncertainties, one can probe the beyond-Standard-Model (BSM) physics in the loop-induced $gg \to ZH$ component at the High-Luminosity Large Hadron Collider (HL-LHC). In this section I will discuss the dependence of signal strength of the $pp \to WH$ process on the anomalous coupling constants. It will be found out that the dependences can be sensitive to the theoretical assumptions.

One can argue that the anomalous coupling constants g_2 and g_4 are dependent on the vector bosons to which the Higgs boson couples, and they are

related by the expressions[63],

$$g_2^{HWW} = \cos^2\theta_W g_2^{HZZ} + \sin^2\theta_W g_2^{H\gamma\gamma} + 2\cos\theta_W \sin\theta_W g_2^{HZ\gamma}, \tag{3.65}$$

$$g_2^{HWW} = \cos^2\theta_W g_4^{HZZ} + \sin^2\theta_W g_4^{H\gamma\gamma} + 2\cos\theta_W \sin\theta_W g_4^{HZ\gamma}, \tag{3.66}$$

where the superscripts HZZ, $H\gamma\gamma$, and $HZ\gamma$ denotes the anomalous interactions may be considered. The latter two are beyond the scope of this thesis, making the corresponding $g_{2,4}^{H\gamma\gamma,HZ\gamma} = 0$. θ_W is the weak mixing angle with $\cos\theta_W = m_W/m_Z$ in the Standard Model.

In the following figure, I assume that

$$g_2^{HWW} = \cos^2\theta_W g_2^{HZZ} \quad \text{, and} \quad g_4^{HWW} = \cos^2\theta_W g_4^{HZZ} \quad , \tag{3.67}$$

and I present the signal strength of the $pp \to WH$ process assuming that the cross section of the $pp \to ZH$ process is kept at its SM value with Eq. (3.52) up to some adjustments and Eq. (3.56).

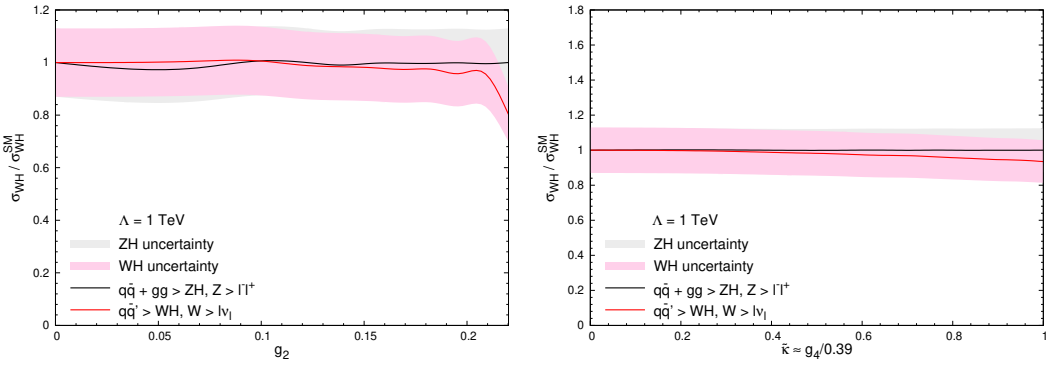

Figure 3.19: Dependence of signal strength of WH at 14 TeV with uncertainty on g_2^{HZZ} (left), with g_1 set to approximately maintain the total cross section of $ZH \to \ell^-\ell^+ b\bar{b}$ at the SM value; and on g_4^{HZZ} (right) and $\tilde{\kappa}$. g_1, κ, and $\tilde{\kappa}$ are assumed to be the same for ZH and WH processes. g_2^{HWW} and g_4^{HWW} are related to g_2^{HZZ} and g_4^{HZZ} by Eq. (3.65 and 3.66) respectively.

The uncertainties are estimated using the percentage uncertainty presented earlier in this chapter. Unfortunately, with the uncertainty in the leading order calculations, the signal strength of the $pp \to WH$ process would not deviate significantly from 1. This is not surprising, because both g_2 and g_4 couplings do not contribute to the $gg \to ZH$ process, and turning them on is to decrease the contribution from the triangle diagram, which may not be numerical significant compared to the larger $q\bar{q} \to ZH$ cross section.

In the following figure, a different assumption is made,

$$g_2^{HWW} = g_2^{HZZ} \quad \text{, and} \quad g_4^{HWW} = g_4^{HZZ} \quad , \tag{3.68}$$

and I present the signal strength of the $pp \to WH$ process assuming that the cross section of the $pp \to ZH$ process is kept at its SM value with Eq. (3.52) up to some adjustments and Eq. (3.56). Again on the left of Fig. 3.20, with

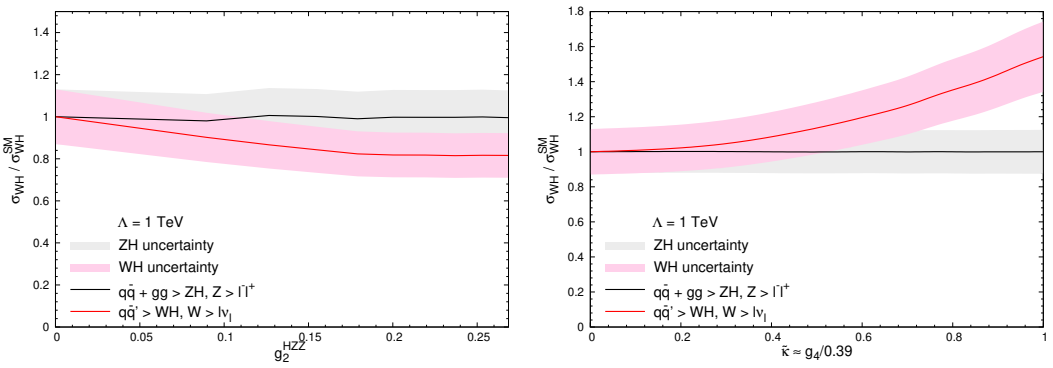

Figure 3.20: Dependence of signal strength of WH at 14 TeV with uncertainty on g_2, with g_1 set to approximately maintain the total cross section of $ZH \to \ell^-\ell^+ b\bar{b}$ at the SM value (left); and on g_4 and $\tilde{\kappa}$. All coupling constants are assumed to be the same for ZH and WH processes (right).

the uncertainty in the leading order calculations, the signal strength of the $pp \to WH$ process would not deviate significantly from 1. On the other hand,

on the right of Fig. 3.20, the $q\bar{q} \to ZH$ cross section increases with increasing g_4, and so does the signal strength of the $q\bar{q}' \to WH$ process.

Fig. 3.19 and Fig. 3.20 only serve to demonstrate that, depending on the theoretical assumptions, the comparison between the ZH and WH processes may be used to extract information on the HVV anomalous couplings. However, it is the best that one goes beyond the mere signal strength, and explores other aspects of the two processes simultaneously.

Chapter 4

$pp \to VH$ Production at Next-to-Leading Order QCD

In Chapter 3, I have shown that in the Standard Model the Higgs boson production in association of a Z boson (ZH) receives $\lesssim$ 10% contribution from gluon fusion ($gg \to ZH$). It is therefore necessary to include the next-to-leading order (NLO) correction to the VH production in quark annihilation, which is at $\sim$ 10% level with LHC energies [65, 66, 67, 68, 69, 70, 71].

The NLO calculation of the $q\bar{q}' \to V^* \to VH$ processes is an application of a subtraction-based algorithm introduced in Ref. [72]. In the following sections, I will present the expressions specific to the VH processes. Because the NLO correction to the $q\bar{q}' \to V^* \to VH$ processes takes place around the $q\bar{q}' \to V^*$ vertex, and does not involve the decay chain of the V^* boson[1], the latter will most often not be expressed explicitly.

[1]The NLO QCD correction to the hadronic decay of the V boson ($V \to q\bar{q}'$), as well as that to the $Hb\bar{b}$ decay, are always treated in JHUGEN. The main effect of the $V \to q\bar{q}'$ decay is captured by a constant scaling factor applied to the Vqq' coupling. The main effect of the $Hb\bar{b}$ decay is captured by evolving the b-quark mass to the energy scale of the Higgs boson mass.

In addition to the real and virtual corrections to the LO calculation, consistence in the NLO calculation of the hadronic cross section requires that the partonic processes of gq, $g\bar{q}$, qg, and $\bar{q}g$, where an additional real quark or antiquark (denoted by j, meaning hadronic jet) is in the final state[2], be included as well,

$$\sigma^{\text{LO+NLO}}_{pp\to VH} = \sigma^{\text{LO+NLO}}_{q\bar{q}'\to VH} + \sigma_{gq\to VH+j}. \tag{4.1}$$

4.1 Calculating the $q\bar{q}' \to V^* \to VH$ Processes at NLO QCD

Omitting the decay chain of the V^* boson, the Feynman diagrams needed for the NLO QCD calculation of the $q\bar{q}' \to VH$ are listed in Fig. 4.1. The amplitudes of real emissions (Fig. 4.1(d, e)) can be similarly calculated as the leading order amplitudes, except that they produce two types of infrared (IR) singularities. The soft singularity arises when the energy of the radiated gluon approaches zero, and the collinear singularity arises when the momentum of the radiated gluon becomes parallel with its parent quark. These singularities are canceled by the same types of singularities produced by the virtual correction (Fig. 4.1(b)), as the loop momentum of the gluon may approach zero or become parallel to that of a quark, and by the renormalized parton distribution functions.

The virtual correction also produces ultraviolet (UV) singularity, where the loop momentum approaches infinity. This singularity is dealt with by the chosen renormalization procedure [73], in which a counter term (Fig. 4.1(c)) is

[2]These processes will sometimes be collectively referred to as gq.

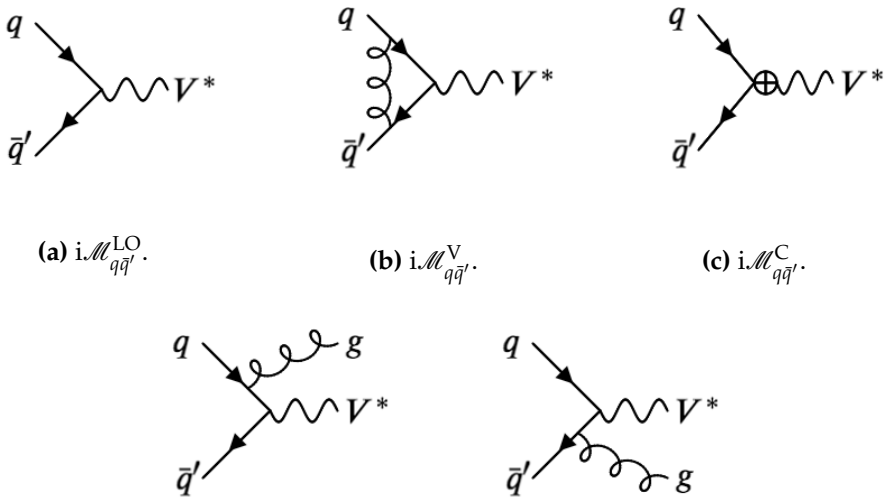

(a) i$\mathscr{M}^{\mathrm{LO}}_{q\bar{q}'}$. **(b)** i$\mathscr{M}^{\mathrm{V}}_{q\bar{q}'}$. **(c)** i$\mathscr{M}^{\mathrm{C}}_{q\bar{q}'}$.

(d) i$\mathscr{M}^{\mathrm{R}_1}_{q\bar{q}'}$. **(e)** i$\mathscr{M}^{\mathrm{R}_2}_{q\bar{q}'}$.

Figure 4.1: Feynman diagrams for (a) the $q\bar{q} \to V^*$ process at LO, (b) one-loop virtual correction in QCD to the LO approximation, (c) UV counter term for the one-loop correction to the $q\bar{q}'V$ vertex, and (d, e) real emissions of gluon from the initial-state quarks. The decay chain of the V boson is not shown for simplicity.

added to cancel this singularity.

The infrared singularities in this calculation are handled in dimensional-reduction scheme, where leading order amplitudes are calculated in spacetime dimension 4, and singularities are regularized by dimensional regularization in dimension $\mathrm{Dim} = 4 - 2\epsilon$. To avoid ambiguity, a subscript of UV or IR may be used to indicate the source of the singularity.

Before explaining each of the diagrams in detail, I am presenting the final expression of the hadronic cross section of the $q\bar{q}' \to VH$ at NLO QCD, in a compact form,

$$
\begin{aligned}
\sigma^{\mathrm{LO+NLO}}_{q\bar{q}\to VH} = \sum_{a,b\in\{q,\bar{q}'\}} \Bigg\{ & \\
& \int \frac{1}{2\hat{s}} \mathrm{d}x_1 \mathrm{d}x_2 \mathrm{PDF}_a(x_1;\mu^2_{\mathrm{Fac}}) \mathrm{PDF}_b(x_2;\mu^2_{\mathrm{Fac}}) \int \Theta(x_1x_2s-\hat{s}) \mathrm{dPS}_{VH+j} \\
& \times \Big[|\mathrm{i}\mathscr{M}^{\mathrm{R}_1}_{ab}(p_a,p_b;p_j,\{p_{\mathrm{f}}\}) + \mathrm{i}\mathscr{M}^{\mathrm{R}_2}_{ab}(p_a,p_b;p_j,\{p_{\mathrm{f}}\})|^2 \\
& \quad - \boldsymbol{V}^{ag,b} |\mathscr{M}^{\mathrm{LO}}_{ab}(p'_a,p_b;\{p'_{\mathrm{f}}\})|^2 - \boldsymbol{V}^{bg,a} |\mathscr{M}^{\mathrm{LO}}_{ab}(p_a,p''_b;\{p''_{\mathrm{f}}\})|^2 \Big] \\
+ & \int \frac{1}{2\hat{s}} \mathrm{d}x_1 \mathrm{d}x_2 \mathrm{PDF}_a(x_1;\mu^2_{\mathrm{Fac}}) \mathrm{PDF}_b(x_2;\mu^2_{\mathrm{Fac}}) \int \Theta(x_1x_2s-\hat{s}) \mathrm{dPS}_{VH} \\
& \times \Big[|\mathrm{i}\mathscr{M}^{\mathrm{LO}}_{ab} + \mathrm{i}\mathscr{M}^{\mathrm{V}}_{ab}(\epsilon) + \mathrm{i}\mathscr{M}^{\mathrm{C}}_{ab}(\epsilon)|^2 + |\mathscr{M}^{\mathrm{LO}}_{ab}|^2 \boldsymbol{I}_{ab}(\epsilon) \Big] \\
+ \sum_{a'} & \int \mathrm{d}x_1 \mathrm{d}x_2 \int_0^1 \mathrm{d}x \frac{1}{2\hat{s}} \mathrm{PDF}_a(x_1;\mu^2_{\mathrm{Fac}}) \mathrm{PDF}_b(x_2;\mu^2_{\mathrm{Fac}}) \int \Theta(xx_1x_2s-\hat{s}) \mathrm{dPS}_{VH}
\end{aligned}
$$

$$\times \left[\boldsymbol{K}^{a,a'}(x) |\mathscr{M}^{\mathrm{LO}}_{a'b}(xp_a, p_b)|^2 + \boldsymbol{P}^{a,a'}(xp_a, x; \mu^2_{\mathrm{Fac}}) |\mathscr{M}^{\mathrm{LO}}_{a'b}(xp_a, p_b)|^2 \right]$$

$$+ \sum_{b'} \int \mathrm{d}x_1 \mathrm{d}x_2 \int_0^1 \mathrm{d}x \frac{1}{2\hat{s}} \mathrm{PDF}_a(x_1; \mu^2_{\mathrm{Fac}}) \mathrm{PDF}_b(x_2; \mu^2_{\mathrm{Fac}}) \int \Theta(xx_1x_2s - \hat{s}) \mathrm{dPS}_{VH}$$

$$\times \left[\boldsymbol{K}^{b,b'}(x) |\mathscr{M}^{\mathrm{LO}}_{ab'}(p_a, xp_b)|^2 + \boldsymbol{P}^{b,b'}(xp_b, x; \mu^2_{\mathrm{Fac}}) |\mathscr{M}^{\mathrm{LO}}_{ab'}(p_a, xp_b)|^2 \right] \Bigg\}. \quad (4.2)$$

The first term has the "dipole contributions", which contains the splitting functions $\boldsymbol{V}$, subtracted from the contributions due to real emissions. The "dipole contributions" approach the infrared singularities in a similar manner as real emissions, and thus systematically and smoothly eliminate these singularities. However, because the cancellations take place numerically, and that the "dipole contributions" depend on sets of momenta derived from but not identical to those for the real emissions, mis-binning, where supposedly canceling large values get filled into the adjacent bins of a histogram, could occur. As a result, special treatments, to be discussed later in Section 4.3.1, can be employed to improve the quality of the histograms.

The subtracted "dipole contributions" are compensated by the contributions due to $\boldsymbol{I}$, $\boldsymbol{K}$, and $\boldsymbol{P}$ operators. The $\boldsymbol{I}$ contribution contains the above infrared singularities parameterized by ϵ_{IR}, which are canceled analytically by those in the virtual correction and renormalization counter term. The $\boldsymbol{K}$ and $\boldsymbol{P}$ contributions are by themselves not singular, which account for compensating the rest of the "dipole contributions" as well as PDF renormalization.

The ultraviolet singularity is dealt entirely in the second term of Eq. (4.2), where the ultraviolet singularity due to the virtual correction i$\mathscr{M}^{\mathrm{V}}_{q\bar{q}'}$, parameterized by ϵ_{UV}, is canceled analytically by that in the renormalization counter

Fig.4.1	$\frac{1}{\epsilon_{\rm UV}}$	$\frac{1}{\epsilon_{\rm IR}}$				$\frac{1}{\epsilon_{\rm IR}^2}$
(a)		$2\,\mathbb{R}\mathrm{e}\left\{(\mathrm{i}\mathscr{M}^{\rm LO})^* \times (\mathrm{i}\mathscr{M}^{\rm V} + \mathrm{i}\mathscr{M}^{\rm C})\right\}$				
(b)	$\mathrm{i}\mathscr{M}^{\rm V}_{ab}$					
(c)	$\mathrm{i}\mathscr{M}^{\rm C}_{ab}$					
(d)		$\lvert\mathrm{i}\mathscr{M}^{\rm R_1}_{ab} + \mathrm{i}\mathscr{M}^{\rm R_2}_{ab}\rvert^2$	$\boldsymbol{V}^{ag,b}\lvert\mathscr{M}^{\rm LO}_{ab}\rvert^2$	$\boldsymbol{K}^{a,a'}\lvert\mathscr{M}^{\rm LO}_{a'b}\rvert^2,\ \boldsymbol{P}^{a,a'}\lvert\mathscr{M}^{\rm LO}_{a'b}\rvert^2$	$\lvert\mathscr{M}^{\rm LO}_{ab}\rvert^2\boldsymbol{I}_{ab}$	
(e)			$\boldsymbol{V}^{bg,a}\lvert\mathscr{M}^{\rm LO}_{ab}\rvert^2$	$\boldsymbol{K}^{b,b'}\lvert\mathscr{M}^{\rm LO}_{ab'}\rvert^2,\ \boldsymbol{P}^{b,b'}\lvert\mathscr{M}^{\rm LO}_{ab'}\rvert^2$		

Table 4.1: Terms of divergences in the NLO QCD calculation of the $q\bar{q}' \to VH$ processes. Terms of divergence regularized by the same parameter are listed in the same column. Terms on the same row have divergence(s) from the same Feynman diagrams. Terms whose sum is finite are connected. Note that the cancellation of the $\frac{1}{\epsilon_{\rm UV}}$ divergence takes place at the amplitude level while the others the level of partonic cross section.

term $\mathrm{i}\mathscr{M}^{\rm C}_{q\bar{q}'}$. Again, the part of the infrared singularities that are parameterized by $\epsilon_{\rm IR}$ is also canceled within the second term.

In Table 4.1, the sources of UV and IR divergences in the Feynman diagrams and the corresponding terms in the final expression are summarized, which shows how divergences regularized by each parameter get canceled.

The parton combination ab in Eq. (4.2) is summed over all of the applicable that produce the specific VH final states, and the summation over a' and b' are such that $a'b$ and ab' lead to the same VH final states. In Table 4.2, all of the partonic combinations of ab as well as their corresponding applicable $a'b$ and ab' are listed for ZH and $W^{\pm}H$ processes. Note that an identity CKM matrix as an approximation can lead to great simplification in the calculation.

ZH	ab	$d\bar{d}$	$u\bar{u}$	$s\bar{s}$	$c\bar{c}$	$b\bar{b}$	$\bar{d}d$	$\bar{u}u$	$\bar{s}s$	$\bar{c}c$	$\bar{b}b$
	aa'	dd	uu	ss	cc	bb	$\bar{d}\bar{d}$	$\bar{u}\bar{u}$	$\bar{s}\bar{s}$	$\bar{c}\bar{c}$	$\bar{b}\bar{b}$
	bb'	$\bar{d}\bar{d}$	$\bar{u}\bar{u}$	$\bar{s}\bar{s}$	$\bar{c}\bar{c}$	$\bar{b}\bar{b}$	dd	uu	ss	cc	bb

W^+H	ab	$\bar{d}u$	$\bar{d}c$	$\bar{s}u$	$\bar{s}c$	$\bar{b}u$	$\bar{b}c$
	aa'	$\bar{d}\bar{d}$, $\bar{d}\bar{s}$, $\bar{d}\bar{b}$	$\bar{d}\bar{d}$, $\bar{d}\bar{s}$, $\bar{d}\bar{b}$	$\bar{s}\bar{d}$, $\bar{s}\bar{s}$, $\bar{s}\bar{b}$	$\bar{s}\bar{d}$, $\bar{s}\bar{s}$, $\bar{s}\bar{b}$	$\bar{b}\bar{d}$, $\bar{b}\bar{s}$, $\bar{b}\bar{b}$	$\bar{b}\bar{d}$, $\bar{b}\bar{s}$, $\bar{b}\bar{b}$
	bb'	uu, uc	cu, cc	uu, uc	cu, cc	uu, uc	cu, cc
	ab	$u\bar{d}$	$c\bar{d}$	$u\bar{s}$	$c\bar{s}$	$u\bar{b}$	$c\bar{b}$
	aa'	uu, uc	cu, cc	uu, uc	cu, cc	uu, uc	cu, cc
	bb'	$\bar{d}\bar{d}$, $\bar{d}\bar{s}$, $\bar{d}\bar{b}$	$\bar{d}\bar{d}$, $\bar{d}\bar{s}$, $\bar{d}\bar{b}$	$\bar{s}\bar{d}$, $\bar{s}\bar{s}$, $\bar{s}\bar{b}$	$\bar{s}\bar{d}$, $\bar{s}\bar{s}$, $\bar{s}\bar{b}$	$\bar{b}\bar{d}$, $\bar{b}\bar{s}$, $\bar{b}\bar{b}$	$\bar{b}\bar{d}$, $\bar{b}\bar{s}$, $\bar{b}\bar{b}$
W^-H	ab	$d\bar{u}$	$d\bar{c}$	$s\bar{u}$	$s\bar{c}$	$b\bar{u}$	$b\bar{c}$
	aa'	dd, ds, db	dd, ds, db	sd, ss, sb	sd, ss, sb	bd, bs, bb	bd, bs, bb
	bb'	$\bar{u}\bar{u}$, $\bar{u}\bar{c}$	$\bar{c}\bar{u}$, $\bar{c}\bar{c}$	$\bar{u}\bar{u}$, $\bar{u}\bar{c}$	$\bar{c}\bar{u}$, $\bar{c}\bar{c}$	$\bar{u}\bar{u}$, $\bar{u}\bar{c}$	$\bar{c}\bar{u}$, $\bar{c}\bar{c}$
	ab	$\bar{u}d$	$\bar{c}d$	$\bar{c}s$	$\bar{c}s$	$\bar{u}b$	$\bar{c}b$
	aa'	$\bar{u}\bar{u}$, $\bar{u}\bar{c}$	$\bar{c}\bar{u}$, $\bar{c}\bar{c}$	$\bar{u}\bar{u}$, $\bar{u}\bar{c}$	$\bar{c}\bar{u}$, $\bar{c}\bar{c}$	$\bar{u}\bar{u}$, $\bar{u}\bar{c}$	$\bar{c}\bar{u}$, $\bar{c}\bar{c}$
	bb'	dd, ds, db	dd, ds, db	sd, ss, sb	sd, ss, sb	bd, bs, bb	bd, bs, bb

Table 4.2: Partonic combinations ab as well as the applicable superscripts $a'b$ and ab' of the $\boldsymbol{K}$ and $\boldsymbol{P}$ functions, for ZH and $W^{\pm}H$ processes.

The color algebra needed for the calculation of the $q\bar{q}' \to VH$ calculation is provided in Section 3.2 and Appendix A of Ref. [72]. In fact, since the LO Feynman diagrams of the $q\bar{q}' \to VH$ processes have only two color-charged initial-state partons[3], all of the color factors needed in this thesis are,

$$\mathrm{Tr}[t^a t^b] = \delta^{ab} T_R = \delta^{ab} \frac{1}{2} , \tag{4.3}$$

[3]While the decay products of V and H can be quarks, the color correlations between the initial- and final-state quarks is not considered.

$$\boldsymbol{T}_g \cdot \boldsymbol{T}_g = N_c = 3\,, \tag{4.4}$$

$$\boldsymbol{T}_q \cdot \boldsymbol{T}_q = C_F = \frac{(N_c^2 - 1)}{2N_c} = \frac{4}{3}\,, \tag{4.5}$$

$$\boldsymbol{T}_i \cdot \boldsymbol{T}_j = \boldsymbol{T}_j \cdot \boldsymbol{T}_i\,, \tag{4.6}$$

$$\boldsymbol{T}_1 \cdot \boldsymbol{T}_2|1,2> \;=\; -\boldsymbol{T}_1 \cdot \boldsymbol{T}_1|1,2> \;=\; -\boldsymbol{T}_1^2|1,2> \;=\; -\boldsymbol{T}_2^2|1,2>\,, \tag{4.7}$$

$$\frac{\boldsymbol{T}_q \cdot \boldsymbol{T}_{\bar{q}}}{\boldsymbol{T}_q^2} = \frac{\boldsymbol{T}_q \cdot \boldsymbol{T}_{\bar{q}}}{\boldsymbol{T}_{\bar{q}}^2} = \frac{\boldsymbol{T}_{\bar{q}} \cdot \boldsymbol{T}_q}{\boldsymbol{T}_q^2} = \frac{\boldsymbol{T}_{\bar{q}} \cdot \boldsymbol{T}_q}{\boldsymbol{T}_{\bar{q}}^2} = -1\,. \tag{4.8}$$

The helicity amplitudes of the NLO real corrections to the $q\bar{q}' \to VH$ processes can be calculated by the same manner used to calculate the LO $q\bar{q}' \to VH$ amplitudes, which uses FORM [44] with the SPINNEY package [45], and will not be presented in detail here (see Section. 2.4). The real corrections require an additional final-state particle to the $q\bar{q}' \to V^* \to VH \to f\bar{f}'b\bar{b}$ phase space. This can be accomplished by one additional splitting of $12345 \to 1234, 5$, with 5 being the particle of real emission (see Section 2.1 for details). It is worth noting that in the real emission amplitudes, infrared singularities appear in the terms that contain the factor of

$$\frac{1}{2p_a.p_r} = \frac{1}{2E_aE_r(1-\cos\theta_{ar})}, \tag{4.9}$$

where $p_{a,b}$ $(E_{a,b})$ are the momenta (energies) of the initial-state partons, p_r (E_r) is the momentum (energy) of the radiated parton, and $\cos\theta_{ar}$ is the angle between partons a and r. Soft singularity occurs as $E_r \to 0$, and colinear singularity occurs as $\cos\theta_{ar} \to 1$. When the real emission amplitudes are evaluated numerically, numerical stability is ensured by not allowing $\frac{p_a.p_r}{p_a.p_b}$ to

reach below machine precision.

Each contribution due to one of the two real emission diagrams (Fig. 4.1(d, e)) has a corresponding dipole contribution to be subtracted. The splitting operators $\boldsymbol{V}$ inside the dipole contributions presented in this chapter have absorbed and factor of -1 due to Eq. (4.8), and with the understanding that the splitting operators yield nonzero outcome only when sandwiched between the states with the same helicities, those needed for the $q\bar{q}' \to VH$ processes become functions,

$$\begin{aligned}\boldsymbol{V}^{ag,b} =& \frac{1}{s_{ag}} \frac{1}{x_{g,ab}} 8\pi\mu_{\text{Fac}}^{2\epsilon_{\text{IR}}} \alpha_{\text{S}} C_F \left[\frac{2}{1 - x_{g,ab}} - (1 + x_{g,ab}) - \epsilon_{\text{IR}}(1 - x_{g,ab}) \right] \\ =& \frac{1}{s_{ag}} \frac{1}{x_{g,ab}} 8\pi\alpha_{\text{S}} C_F \left[\frac{2}{1 - x_{g,ab}} - (1 + x_{g,ab}) \right] + \mathcal{O}(\epsilon_{\text{IR}}) \end{aligned} \tag{4.10}$$

where

$$x_{g,ab} = \frac{p_a.p_b - p_g.p_a - p_g.p_b}{p_a.p_b}. \tag{4.11}$$

Denoting $p_a, p_b, p_j, \{p_{\text{f}}\}$ the set of momenta for the scattering of initial-state partons a and b, which results in the final-state momenta p_{f} and an additional parton j radiated from a, the momenta for the corresponding dipole contribution are

$$p_a \to p'_a = x_{g,ab}\, p_a, \tag{4.12}$$

$$p_b \to p_b, \tag{4.13}$$

$$\text{and} \quad p_{\text{f}}^{\mu} \to p_{\text{f}}^{\mu\prime} = \Lambda^{\mu}_{\nu}(K, \widetilde{K})\, p_{\text{f}}^{\nu}, \tag{4.14}$$

where

$$K^\mu = p_a^\mu + p_b^\mu - p_j^\mu, \tag{4.15}$$

$$\widetilde{K}^\mu = p_a' + p_b^\mu, \tag{4.16}$$

$$\text{and} \quad \Lambda_\nu^\mu\left(K, \widetilde{K}\right) = g_\nu^\mu - \frac{2\left(\widetilde{K}+K\right)^\mu \left(\widetilde{K}+K\right)_\nu}{\left(\widetilde{K}+K\right)^2} - \frac{2\widetilde{K}^\mu K_\nu}{K^2}. \tag{4.17}$$

The matrix $\Lambda_\nu^\mu\left(K, \widetilde{K}\right)$ generates a proper Lorentz transformation such that momentum conservation without the radiated parton is obtained,

$$p_a' + p_b = \sum_{\mathrm{f}} p_{\mathrm{f}}'. \tag{4.18}$$

The momenta for the dipole contribution corresponding to that j radiated from b can be obtained in the same manner.

Note that the dipole contributions share the same flux factor $\frac{1}{\hat{s}}$ and the same phase space weight with those of the real emission. However, should any phase space cuts be employed, the derived momenta need to be checked against the same selection criteria. When dynamic scale is employed in Monte-Carlo simulation, the renormalization and factorization scales need to be reevaluated based on the derived momenta, and PDF's need to be reevaluated for the dipole contributions.

With the computational techniques introduced in the previous chapters, in particular the Passarino-Veltman tensor integral reduction, the one-loop virtual correction to the LO amplitude can be found as

$$\mathrm{i}\mathscr{M}^{\mathrm{V}} = \mathrm{i}\mathscr{M}^{\mathrm{LO}}\ (-\mathrm{i})16\pi\alpha_{\mathrm{S}}C_F\left[B_0(0,0;0;\mathrm{Dim}) - \frac{3}{4}B_0(0,0;(p_a+p_b);\mathrm{Dim})\right.$$

$$-\frac{1}{2}\epsilon_{\mathrm{UV}} B_0(0,0;(p_a+p_b);\mathrm{Dim}) - \frac{1}{2} s_{ab} C_0(0,0,0;0,(p_a+p_b),0;\mathrm{Dim})\Big], \tag{4.19}$$

where the functions B_0 and C_0 were defined in Eq. (3.7 and 3.8), and

$$s_{ab} \equiv 2(p_a.p_b). \tag{4.20}$$

The amplitude of the virtual correction is found to be proportional to the leading order amplitude. This is not a general feature in NLO calculations, but turns out to be convenient. The analytical expressions of the scalar integrals can be found in Section 4.3.2 of Ref. [58] and Eq. (B.16) of Ref. [61][4],

$$\begin{aligned} &B_0(0,0;0;\mathrm{Dim}) \\ =&\frac{\mathrm{i}\pi^2}{(2\pi)^4}\left(\frac{\Gamma(1+\epsilon_{\mathrm{UV}})(4\pi)^{\epsilon_{\mathrm{UV}}}}{\epsilon_{\mathrm{UV}}} - \frac{\Gamma(1+\epsilon_{\mathrm{IR}})(4\pi)^{\epsilon_{\mathrm{IR}}}}{\epsilon_{\mathrm{IR}}} + \mathcal{O}(\epsilon_{\mathrm{IR}})\right), \end{aligned} \tag{4.21}$$

$$\begin{aligned} &B_0(0,0;(p_a+p_b);\mathrm{Dim}) \\ =&\frac{\mathrm{i}\pi^2}{(2\pi)^4}\left[2 - \ln\frac{(s_{ab}-\mathrm{i}0)}{\mu^2_{\mathrm{Ren}}} + \frac{\Gamma(1+\epsilon_{\mathrm{UV}})(4\pi)^{\epsilon_{\mathrm{UV}}}}{\epsilon_{\mathrm{UV}}} + \mathcal{O}(\epsilon_{\mathrm{IR}})\right], \end{aligned} \tag{4.22}$$

$$\begin{aligned} &C_0(0,0,0;0,p_a+p_b,0;\mathrm{Dim}) \\ =&\frac{\mathrm{i}\pi^2}{(2\pi)^4}\frac{1}{s_{ab}}\left[\frac{\Gamma(1+\epsilon_{\mathrm{IR}})}{{\epsilon_{\mathrm{IR}}}^2}\left(\frac{4\pi\mu^2_{\mathrm{Ren}}}{-s_{ab}-\mathrm{i}0}\right)^{\epsilon_{\mathrm{IR}}} - \frac{\pi^2}{6} + \mathcal{O}(\epsilon_{\mathrm{IR}})\right]. \end{aligned} \tag{4.23}$$

The renormalization counter term for the above virtual amplitude is constructed using Eq. (2.25, 27, and 28) of Ref. [73],

[4]Note that the tensor and scalar integrals in both Ref. [58] and Ref. [61] have omitted a factor of $\mathrm{i}\pi^2/(2\pi)^4$, which is not omitted in this thesis.

$$\mathrm{i}\mathscr{M}^{\mathrm{C}} = \mathrm{i}\mathscr{M}^{\mathrm{LO}}\,\frac{\alpha_{\mathrm{S}}}{\pi}C_F\Big[\frac{\Gamma(1+\epsilon_{\mathrm{IR}})(4\pi)^{\epsilon_{\mathrm{IR}}}}{4\epsilon_{\mathrm{IR}}} - \frac{\Gamma(1+\epsilon_{\mathrm{UV}})(4\pi)^{\epsilon_{\mathrm{UV}}}}{4\epsilon_{\mathrm{UV}}} + \mathscr{O}(\epsilon)\Big], \tag{4.24}$$

where the ratios of energy scales are set to be 1.

The renormalization counter term eliminates the UV divergence in the virtual correction. In anticipating that the rest of the infrared singularities will be canceled by the $\boldsymbol{I}$ contribution, and that in Ref. [72] a factor of

$$\frac{(4\pi)^{\epsilon}}{\Gamma(1-\epsilon)} = 1 + \mathscr{O}(\epsilon) \quad \to 1\ (\epsilon \to 0) \tag{4.25}$$

is pulled outside the rest of the expression of $\boldsymbol{I}$, it is necessary to apply the same ϵ-normalization to the virtual correction and renormalization counter term above so that the non-singular contributions are consistent. In doing this, no γ_{E} will make appearance in the expression of the non-singular part of each of the contributions mentioned above. The sum of the virtual correction and the renormalization counter term reads,

$$\begin{aligned}
&\mathrm{i}\mathscr{M}^{\mathrm{NLO}}_{\text{UV-safe}} \\
=&\mathrm{i}\mathscr{M}^{\mathrm{V}} + \mathrm{i}\mathscr{M}^{\mathrm{C}} = \mathrm{i}\mathscr{M}^{\mathrm{LO}}\,\frac{\alpha_{\mathrm{S}}}{\pi}C_F\frac{(4\pi)^{\epsilon_{\mathrm{IR}}}}{\Gamma(1-\epsilon_{\mathrm{IR}})} \\
\times&\Big\{-\frac{3}{4}\Big[2 - \ln\frac{(s_{ab}+\mathrm{i}0)}{\mu^2_{\mathrm{Ren}}}\Big] - \frac{1}{2} - \frac{1}{4}\ln^2\frac{\mu^2_{\mathrm{Ren}}}{(-s_{ab}-\mathrm{i}0)} \\
&-\frac{3}{4\epsilon_{\mathrm{IR}}} - \frac{1}{2\epsilon_{\mathrm{IR}}}\ln\frac{\mu^2_{\mathrm{Ren}}}{-s_{ab}-\mathrm{i}0} - \frac{1}{2{\epsilon_{\mathrm{IR}}}^2} + \mathscr{O}(\epsilon)\Big\}.
\end{aligned} \tag{4.26}$$

With the UV divergence taken care of, the UV-safe squared amplitude with

one-loop virtual correction is

$$
\begin{aligned}
&|\mathscr{M}^{\text{LO+NLO}}|^2_{\text{UV-safe}} = |\mathrm{i}\mathscr{M}^{\text{LO}} + \mathrm{i}\mathscr{M}^{\text{NLO}}_{\text{UV-safe}}|^2 \\
=&|\mathscr{M}^{\text{LO}}|^2 + 2\,\mathbb{R}\mathrm{e}\left\{(\mathrm{i}\mathscr{M}^{\text{LO}})^* \times (\mathrm{i}\mathscr{M}^{\text{NLO}}_{\text{UV-safe}})\right\} + \mathcal{O}(\alpha_{\text{S}}^2).
\end{aligned} \tag{4.27}
$$

Omitting $\mathcal{O}(\alpha_{\text{S}}^2)$, it is convenient to introduce the shorthand notation,

$$
\begin{aligned}
&|\mathscr{M}|^2_{\text{NLO,UV-safe}} \\
\equiv&2\,\mathbb{R}\mathrm{e}\left\{(\mathrm{i}\mathscr{M}^{\text{LO}})^* \times (\mathrm{i}\mathscr{M}^{\text{NLO}}_{\text{UV-safe}})\right\} \\
=&|\mathscr{M}^{\text{LO}}|^2\,\frac{\alpha_{\text{S}}}{\pi}C_F 2\left[\frac{(4\pi)^\epsilon}{\Gamma(1-\epsilon)}\right]\left[-\frac{3}{4}\left(2-\ln\frac{s_{ab}}{\mu^2_{\text{Ren}}}\right)-\frac{1}{2}-\frac{1}{4}\left(\ln^2\frac{s_{ab}}{\mu^2_{\text{Ren}}}-\pi^2\right)\right] \\
-&|\mathscr{M}^{\text{LO}}|^2\,\frac{\alpha_{\text{S}}}{\pi}C_F\left[\frac{(4\pi)^\epsilon}{\Gamma(1-\epsilon)}\right]\frac{1}{2{\epsilon_{\text{IR}}}^2} \\
-&|\mathscr{M}^{\text{LO}}|^2\,\frac{\alpha_{\text{S}}}{\pi}C_F\left[\frac{(4\pi)^\epsilon}{\Gamma(1-\epsilon)}\right]\frac{1}{\epsilon_{\text{IR}}}\left(\frac{1}{2}\ln\frac{\mu^2_{\text{Ren}}}{s_{ab}}+\frac{3}{4}\right).
\end{aligned} \tag{4.28}
$$

The $\boldsymbol{I}$ contribution with any applicable $q\bar{q}'$ combination ab is

$$
\begin{aligned}
&\left[\boldsymbol{I}\textbf{ contribution for }q\bar{q}\right] \\
\equiv&\int\frac{1}{2\hat{s}}\mathrm{d}x_1\mathrm{d}x_2\mathrm{PDF}_a(x_1;\mu^2_{\text{Fac}})\mathrm{PDF}_b(x_2;\mu^2_{\text{Fac}}) \\
&\times\int\Theta(x_1x_2s-\hat{s})\mathrm{dPS}_{VH}\left[|\mathscr{M}^{\text{LO}}_{ab}|^2\boldsymbol{I}_{ab}(\epsilon_{\text{IR}})\right] \\
=&\int\frac{1}{2\hat{s}}\mathrm{d}x_1\mathrm{d}x_2\mathrm{PDF}_a(x_1;\mu^2_{\text{Fac}})\mathrm{PDF}_b(x_2;\mu^2_{\text{Fac}}) \\
&\times\int\Theta(x_1x_2s-\hat{s})\mathrm{dPS}_{VH}|\mathscr{M}^{\text{LO}}_{ab}|^2\frac{\alpha_{\text{S}}}{2\pi}C_F\left[\frac{(4\pi)^\epsilon}{\Gamma(1-\epsilon)}\right]
\end{aligned}
$$

$$\times \left[\left(10 - \pi^2 + 3 \ln \frac{\mu_{\rm Fac}^2}{s_{ab}} + \ln^2 \frac{\mu_{\rm Fac}^2}{s_{ab}} \right) + \frac{1}{{\epsilon_{\rm IR}}^2} + \frac{1}{\epsilon_{\rm IR}} \left(\ln \frac{\mu_{\rm Fac}^2}{s_{ab}} + \frac{3}{2} \right) - 1 \right] \tag{4.29}$$

The last -1 in Eq. (4.29) is due to the translation from the conventional dimensional-regularization scheme used in Ref. [72] to the dimensional-reduction scheme[5]. The divergences of $\frac{1}{\epsilon_{\rm IR}}$ and $\frac{1}{{\epsilon_{\rm IR}}^2}$ in Eq. (4.28) and Eq. (4.29) cancel when these two expressions are combined at the squared-matrix-element level.

The explicit expression of the contribution to the $q\bar{q}'$ processes from the $\boldsymbol{K}$ operators is

$$\begin{aligned}
&\left[\boldsymbol{K}\ \textbf{contribution for}\ q\bar{q}\right] \\
&\equiv \sum_{a'} \int \mathrm{d}x_1 \mathrm{d}x_2 \int_0^1 \mathrm{d}x \frac{1}{2\hat{s}} \mathrm{PDF}_a(x_1;\mu_{\rm Fac}^2) \mathrm{PDF}_b(x_2;\mu_{\rm Fac}^2) \\
&\quad \times \int \Theta(x x_1 x_2 s - \hat{s}) \mathrm{dPS}_{VH} \left[\boldsymbol{K}^{a,a'}(x) |\mathscr{M}_{a'b}^{\rm LO}(x p_a, p_b)|^2 \right] \\
&+ \sum_{b'} \int \mathrm{d}x_1 \mathrm{d}x_2 \int_0^1 \mathrm{d}x \frac{1}{2\hat{s}} \mathrm{PDF}_a(x_1;\mu_{\rm Fac}^2) \mathrm{PDF}_b(x_2;\mu_{\rm Fac}^2) \\
&\quad \times \int \Theta(x x_1 x_2 s - \hat{s}) \mathrm{dPS}_{VH} \left[\boldsymbol{K}^{b,b'}(x) |\mathscr{M}_{ab'}^{\rm LO}(p_a, x p_b)|^2 \right] \\
&= \sum_{a'} \int \mathrm{d}x_1 \mathrm{d}x_2 \int_0^1 \mathrm{d}x \frac{1}{2\hat{s}} \mathrm{PDF}_a(x_1;\mu_{\rm Fac}^2) \mathrm{PDF}_b(x_2;\mu_{\rm Fac}^2) \\
&\quad \times \int \Theta(x x_1 x_2 s - \hat{s}) \mathrm{dPS}_{VH} |\mathscr{M}_{a'b}^{\rm LO}(x p_a, p_b)|^2
\end{aligned} \tag{4.30}$$

[5] See Note added at the end of Ref. [72].

$$\times \frac{\alpha_S}{2\pi} C_F \Bigg\{ \left[\frac{2}{1-x} \ln \frac{(1-x)^2}{x} \right]_+ + \left[-(1+x) \ln \frac{(1-x)^2}{x} + (1-x) \right] + \delta(1-x) \left[\frac{2\pi^2}{3} - 5 \right] \Bigg\}$$

$$+ \big[(a,1) \longleftrightarrow (b,2) \big]. \tag{4.31}$$

The "+" prescription denotes the plus distribution,

$$\int_0^1 \mathrm{d}x \, g(x) \big[f(x) \big]_+ \equiv \int_0^1 \mathrm{d}x \big[g(x) - g(1) \big] f(x). \tag{4.32}$$

Consequently,

$$\big[\boldsymbol{K} \textbf{ contribution for } q\bar{q} \big]$$

$$= \sum_{a'} \int \mathrm{d}x_1 \mathrm{d}x_2 \int_0^1 \mathrm{d}x \frac{1}{2\hat{s}} \mathrm{PDF}_a(x_1; \mu_{\mathrm{Fac}}^2) \mathrm{PDF}_b(x_2; \mu_{\mathrm{Fac}}^2)$$

$$\times \int \Theta(x x_1 x_2 s - \hat{s}) \mathrm{dPS}_{VH} |\mathscr{M}_{a'b}^{\mathrm{LO}}(x p_a, p_b)|^2$$

$$\times \frac{\alpha_S}{2\pi} C_F \left[\frac{2}{1-x} \ln \frac{(1-x)^2}{x} - (1+x) \ln \frac{(1-x)^2}{x} + (1-x) \right]$$

$$+ \sum_{a'} \int \mathrm{d}x_1 \mathrm{d}x_2 \int_0^1 \mathrm{d}x \frac{1}{2\hat{s}} \mathrm{PDF}_a(x_1; \mu_{\mathrm{Fac}}^2) \mathrm{PDF}_b(x_2; \mu_{\mathrm{Fac}}^2)$$

$$\times \int \Theta(x_1 x_2 s - \hat{s}) \mathrm{dPS}_{VH} |\mathscr{M}_{a'b}^{\mathrm{LO}}(p_a, p_b)|^2 \frac{\alpha_S}{2\pi} C_F \left[\frac{-2}{1-x} \ln \frac{(1-x)^2}{x} \right]$$

$$+ \sum_{a'} \int \mathrm{d}x_1 \mathrm{d}x_2 \frac{1}{2\hat{s}} \mathrm{PDF}_a(x_1; \mu_{\mathrm{Fac}}^2) \mathrm{PDF}_b(x_2; \mu_{\mathrm{Fac}}^2)$$

$$\times \int \Theta(x_1 x_2 s - \hat{s}) \mathrm{dPS}_{VH} |\mathscr{M}_{a'b}^{\mathrm{LO}}(p_a, p_b)|^2 \frac{\alpha_S}{2\pi} C_F \left[\frac{2\pi^2}{3} - 5 \right]$$

$$+\big[(a,1) \longleftrightarrow (b,2)\big]. \tag{4.33}$$

Notice that in applying the plus distribution in Eq. (4.32) to the $\boldsymbol{K}$ contribution in Eq. (4.31), as x approaches 1, both the numerator and denominator approaches 0, and the integral is finite. However, to allow numerical stability when the integral is evaluated numerically, one needs to set a cutoff value that keeps x from being too close to 1. In addition, turning Eq. (4.31) into Eq. (4.33) is needed if one were to fill the histograms of kinematic distributions. This is because, as shown in Eq. (4.33), three sets of momenta, each with initial-state momenta $(p_a,\ p_b)$, $(xp_a,\ p_b)$, and $(p_a,\ xp_b)$ respectively, are involved and each set carries it own weight. The momenta sets of $(xp_a,\ p_b)$ and $(p_a,\ xp_b)$ are obtained by first generating a set of momenta with invariant mass $x\hat{s} = 2xp_a.p_b$, and then a boost from the center-of-mass frame to the laboratory frame using Eq. (2.115) and

$$x_1 \to xx_1 \quad \text{and} \quad x_2 \to xx_2 \tag{4.34}$$

respectively. The momenta sets of $(xp_a,\ p_b)$ and $(p_a,\ xp_b)$ are identical in the center-of-mass frame, and the scattering amplitudes are Lorentz invariant. However, both of the momenta sets are needed if kinematic cuts are to be performed properly.

The explicit expression of the contribution to the $q\bar{q}'$ processes from the $\boldsymbol{P}$ operator is

$$\big[\boldsymbol{P}\ \textbf{contribution}\ \text{for}\ q\bar{q}\big]$$

$$
\begin{aligned}
&= \sum_{a'} \int \mathrm{d}x_1 \mathrm{d}x_2 \int_0^1 \mathrm{d}x \frac{1}{2\hat{s}} \mathrm{PDF}_a(x_1;\mu^2_{\mathrm{Fac}}) \mathrm{PDF}_b(x_2;\mu^2_{\mathrm{Fac}}) \\
&\quad \times \int \Theta(x x_1 x_2 s - \hat{s}) \mathrm{dPS}_{VH} \Big[\boldsymbol{P}^{a,a'}(x, x p_a, \mu^2_{\mathrm{Fac}}) |\mathscr{M}^{\mathrm{LO}}_{a'b}(x p_a, p_b; \{p\})|^2 \Big] \\
&+ \sum_{b'} \int \mathrm{d}x_1 \mathrm{d}x_2 \int_0^1 \mathrm{d}x \frac{1}{2\hat{s}} \mathrm{PDF}_a(x_1;\mu^2_{\mathrm{Fac}}) \mathrm{PDF}_b(x_2;\mu^2_{\mathrm{Fac}}) \\
&\quad \times \int \Theta(x x_1 x_2 s - \hat{s}) \mathrm{dPS}_{VH} \Big[\boldsymbol{P}^{b,b'}(x, x p_b, \mu^2_{\mathrm{Fac}}) |\mathscr{M}^{\mathrm{LO}}_{ab'}(p_a, x p_b; \{p\})|^2 \Big] \\
&= \sum_{a'} \int \mathrm{d}x_1 \mathrm{d}x_2 \int_0^1 \mathrm{d}x \frac{1}{2\hat{s}} \mathrm{PDF}_a(x x_1;\mu^2_{\mathrm{Fac}}) \mathrm{PDF}_b(x_2;\mu^2_{\mathrm{Fac}}) \\
&\quad \times \int \Theta(x x_1 x_2 s - \hat{s}) \mathrm{dPS}_{VH} |\mathscr{M}^{\mathrm{LO}}_{a'b}(x p_a, p_b)|^2 \frac{\alpha_{\mathrm{S}}}{2\pi} C_F(-1) \ln \frac{\mu^2_{\mathrm{Fac}}}{x s_{ab}} \left[\frac{1+x^2}{1-x} \right]_+ \\
&+ \big[(a,1) \longleftrightarrow (b,2) \big] \qquad (4.35) \\
&= \sum_{a'} \int \mathrm{d}x_1 \mathrm{d}x_2 \int_0^1 \mathrm{d}x \frac{1}{2\hat{s}} \mathrm{PDF}_a(x x_1;\mu^2_{\mathrm{Fac}}) \mathrm{PDF}_b(x_2;\mu^2_{\mathrm{Fac}}) \\
&\quad \times \int \Theta(x x_1 x_2 s - \hat{s}) \mathrm{dPS}_{VH} |\mathscr{M}^{\mathrm{LO}}_{a'b}(x p_a, p_b)|^2 \frac{\alpha_{\mathrm{S}}}{2\pi} C_F(-1) \ln \frac{\mu^2_{\mathrm{Fac}}}{x s_{ab}} \left[\frac{1+x^2}{1-x} \right] \\
&+ \sum_{a'} \int \mathrm{d}x_1 \mathrm{d}x_2 \int_0^1 \mathrm{d}x \frac{1}{2\hat{s}} \mathrm{PDF}_a(x_1;\mu^2_{\mathrm{Fac}}) \mathrm{PDF}_b(x_2;\mu^2_{\mathrm{Fac}}) \\
&\quad \times \int \Theta(x_1 x_2 s - \hat{s}) \mathrm{dPS}_{VH} |\mathscr{M}^{\mathrm{LO}}_{a'b}(p_a, p_b)|^2 \frac{\alpha_{\mathrm{S}}}{2\pi} C_F(-1) \ln \frac{\mu^2_{\mathrm{Fac}}}{s_{ab}} \left[-\frac{1+x^2}{1-x} \right] \\
&+ \big[(a,1) \longleftrightarrow (b,2) \big], \qquad (4.36)
\end{aligned}
$$

and the discussion following Eq. (4.33) equally applies here.

4.2 Calculating the $gq \to VH + j$ Processes

The Feynman diagrams relevant to the $gq \to VH + j$ production are listed in Fig. 4.2.

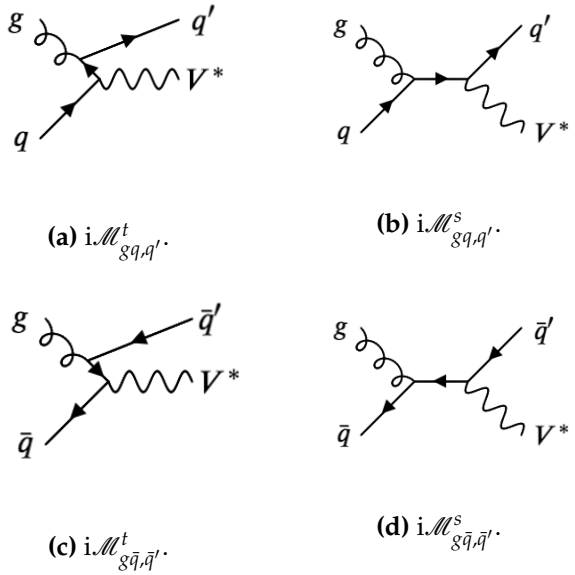

(a) i$\mathscr{M}^{t}_{gq,q'}$.

(b) i$\mathscr{M}^{s}_{gq,q'}$.

(c) i$\mathscr{M}^{t}_{g\bar{q},\bar{q}'}$.

(d) i$\mathscr{M}^{s}_{g\bar{q},\bar{q}'}$.

Figure 4.2: Feynman diagrams of (a, b) gq-initiated process and (c, d) $g\bar{q}$-initiated process. The decay chain of the V boson is not shown for simplicity. Note that 4 more diagrams of i$\mathscr{M}^{t}_{qg,q'}$, i$\mathscr{M}^{s}_{qg,q'}$, i$\mathscr{M}^{t}_{\bar{q}g,\bar{q}'}$, and i$\mathscr{M}^{s}_{\bar{q}g,\bar{q}'}$ are not shown in the figure, and that the superscript of s or t is used to indicate the s- or t-channel shape of a diagram.

Note that in naming the amplitudes, a superscript of s or t is used to describe the s- or t-channel shape of a diagram, telling them apart. The final expression of the total cross section of the $gq \to VH + q'$ processes, in a

compact form, is

$$\sigma_{qg/gq\to VH+q'} + \sigma_{\bar{q}g/g\bar{q}\to VH+\bar{q}'} = \sum_{a,b\in\{q,\bar{q}'\}} \Bigg\{$$

$$\int \mathrm{d}x_1\mathrm{d}x_2 \int \Theta(x_1x_2s-\hat{s})\mathrm{dPS}_{VH+j}\frac{1}{2\hat{s}}\mathrm{PDF}_a(x_1;\mu^2_{\mathrm{Fac}})\mathrm{PDF}_g(x_2;\mu^2_{\mathrm{Fac}})$$

$$\times\left[|\mathrm{i}\mathscr{M}^t_{ag,b}(p_a,p_g;p_b)+\mathrm{i}\mathscr{M}^s_{ag,b}(p_a,p_g;p_b)|^2 - \boldsymbol{V}^{gb,a}|\mathscr{M}^{\mathrm{LO}}_{a\bar{b}}(p_a,p'_g;\{p'\})|^2\right]$$

$$+\int \mathrm{d}x_1\mathrm{d}x_2 \int_0^1 \mathrm{d}x \int \Theta(xx_1x_2s-\hat{s})\mathrm{dPS}_{VH}\frac{1}{2\hat{s}}\mathrm{PDF}_a(x_1;\mu^2_{\mathrm{Fac}})\mathrm{PDF}_g(xx_2;\mu^2_{\mathrm{Fac}})$$

$$\times\left[\boldsymbol{K}^{g,b}(x)|\mathscr{M}^{\mathrm{LO}}_{a\bar{b}}(p_a,xp_g)|^2+\boldsymbol{P}^{g,b}(xp_g,x;\mu^2_{\mathrm{Fac}})|\mathscr{M}^{\mathrm{LO}}_{a\bar{b}}(p_a,xp_g)|^2\right]$$

$$+\int \mathrm{d}x_1\mathrm{d}x_2 \int \Theta(x_1x_2s-\hat{s})\mathrm{dPS}_{VH+j}\frac{1}{2\hat{s}}\mathrm{PDF}_g(x_1;\mu^2_{\mathrm{Fac}})\mathrm{PDF}_a(x_2;\mu^2_{\mathrm{Fac}})$$

$$\times\left[|\mathrm{i}\mathscr{M}^t_{ga,b}(p_g,p_a;p_b)+\mathrm{i}\mathscr{M}^s_{ga,b}(p_g,p_a;p_b)|^2 - \boldsymbol{V}^{gb,a}|\mathscr{M}^{\mathrm{LO}}_{\bar{b}a}(p''_g,p_a;\{p''\})|^2\right]$$

$$+\int \mathrm{d}x_1\mathrm{d}x_2 \int_0^1 \mathrm{d}x \int \Theta(xx_1x_2s-\hat{s})\mathrm{dPS}_{VH}\frac{1}{2\hat{s}}\mathrm{PDF}_g(xx_1;\mu^2_{\mathrm{Fac}})\mathrm{PDF}_a(x_2;\mu^2_{\mathrm{Fac}})$$

$$\times\left[\boldsymbol{K}^{g,a}(x)|\mathscr{M}^{\mathrm{LO}}_{\bar{b}a}(xp_g,p_a)|^2+\boldsymbol{P}^{g,a}(xp_g,x;\mu^2_{\mathrm{Fac}})|\mathscr{M}^{\mathrm{LO}}_{\bar{b}a}(xp_g,p_a)|^2\right]\Bigg\}. \quad (4.37)$$

Notice the consistency among the subscripts of $\mathrm{i}\mathscr{M}^{t,s}$, $\mathrm{i}\mathscr{M}^{\mathrm{LO}}$, and PDF's. The parton combination ab in Eq. (4.37) is summed over all that are applicable to the $ga/ag \to VH+b$ process, and consequently $a\bar{b}$ or $\bar{b}a$ leads to the same VH final states in a leading order Feynman diagram. In Table 4.3, all of the partonic combinations of ab are listed for ZH and $W^{\pm}H$ processes. Like in the case of the $q\bar{q}'$ processes, an diagonal CKM matrix as an approximation can lead to great simplification in the calculation.

ZH	dd	uu	ss	cc	bb	$d\bar{d}$	$u\bar{u}$	$s\bar{s}$	$c\bar{c}$	$b\bar{b}$
W^+H	ud		cd		us		cs		ub	cb
	$\bar{d}\bar{u}$		$\bar{d}\bar{c}$		$\bar{s}\bar{u}$		$\bar{s}\bar{c}$		$\bar{b}\bar{u}$	$\bar{b}\bar{c}$
W^-H	du		dc		su		sc		bu	bc
	$\bar{u}\bar{d}$		$\bar{c}\bar{d}$		$\bar{c}\bar{s}$		$\bar{c}\bar{s}$		$\bar{u}\bar{b}$	$\bar{c}\bar{b}$

Table 4.3: Partonic combinations ab for $ga/ag \to VH + b$ in Eq. (4.37).

The helicity amplitudes of the $gq \to VH + q'$ processes can be calculated by the same manner used to calculate the LO $q\bar{q}' \to VH$ amplitudes, which uses FORM [44] with the SPINNEY package [45], and will not be presented in detail here (see Section. 2.4). The $gq \to VH + q'$ processes require an additional final-state particle to the $q\bar{q}' \to V^* \to VH \to f\bar{f}'b\bar{b}$ phase space. This can be accomplished by one additional splitting of $12345 \to 1234, 5$, with 5 being the particle of real emission (see Section 2.1 for details).

Having absorbed the color factor of -1, the splitting functions $\boldsymbol{V}$ needed for the $gq \to VH + q'$ processes are,

$$\begin{aligned} \boldsymbol{V}^{\boldsymbol{gb,a}}(x_{b,ga}) &= \frac{1}{s_{gb}} \frac{1}{x_{b,ga}} 8\pi\mu_{\text{Fac}}^{2\epsilon_{\text{IR}}} \alpha_{\text{S}} T_R [1 - \epsilon_{\text{IR}} - 2x_{b,ga}(1 - x_{b,ga})] \\ &= -8\pi\alpha_{\text{S}} T_R [1 - 2x_{b,ga}(1 - x_{b,ga})] + \mathcal{O}(\epsilon_{\text{IR}}), \end{aligned} \tag{4.38}$$

where

$$x_{b,ga} = \frac{p_g \cdot p_a - p_b \cdot p_g - p_b \cdot p_a}{p_g \cdot p_a}, \tag{4.39}$$

Considering only the incoming and outgoing nature of the particles and ignoring the particle identities, the treatment of the phase space with an

additional radiated particle is identical to that of the $q\bar{q}'$ processes.

The explicit expression of the contribution to the gq processes from the $\boldsymbol{K}$ operators with the quark combination ab is,

$$
\begin{aligned}
&\left[\boldsymbol{K}\textbf{ contribution for } gq\right] = \sum_{a,b\in\{q,\bar{q}'\}} \Bigg\{ \\
&= \int \mathrm{d}x_1 \mathrm{d}x_2 \int_0^1 \mathrm{d}x \int \Theta(x x_1 x_2 s - \hat{s}) \mathrm{dPS}_{VH} \frac{1}{2\hat{s}} \mathrm{PDF}_a(x_1;\mu^2_{\mathrm{Fac}}) \mathrm{PDF}_{\bar{b}}(x_2;\mu^2_{\mathrm{Fac}}) \\
&\quad \times \left[\boldsymbol{K}^{g,b}(x) |\mathscr{M}^{\mathrm{LO}}_{a\bar{b}}(p_a, x p_g)|^2 \right] \\
&+ \int \mathrm{d}x_1 \mathrm{d}x_2 \int_0^1 \mathrm{d}x \int \Theta(x x_1 x_2 s - \hat{s}) \mathrm{dPS}_{VH} \frac{1}{2\hat{s}} \mathrm{PDF}_{\bar{b}}(x_1;\mu^2_{\mathrm{Fac}}) \mathrm{PDF}_a(x_2;\mu^2_{\mathrm{Fac}}) \\
&\quad \times \left[\boldsymbol{K}^{g,a}(x) |\mathscr{M}^{\mathrm{LO}}_{\bar{b}a}(x p_g, p_a)|^2 \right] \Bigg\} \qquad (4.40) \\
&= \sum_{a,b\in\{q,\bar{q}'\}} \Bigg\{ \int \mathrm{d}x_1 \mathrm{d}x_2 \int_0^1 \mathrm{d}x \int \Theta(x x_1 x_2 s - \hat{s}) \mathrm{dPS}_{VH} \frac{1}{2\hat{s}} \mathrm{PDF}_a(x_1;\mu^2_{\mathrm{Fac}}) \mathrm{PDF}_{\bar{b}}(x_2;\mu^2_{\mathrm{Fac}}) \\
&\quad \times |\mathscr{M}^{\mathrm{LO}}_{a\bar{b}}(p_a, x p_g)|^2 \frac{\alpha_{\mathrm{S}}}{2\pi} T_R \left[\left(x^2 + (1-x)^2\right) \ln \frac{(1-x)^2}{x} + 2x(1-x) \right] \\
&+ \int \mathrm{d}x_1 \mathrm{d}x_2 \int_0^1 \mathrm{d}x \int \Theta(x x_1 x_2 s - \hat{s}) \mathrm{dPS}_{VH} \frac{1}{2\hat{s}} \mathrm{PDF}_{\bar{b}}(x_1;\mu^2_{\mathrm{Fac}}) \mathrm{PDF}_a(x_2;\mu^2_{\mathrm{Fac}}) \\
&\quad \times |\mathscr{M}^{\mathrm{LO}}_{\bar{b}a}(x p_g, p_a)|^2 \frac{\alpha_{\mathrm{S}}}{2\pi} T_R \left[\left(x^2 + (1-x)^2\right) \ln \frac{(1-x)^2}{x} + 2x(1-x) \right] \Bigg\}. \qquad (4.41)
\end{aligned}
$$

The explicit expression of the contribution to the gq processes from the $\boldsymbol{P}$

operators with the quark combination ab is,

$$
\begin{aligned}
&\left[\boldsymbol{P}\textbf{ contribution for } gq\right] = \sum_{a,b\in\{q,\bar{q}'\}} \Bigg\{ \\
&= \int \mathrm{d}x_1 \mathrm{d}x_2 \int_0^1 \mathrm{d}x \int \Theta(x x_1 x_2 s - \hat{s}) \mathrm{dPS}_{VH} \frac{1}{2\hat{s}} \mathrm{PDF}_a(x_1;\mu^2_{\mathrm{Fac}}) \mathrm{PDF}_{\bar{b}}(x_2;\mu^2_{\mathrm{Fac}}) \\
&\quad \times \left[\boldsymbol{P}^{g,b}(x p_g, x; \mu^2_{\mathrm{Fac}}) |\mathscr{M}^{\mathrm{LO}}_{a\bar{b}}(p_a, x p_g)|^2 \right] \\
&+ \int \mathrm{d}x_1 \mathrm{d}x_2 \int_0^1 \mathrm{d}x \int \Theta(x x_1 x_2 s - \hat{s}) \mathrm{dPS}_{VH} \frac{1}{2\hat{s}} \mathrm{PDF}_{\bar{b}}(x_1;\mu^2_{\mathrm{Fac}}) \mathrm{PDF}_a(x_2;\mu^2_{\mathrm{Fac}}) \\
&\quad \times \left[\boldsymbol{P}^{g,a}(x p_g, x; \mu^2_{\mathrm{Fac}}) |\mathscr{M}^{\mathrm{LO}}_{\bar{b}a}(x p_g, p_a)|^2 \right] \Bigg\} \qquad (4.42) \\
&= \sum_{a,b\in\{q,\bar{q}'\}} \Bigg\{ \int \mathrm{d}x_1 \mathrm{d}x_2 \int_0^1 \mathrm{d}x \int \Theta(x x_1 x_2 s - \hat{s}) \mathrm{dPS}_{VH} \frac{1}{2\hat{s}} \mathrm{PDF}_{\bar{b}}(x_1;\mu^2_{\mathrm{Fac}}) \mathrm{PDF}_a(x_2;\mu^2_{\mathrm{Fac}}) \\
&\quad \times |\mathscr{M}^{\mathrm{LO}}_{a\bar{b}}(p_a, x p_g)|^2 \frac{\alpha_{\mathrm{S}}}{2\pi}(-1) T_R \left[x^2 + (1-x)^2 \right] \ln \frac{\mu^2_{\mathrm{Fac}}}{x s_{ab}} \Bigg] \\
&+ \int \mathrm{d}x_1 \mathrm{d}x_2 \int_0^1 \mathrm{d}x \int \Theta(x x_1 x_2 s - \hat{s}) \mathrm{dPS}_{VH} \frac{1}{2\hat{s}} \mathrm{PDF}_{\bar{b}}(x_1;\mu^2_{\mathrm{Fac}}) \mathrm{PDF}_a(x_2;\mu^2_{\mathrm{Fac}}) \\
&\quad \times |\mathscr{M}^{\mathrm{LO}}_{\bar{b}a}(x p_g, p_a)|^2 \frac{\alpha_{\mathrm{S}}}{2\pi}(-1) T_R \left[x^2 + (1-x)^2 \right] \ln \frac{\mu^2_{\mathrm{Fac}}}{x s_{ab}} \Bigg] \Bigg\}. \qquad (4.43)
\end{aligned}
$$

These gq contributions do not involve ultraviolet divergences, and there is no infrared divergences parameterized by ϵ. However, the contribution of real emission (of a quark) has colinear divergence when the momentum of the radiated quark becomes parallel to that of the initial-state gluon. This divergence is canceled by the subtracted dipole contribution, and the latter is compensated by the contributions due to $\boldsymbol{K}$ and $\boldsymbol{P}$ operators. The $\boldsymbol{K}$ and $\boldsymbol{P}$

contribution is also responsible for the PDF renormalization.

4.3 Mis-binning and Treatment

4.3.1 Mis-binning due to Subtraction of Dipole Contributions

In both the next-to-leading order corrections to the $q\bar{q}$-initiated processes, as well as in the gq processes, the infrared divergences due to the radiation of an additional particle is canceled by their respective dipole contribution. The dipole contribution involve a set of momenta derived from that of the real emission, but are not identical, and thus there is a chance of mis-binning when filling their respective weights into histograms of kinematic variables. In Ref. [72], the subtraction is applied to the entire phase space so that its effect is smoothly applied everywhere. However, since the subtraction is meant to have the infrared divergences canceled, it only needs to be applied to the vicinity of the singularities, namely

$$\tilde{v}_{a,r} \equiv \frac{p_a \cdot p_r}{p_a \cdot p_b} \to 0, \tag{4.44}$$

$$\text{and} \quad \tilde{v}_{a,r} \equiv \frac{p_a \cdot p_r}{p_a \cdot p_b} \to 0, \tag{4.45}$$

where $p_{a,b}$ are the momenta of the initial-state partons and p_r is the momentum of the radiated parton.

In Ref. [74], the subtraction method discussed above is modified by the introduction of a parameter $0 \leq \alpha \leq 1$, and the splitting functions in Eqs. (4.10)

and (4.38), respectively, become

$$\begin{aligned}
&\boldsymbol{V}^{ag,b} \to \boldsymbol{V}^{ag,b}(\alpha) \\
=&\frac{1}{s_{ag}}\frac{1}{x_{g,ab}} 8\pi\alpha_S C_F \left[\frac{2}{1-x_{g,ab}} - (1+x_{g,ab})\right]\Theta(\alpha - \tilde{v}_{a,g}) + \mathcal{O}(\epsilon_{\mathrm{IR}}), \qquad (4.46) \\
&\boldsymbol{V}^{\boldsymbol{gb,a}}(x_{b,ga}) \to \boldsymbol{V}^{\boldsymbol{gb,a}}(x_{b,ga};\alpha) \\
=&\frac{1}{s_{gb}}\frac{1}{x_{b,ga}} 8\pi\alpha_S T_R[1 - 2x_{b,ga}(1-x_{b,ga})]\Theta(\alpha - \tilde{v}_{a,g}) + \mathcal{O}(\epsilon_{\mathrm{IR}}). \qquad (4.47)
\end{aligned}$$

The Θ step function dictates that the subtraction would occur only when $v_{a,r}$ is less than α, or when the radiated momentum is sufficiently soft or parallel to its parent particle. When $\alpha = 1$, the original subtraction method is recovered. When α is chosen to have a reasonably small value, the subtraction does not take place in much of the phase space, and chances of mis-binning can be greatly reduced.

In order to take into account the dipole contributions that are not subtracted due to α, the $\boldsymbol{I}$, $\boldsymbol{K}$, and $\boldsymbol{P}$ operators are modified accordingly, whose contribution were originally designed to compensate the dipole contribution subtracted in the entire phase space. The $\boldsymbol{I}$ contribution (Eq. (4.29)) becomes

$$\begin{aligned}
&\left[\boldsymbol{I}(\alpha) \textbf{ contribution for } q\bar{q}\right] \\
=&\int \frac{1}{2\hat{s}} \mathrm{d}x_1 \mathrm{d}x_2 \mathrm{PDF}_a(x_1;\mu^2_{\mathrm{Fac}})\mathrm{PDF}_b(x_2;\mu^2_{\mathrm{Fac}}) \\
&\times \int \Theta(x_1x_2s - \hat{s})\mathrm{dPS}_{VH}|\mathscr{M}^{\mathrm{LO}}_{ab}|^2 \frac{\alpha_S}{2\pi} C_F \left[\frac{(4\pi)^\epsilon}{\Gamma(1-\epsilon)}\right]
\end{aligned}$$

$$\times\left[\left(10-\pi^2+3\ln\frac{\mu_{\rm Fac}^2}{s_{ab}}+\ln^2\frac{\mu_{\rm Fac}^2}{s_{ab}}\right)+\frac{1}{{\epsilon_{\rm IR}}^2}+\frac{1}{\epsilon_{\rm IR}}\left(\ln\frac{\mu_{\rm Fac}^2}{s_{ab}}+\frac{3}{2}\right)-1\right.$$
$$\left.-\left(2\ln^2\alpha-3\big(\alpha-1-\ln\alpha\big)\right)\right] \tag{4.48}$$

Notice that the α-dependence is only with the finite part of the $\boldsymbol{I}$ contribution.

The $\boldsymbol{K}$ contribution to the $q\bar{q}$-initiated processes (Eq. (4.31)) becomes

$$\big[\boldsymbol{K}(\alpha)\ \textbf{contribution for}\ q\bar{q}\big]$$
$$=\sum_{a'}\int {\rm d}x_1{\rm d}x_2\int_0^1{\rm d}x\frac{1}{2\hat{s}}{\rm PDF}_a(x_1;\mu_{\rm Fac}^2){\rm PDF}_b(x_2;\mu_{\rm Fac}^2)$$
$$\times\int\Theta(xx_1x_2s-\hat{s}){\rm dPS}_{VH}|\mathscr{M}_{a'b}^{\rm LO}(xp_a,p_b)|^2\frac{\alpha_{\rm S}}{2\pi}C_F$$
$$\times\left\{\Theta(x+\alpha-1)\left[\frac{2}{1-x}\ln\frac{(1-x)^2}{x}\right]_+ +\Theta(1-\alpha-x)\left[\frac{2}{1-x}\ln\frac{1-x}{x}\right]_+\right.$$
$$+\left[-(1+x)\ln\frac{(1-x)^2}{x}+(1-x)+\frac{1+x^2}{1-x}\ln\left(\min\left(1,\frac{\alpha}{1-x}\right)\right)\right]$$
$$+\left[\frac{2}{1-x}\ln(1-x)\Theta(1-\alpha-x)\right]$$
$$\left.+\delta(1-x)\left[\frac{2\pi^2}{3}-5+\left(2\ln^2\alpha-\frac{3}{2}\big(\alpha-1-\ln\alpha\big)\right)\right]\right\}$$
$$+\big[(a,1)\longleftrightarrow(b,2)\big]. \tag{4.49}$$

The $\boldsymbol{K}$ contribution to the gq-initiated processes (Eq. (4.41)) becomes

$$\big[\boldsymbol{K}(\alpha)\ \textbf{contribution for}\ gq\big]=\sum_{a,b\in\{q,\bar{q}'\}}\left\{\right.$$

$$
\begin{aligned}
&= \int \mathrm{d}x_1 \mathrm{d}x_2 \int_0^1 \mathrm{d}x \int \Theta(x x_1 x_2 s - \hat{s}) \mathrm{dPS}_{VH} \frac{1}{2\hat{s}} \mathrm{PDF}_a(x_1; \mu^2_{\mathrm{Fac}}) \mathrm{PDF}_{\bar{b}}(x_2; \mu^2_{\mathrm{Fac}}) \\
&\quad \times |\mathscr{M}^{\mathrm{LO}}_{a\bar{b}}(p_a, x p_g)|^2 \frac{\alpha_{\mathrm{S}}}{2\pi} T_R \left[\left(x^2 + (1-x)^2\right) \ln \frac{(1-x)^2 \ \min\left(1, \frac{\alpha}{1-x}\right)}{x} \right. \\
&\quad \left. + 2x(1-x) \right] \\
&+ \int \mathrm{d}x_1 \mathrm{d}x_2 \int_0^1 \mathrm{d}x \int \Theta(x x_1 x_2 s - \hat{s}) \mathrm{dPS}_{VH} \frac{1}{2\hat{s}} \mathrm{PDF}_{\bar{b}}(x_1; \mu^2_{\mathrm{Fac}}) \mathrm{PDF}_a(x_2; \mu^2_{\mathrm{Fac}}) \\
&\quad \times |\mathscr{M}^{\mathrm{LO}}_{\bar{b}a}(x p_g, p_a)|^2 \frac{\alpha_{\mathrm{S}}}{2\pi} T_R \left[\left(x^2 + (1-x)^2\right) \ln \frac{(1-x)^2 \ \min\left(1, \frac{\alpha}{1-x}\right)}{x} \right. \\
&\quad \left. + 2x(1-x) \right] \Bigg\}.
\end{aligned}
$$

The $\boldsymbol{P}$ contributions to both the $q\bar{q}$- and gq-initiated processes are not modified by the introduction of the α parameter. While the α parameter controls the size of the phase space that contains the infrared singularities, and a reasonably small value of α can be used to reduce the chances of mis-binning, both the NLO correction to the $q\bar{q}$-initiated processes and the gq-initiated processes should be separately α-*in*dependent in their cross sections and in their kinematic distributions. Therefore checking α-independence by running the simulation with a few different α values can be used to check if mistakes exist in the calculation.

4.3.2 Mis-binning due to Plus Distributions

From Eqs. (4.33) and (4.36), one can also expect that cancellation between large numbers in a numerical simulation is possible as x approaches 1. Therefore mis-binning can occur when related momentum sets happen to end up in different bins of a histogram. The effect of mis-binning here can be eliminated by performing changes of variable in Eqs. (4.33) and (4.36),

$$xx_1 \to x_1, \quad x_1 \to \frac{x_1}{x}; \quad \text{and} \quad xx_2 \to x_2, \quad x_2 \to \frac{x_2}{x}, \tag{4.50}$$

which substitutes multiple sets of momenta with multiple sets of PDF's. This technique is introduced in Ref. [75]. It is not employed in the current version of JHUGEN, but has been implemented in another version of the generator independently by Dr. Markus C. Schulze, a collaborator of JHUGEN. The two independent implementations of $\boldsymbol{I}$, $\boldsymbol{K}$, $\boldsymbol{P}$ were used to crosscheck the results from one another.

4.4 Collider Phenomenology

In Fig. 4.3, the theoretical uncertainties of the $q\bar{q} \to Z^* \to ZH \to \ell^-\ell^+ b\bar{b}$ simulation at next-to-leading order are presented. The theoretical uncertainty mainly consists of that from different PDF sets, and that from the varying energy scale of the calculation. The PDF sets used in this evaluation are CT14NNLO [51], MSTW2008LO90CL [52], and NNPDF31_LO_AS_0118 [53]. The energy scales relevant to this simulation are the renormalization scale μ^2_{Ren} and the factorization scale μ^2_{Fac} used by the PDF. Both have been set

to $\mu_{\text{Ren}} = \mu_{\text{Fac}} = m_{ZH}$. To evaluate the uncertainty due to this scale, the simulation is repeated with $\mu_{\text{Ren}} = \mu_{\text{Fac}} = 2m_{ZH}$ and $\mu_{\text{Ren}} = \mu_{\text{Fac}} = m_{ZH}/2$.

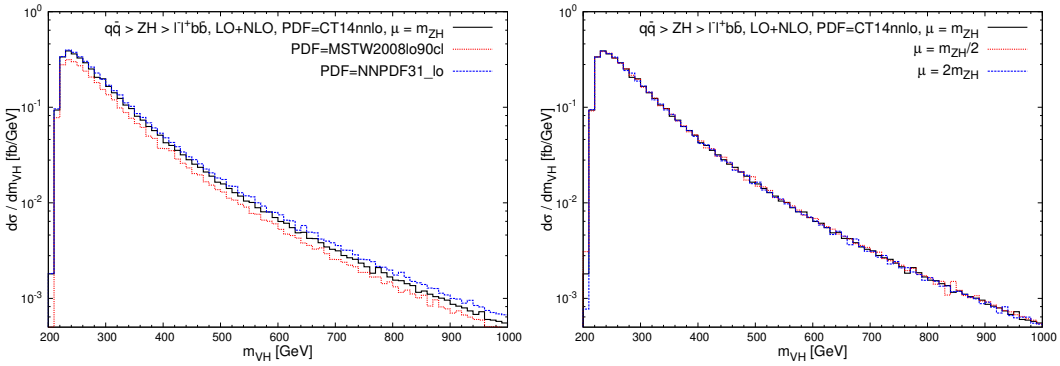

Figure 4.3: m_{ZH} distribution for simulated $q\bar{q} \to Z^* \to ZH \to \ell^-\ell^+ b\bar{b}$ SM events at 14 TeV at NLO, created with three PDF sets (left) as well as using three factorization scales (right).

The cross section varies by approximately 12% with the selected PDF sets, and 0.1% with the scales. The scale dependence of the cross section has been reduced significantly from that of the LO calculation, which is an expected feature of the NLO calculation.

In Fig. 4.4, the independence of the $q\bar{q} \to Z^* \to ZH \to \ell^-\ell^+ b\bar{b}$ simulation at next-to-leading order due to the choice of the α parameter (See Section 4.3.1 for details) is presented. In the rest of this chapter,

$$\alpha = 0.1 \tag{4.51}$$

is selected if not specified otherwise, and Eq. (3.50) is adopted as the definition of $\cos\theta_1$.

In Figs. 4.5, 4.6, and 4.7, the ratios of differential cross sections between NLO and LO (K factors) are presented for the theoretical scenarios of SM, g_2,

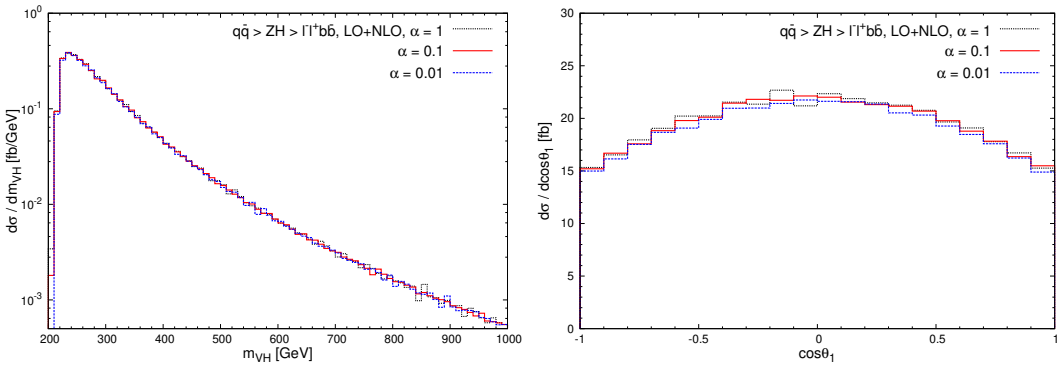

Figure 4.4: Demonstration of α-independence in simulated $q\bar{q} \to Z^* \to ZH \to \ell^-\ell^+ b\bar{b}$ SM events at 14 TeV at NLO. The definition of $\cos\theta_1$ is in Eq. (3.50).

and pseudoscalar. Notice that the angles defined in Fig. 1.2 are leading order in nature and do not account for the radiated parton. The $\cos\theta_1$, for example, needs clarification when it is assigned to an NLO event. When computing the angles in this Chapter, except for the radiated parton due to NLO real correction, a boost is first performed on every final-state particle of the event such that the boosted $Z^* \to ZH \to \ell^-\ell^+ b\bar{b}$ system no longer has transverse momentum. Then the boosted $Z^* \to ZH \to \ell^-\ell^+ b\bar{b}$ momenta are used to compute the angles in the same manner as for the LO events. While this treatment is not unique, it allows a smooth transition between LO and NLO kinematics, as well as a reasonable estimate of the momentum fractions $x_{1,2}$ of the scattering partons.

In Figs. 4.5, 4.6, and 4.7, the K factors remain relatively constant against most of the kinematic variables in three theoretical scenarios with anomalous couplings. The exception is p_{T}^H, where higher p_{T}^H receives slightly larger K factor. The overall K factors are 1.12, 1.14, and 1.14 for the theoretical scenarios of SM, g_2, and pseudoscalar, respectively.

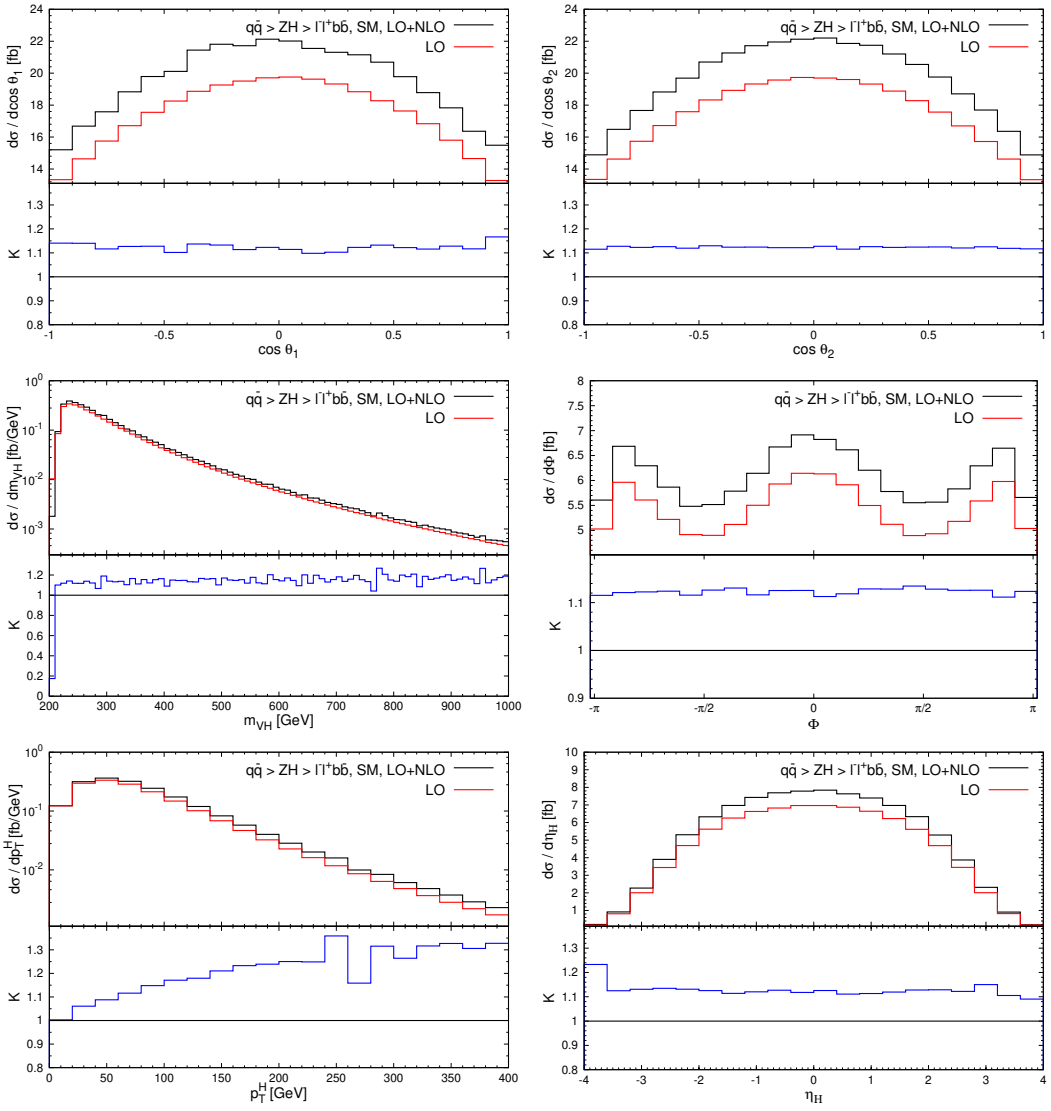

Figure 4.5: Selected kinematic distributions for simulated $q\bar{q} \to Z^* \to ZH \to \ell^-\ell^+ b\bar{b}$ SM events at 14 TeV at NLO and LO, as well as the differential K factors. The overall K factors is 1.12.

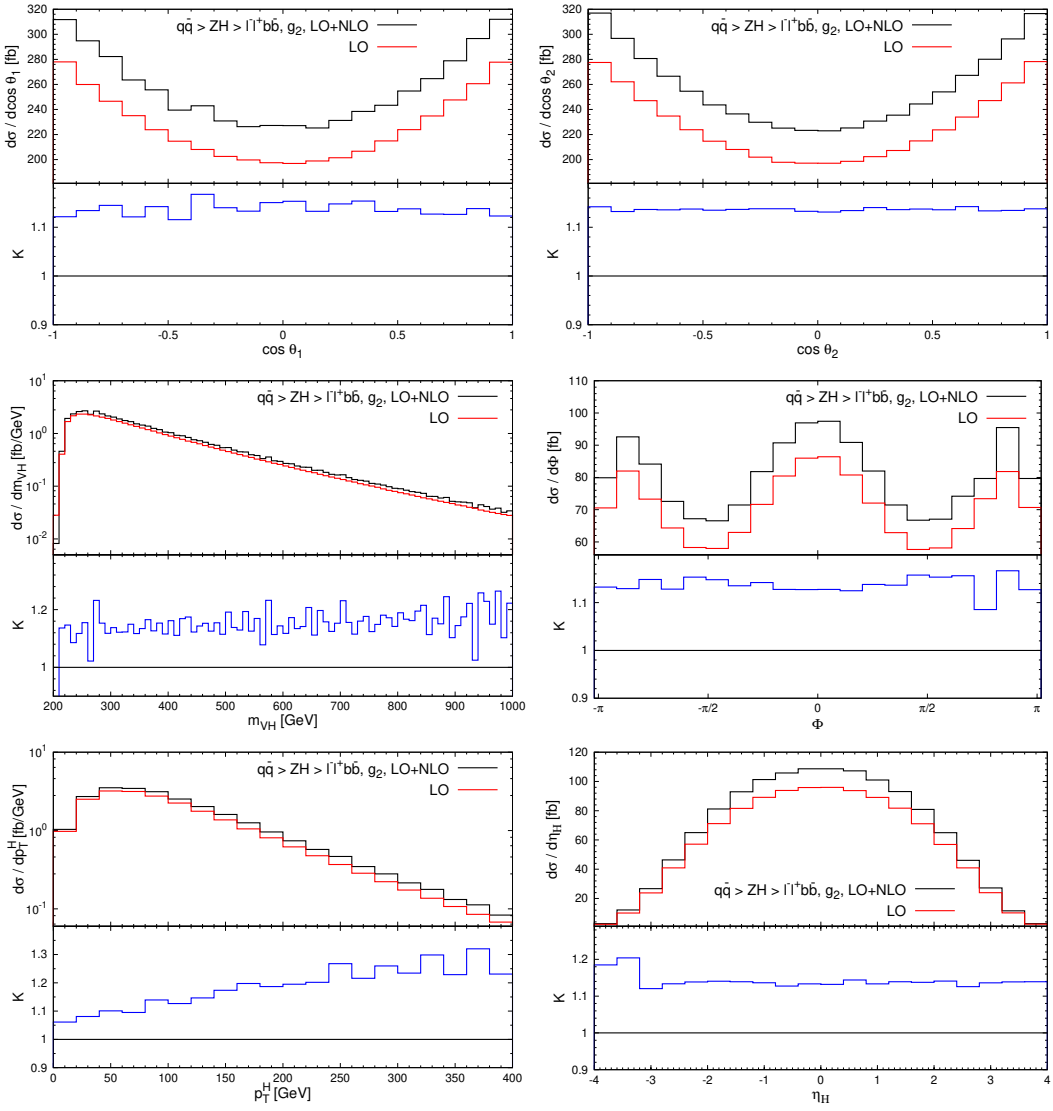

Figure 4.6: Selected kinematic distributions for simulated $q\bar{q} \to Z^* \to ZH \to \ell^-\ell^+ b\bar{b}$ g_2 events at 14 TeV at NLO and LO, as well as the differential K factors. The overall K factors is 1.14.

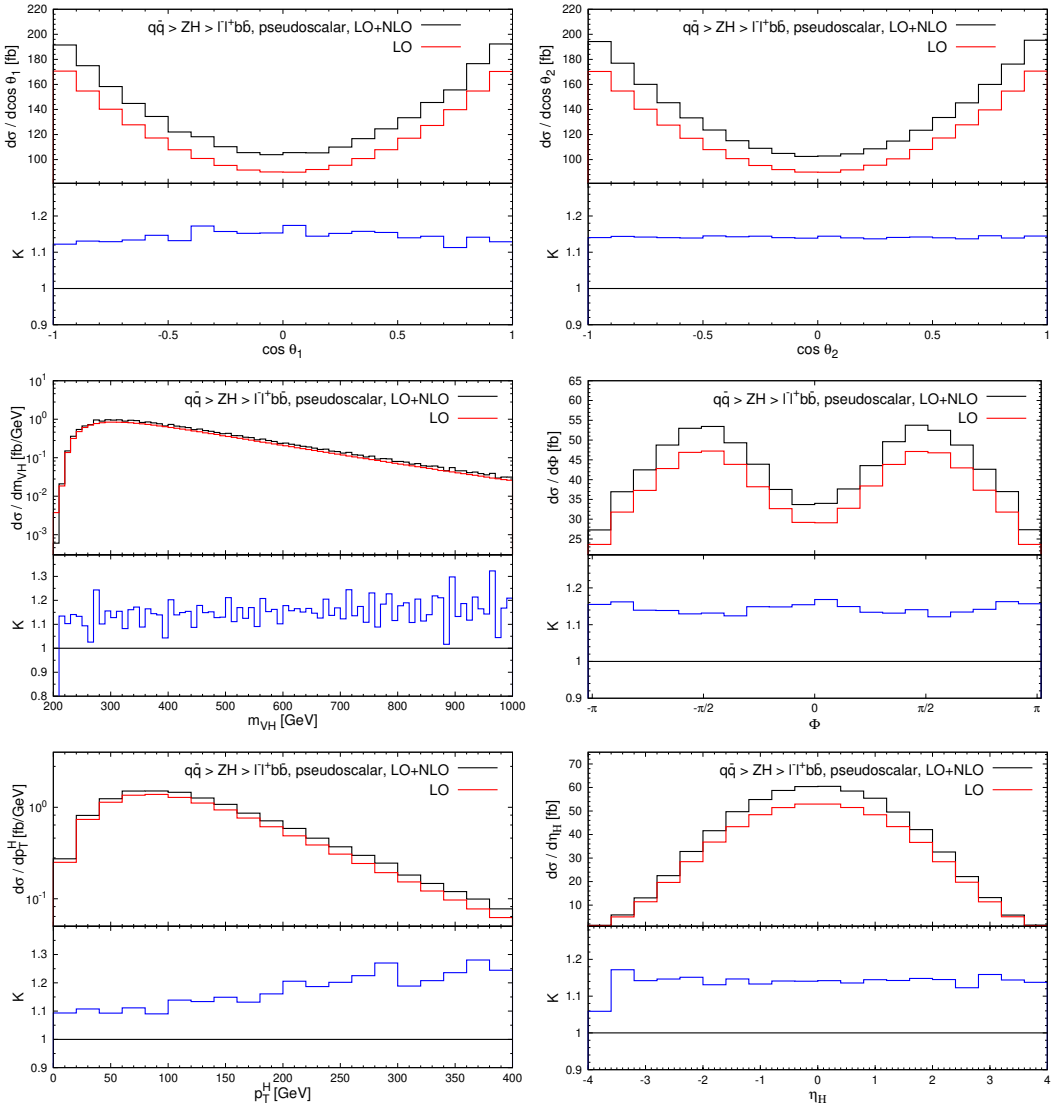

Figure 4.7: Selected kinematic distributions for simulated $q\bar{q} \to ZH \to \ell^-\ell^+ b\bar{b}$ pseudoscalar events at 14 TeV at NLO and LO, as well as the differential K factors. The overall K factors is 1.14.

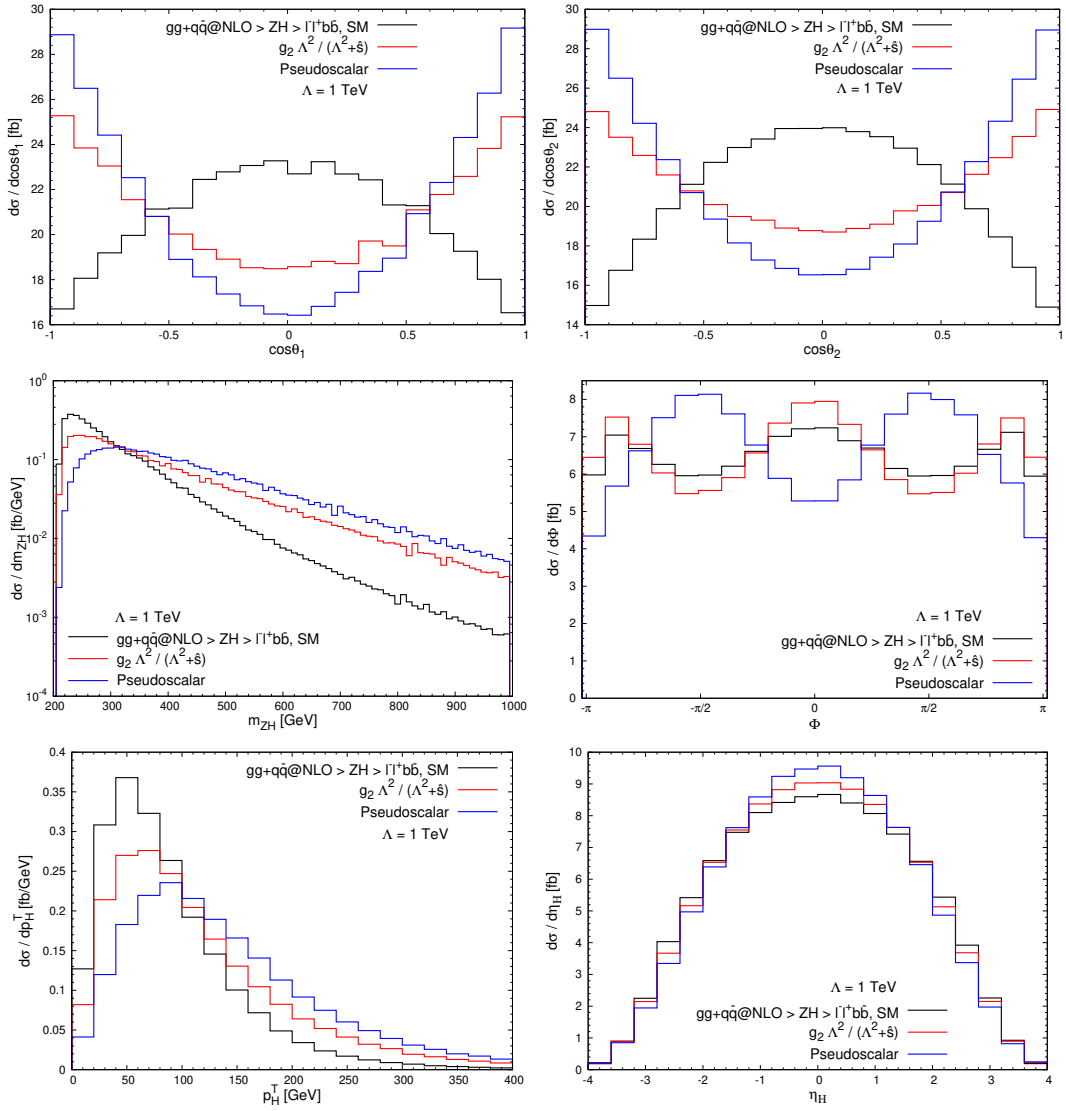

Figure 4.8: selected kinematic distributions are presented with simulated $pp(gg + q\bar{q})$@NLO $\rightarrow ZH \rightarrow \ell^-\ell^+b\bar{b}$ events at 14 TeV assuming the theoretical scenarios of SM, g_2, and pseudoscalar.

In Fig. 4.8, selected kinematic distributions are presented with simulated $pp(gg + q\bar{q})$@NLO $\rightarrow Z^* \rightarrow ZH \rightarrow \ell^-\ell^+ b\bar{b}$ events assuming the theoretical scenarios of SM, g_2, and pseudoscalar.

Chapter 5

Constraining the Higgs Boson Coupling to Light Quarks in the $H \to ZZ$ Final States

This study was first published in Ref. [39] in January 2016. Minor modifications were made. Since the discovery of a Higgs boson with a mass of around 125 GeV at the Large Hadron Collider (LHC) [1, 2], measurements of its properties have shown consistency with the Standard Model (SM) expectations within the uncertainties [76, 77, 78]. Assuming SM, the gluon fusion via closed quark loop dominates the Higgs boson production, because of large gluon-gluon luminosity and large mass of the top quark. Also due to relatively large mass of the b quark, the Higgs boson decays into a pair of b quarks most of the time. While experimental analyses have been performed on the interactions between the Higgs boson and heavy quarks [79, 80, 81, 82, 83, 84, 85, 86], as well as leptons [87, 88, 89, 90, 86], at the time of this study, no experimental results have been presented on the Higgs Yukawa coupling to the quarks, namely, u, d, and s quarks. This is not surprising, because in SM, (1) the small

masses of the u and d quarks make their Yukawa couplings to the Higgs boson weak, with the branching fraction ($\mathscr{Br}$) of the Higgs boson decaying to u or d quark pair being $\lesssim 10^{-6}$; and (2) while $\mathscr{Br}(H \to s\bar{s}) \sim 2.4 \times 10^{-4}$ (comparable to $\mathscr{Br}(H \to \mu^+\mu^-)$) and $\mathscr{Br}(H \to c\bar{c}) \sim 2.9 \times 10^{-2}$ (comparable to $\mathscr{Br}(H \to ZZ)$), these decaying processes are difficult to observe without efficient quark flavor tagging. It is worth noting that in Ref. [89], the upper limits of $\mathscr{Br}(H \to \mu^+\mu^-)$ and $\mathscr{Br}(H \to e^+e^-)$ have been set to be 0.0016 and 0.0019 respectively, where the latter is $\approx 3.7 \times 10^5$ times the SM value. It is also worth noting that phenomenological studies do exist on constraining light Yukawa couplings of light quarks. For example, in Ref. [91], depending on the analysis performed, the upper limit of the Yukawa coupling between the Higgs boson and the c quark can be set as low as $\lesssim 6.2$ times the SM value. Another example is Ref. [92], in which Higgs-boson-mediated production of vector meson in association with a vector boson is used to constrain Yukawa couplings of u, d, and s quarks. Via a global fit and depending on how the couplings are allowed to vary, the upper limit of these couplings are found to be close to the SM Yukawa coupling of the b quark, whose numerical indications will be summarized in a later table.

In this study I attempt to constrain the Yukawa coupling between the Higgs boson and quarks in the first two generations. The Yukawa Lagrangian after electroweak symmetric breaking is

$$\mathscr{L}_{\text{Yukawa}} = -\sum_f \frac{m_f}{v} \bar{f} f H, \tag{5.1}$$

where the summation is over fermion flavors. Relaxing the coupling constants,

the deviation from SM considered in this study is written as

$$\Delta\mathscr{L}_{\text{Yukawa}} = -\sum_{f}(\kappa_f - 1)\frac{m_f}{v}\bar{f}fH, \tag{5.2}$$

where $f = u, d, s, c$, and the scaling factors κ_f are real and can take both positive and negative values. The masses of the quarks are set according to the 2014 Particle Data Group summary table [93]. As the couplings of the Higgs boson to other particles is kept SM, the deviation of κ_f from 1 leads to change in the Higgs boson width, and in the cross sections of processes involving Yukawa interactions.

Combining the direct measurement with $\gamma\gamma$ and 4ℓ final states, the CMS experiment has set an upper limit on the Higgs boson width at 1.7 GeV at a 95% confidence level (CL) [78]. This can be translated to an upper limit on each $|\kappa_f|$ by adding its contribution to the Higgs boson width predicted by SM. In Table 5.1, I list the upper limits on $|\kappa_f|$ due to this argument, the calculation is performed at leading order (LO), with the Higgs boson mass $m_H = 125.6$ GeV and the corresponding SM width $\Gamma_H^{\text{SM}} = 4.15$ MeV. As a reference, the upper limits set by requiring the theory being perturbative, namely,

$$\kappa_f \frac{m_f}{v} < \mathcal{O}(1) \tag{5.3}$$

are listed in Table 5.1. In addition, the upper limits by Ref. [91] and Ref. [92] are also listed, as some of the best constraints placed till January 2016.

In the remainder of this study I explore constraints on κ_f from the production of the Higgs boson, which decays into a pair of Z bosons. In SM, the production of the Higgs boson is dominated by gluon fusion with t and b

	$\lvert\kappa_u\rvert$	$\lvert\kappa_d\rvert$	$\lvert\kappa_s\rvert$	$\lvert\kappa_c\rvert$
Perturbation	$< 1.1 \times 10^5$	$< 5.1 \times 10^4$	< 2600	< 190
$\Gamma_H < 1.7$ GeV	$\lesssim 4.9 \times 10^4$	$\lesssim 2.4 \times 10^4$	$\lesssim 1200$	$\lesssim 88$
Ref. [91]				$\lesssim 6.2$
Ref. [92]	$2100 - 2800$	$930 - 1400$	$35 - 70$	

Table 5.1: 95% CL upper limits of scaling factors $|\kappa_f|$, due to Higgs boson width direct measurement; in comparison with those by requiring the theory perturbative, and those by Ref. [91] and Ref. [92]. In the Standard Model, $\kappa_f = 1$.

loops (Fig. 5.1(a)). The dominant continuum background is the quark-initiated ZZ production (Fig. 5.1(b)), accompanied by gluon-initiated ZZ production (Fig. 5.1(c)). The subdominant production mechanism of the Higgs boson is vector boson fusion (VBF, Fig. 5.1(d)), which contributes about 7% to the Higgs boson production in the resonance region, and about 10% in the $m_{ZZ} > 2m_Z$ region.

As the Yukawa couplings change with κ_f, additional contributions from the Higgs-mediated quark annihilation (Fig. 5.2(a, b)) and gluon fusion with light quark loops (Fig. 5.2(c)) are taken into account in this study. While it is understood that a large $|\kappa_f|$ could make a difference in the VBF type diagram, by having Higgs boson in place of the weak bosons (Fig. 5.2(d)), its contribution is neglected in this study because of its distinct kinematic characteristics, particularly the angular correlation between the two jets, which will allow suppression (see, e.g. Ref. [35]).

For a typical process with the Higgs boson created in the s-channel, the

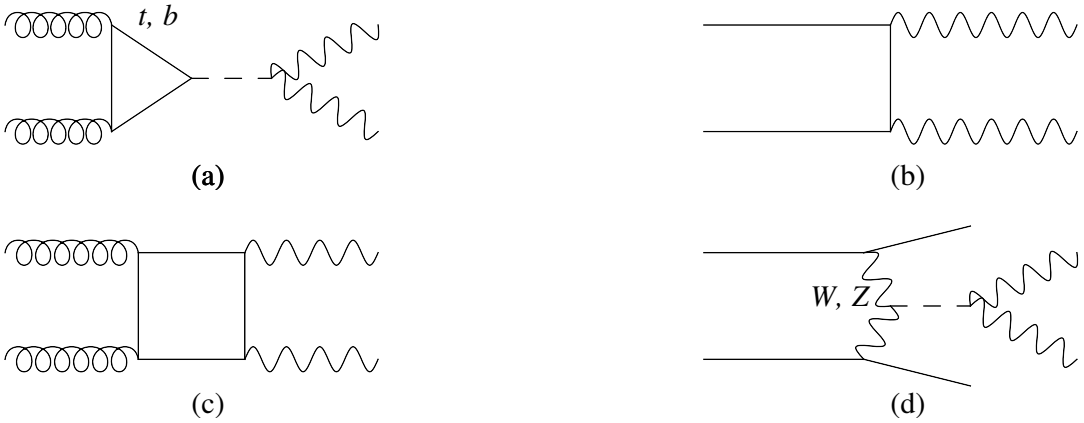

Figure 5.1: LO contributions to the main ZZ production processes: (a) Higgs-mediated gg production; (b) quark-initiated background production; (c) gluon-initiated background production; and (d) Higgs-mediated VBF production.

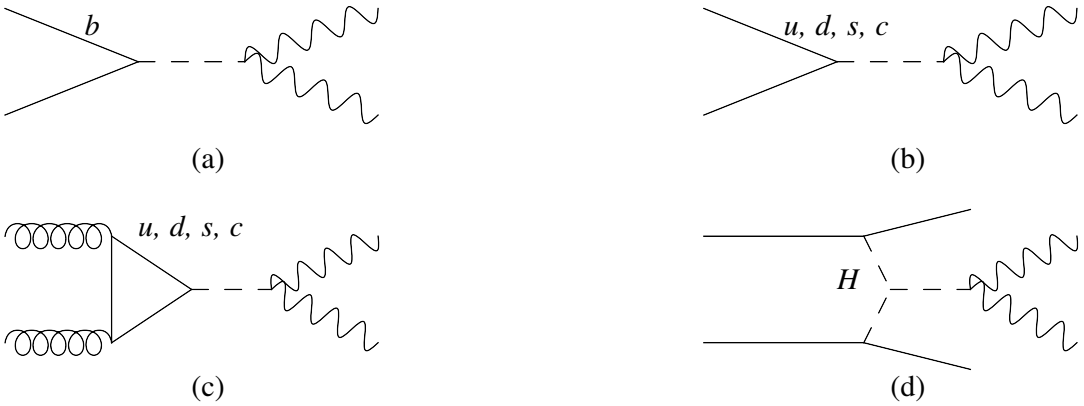

Figure 5.2: Additional LO contributions to the ZZ production due to b and light quarks: (a) Higgs-mediated $b\bar{b}$ annihilation; (b) Higgs-mediated light-quark annihilation; (c) Higgs-mediated gg production; and (d) $H \to ZZ$ production via Higgs boson fusion.

cross section in the resonance and off-shell region behaves as

$$\sigma^{\text{resonance}}_{A\to H\to B} \sim \frac{g^2_{AH}\, g^2_{HB}}{\Gamma_H} \text{ and } \sigma^{\text{off-shell}}_{A\to H^*\to B} \sim g^2_{AH}\, g^2_{HB}, \tag{5.4}$$

respectively, where g_{AH} (g_{HB}) is the Higgs boson coupling to the initial (final) state. The resonance and off-shell regions offer two distinct sources of information on the Yukawa couplings. In the resonance region, the gluon fusion is always the dominant mechanism of Higgs boson production, even at large scaling factors $|\kappa_f|$, as a result of the large gluon-gluon luminosity. While each scaled-up Yukawa coupling makes its increased contribution in the $gg \to H$ closed quark loop, its increased contribution to the Higgs boson width affects the production overwhelmingly at large $|\kappa_f|$, reducing the cross section to near zero. This feature can be used to constrain κ_f by requiring $|\kappa_f|$ being small enough to allow consistency with experimental observations. In the off-shell region, the production cross section of the Higgs boson, which decays into ZZ, receives enhancement at $m_{ZZ} \gtrsim 2m_Z$, where the invariant mass of the Higgs boson allows both Z bosons become on-shell [94, 95]. In addition, the parton luminosities of $q\bar{q}$, particularly $u\bar{u}$ and $d\bar{d}$, are less dominated by that of gg (see, e.g. Ref. [35]). As a result, the production of the Higgs boson becomes dominated by the $q\bar{q}$ annihilation (Fig. 5.2(b)) at large $|\kappa_f|$, and the cross section increases with $|\kappa_f|^2$. Therefore the measured off-shell cross section may be used to further constrain κ_f.

The cross section of ZZ production with four-lepton (4ℓ, $\ell = e, \mu$) final states in proton-proton collisions at centre-of-mass energy $\sqrt{s} = 7\,\text{TeV}$ and 8 TeV is then calculated, as a function of each individual κ_f, and compare to

the signal strength μ_{ggH} reported by CMS in Ref. [78, 96], which is based on integrated luminosities of 5.1 fb^{-1} at $\sqrt{s} = 7$ TeV and 19.7 fb^{-1} at 8 TeV. The signal strength is defined by the relation,

$$\sigma^{\text{obs.}}_{gg\to ZZ} = \mu_{ggH}\,\sigma^{\text{SM}}_{\text{signal}} + \sqrt{\mu_{ggH}}\,\sigma^{\text{SM}}_{\text{intf.}} + \sigma^{\text{SM}}_{\text{bkg.}}, \tag{5.5}$$

where $\sigma^{\text{obs.}}_{gg\to ZZ}$, $\sigma^{\text{SM}}_{\text{signal}}$, $\sigma^{\text{SM}}_{\text{intf.}}$, and $\sigma^{\text{SM}}_{\text{bkg.}}$ are the total gluon-initiated ZZ cross section observed, SM predictions for the Higgs boson signal, signal-background interference, and background, respectively. While our analysis largely involves Higgs boson production by $q\bar{q}$ annihilation, its indistinguishability from gluon fusion allows us to base the analysis on μ_{ggH}. In each calculation, one κ_f is varied in the range set by Table 5.1 while others are kept at 1 (SM value). The resonance region is defined as $120.5\,\text{GeV} < m_{4\ell} < 130.6\,\text{GeV}$ in our calculation, which does not necessarily agree with the CMS definition. The off-shell region is defined as $220\ \text{GeV} < m_{4\ell} < 800\,\text{GeV}$, as adopted by CMS in Ref. [96].

The gluon-initiated processes are calculated as follows. The contribution from diagrams in Figs. 5.1(a), 5.2(c), and their interference with the diagram in Fig. 5.1(c) is calculated using MCFM 6.8 [97] with NPROC $= 128 - 130$ at loop-induced leading order in perturbative quantum chromodynamics (QCD). The contribution from the diagram in Fig. 5.2(c) is implemented by adding codes that are parallel to those that calculate the t and b loops. The contribution from the diagram in Fig. 5.1 (c) is calculated with NPROC $= 81$ at loop-induced leading order. For simplicity, the quark mass evolution is accounted as part of the uncertainty in the cross section. The cross sections of

the gluon-initiated processes are scaled by the same m_{ZZ}-dependent correction factors to the LO cross section (K factors) applied in Ref. [96], with next-to-next-to-leading order and next-to-next-to-leading logarithms accuracy for the total cross section [98, 99, 100]. The QCD renormalization and factorization scales are set to $\mu_r = \mu_f = m_{ZZ}/2$ (dynamic scales) and MSTW2008 parton distribution functions (PDFs) [101] are used.

The quark-initiated processes are calculated using MADGRAPH5 V2.2.3 [102] at LO, with a modified SM model that includes the Yukawa couplings for all the quark species. Interferences between Fig. 5.1(b) and Fig. 5.2(a, b) are given full treatment. The cross sections calculated at LO are scaled by a K factor, which is the ratio between the NLO cross section of Fig. 5.1(b) obtained by MCFM and the LO one by MADGRAPH5. The cross section is further scaled by a K factor due to NLO electroweak corrections [103, 104], which predicts negative and m_{ZZ}-dependent corrections to the $q\bar{q} \to ZZ$ process for on-shell Z boson pairs. $\mu_r = \mu_f = m_{ZZ}/2$ and MSTW2008 PDFs are used.

I employ the CMS selection requirements [105], requiring $p_{\perp,\mu} > 5$ GeV, $p_{\perp,e} > 7$ GeV, $|\eta_\mu| < 2.4$, $|\eta_e| < 2.5$, $m_{\ell^+\ell^-} > 4$ GeV, $M_{4l} > 100$ GeV. In addition, the transverse momentum of the hardest (next-to-hardest) lepton should be larger than 20 (10) GeV, the invariant mass of a pair of same-flavor leptons closest to the Z boson mass should be in the interval 40 GeV $< m_{\ell^+\ell^-} <$ 120 GeV and the invariant mass of the other pair should be in the interval 12 GeV $< m_{\ell^+\ell^-} <$ 120 GeV.

In the resonance region, the cross section of $q\bar{q}$ annihilation is dependent on κ_f, but its contribution to the total cross section is tiny due to small Yukawa

couplings. For example, even at $\kappa_u = 5 \times 10^4$, this cross section is only at a few percent level of that of the SM gluon fusion. The strongest dependence on κ_f is with the gluon fusion process, Fig. 5.1(a) and Fig. 5.2(c), combined with its interference with the continuum background. This cross section decreases as $|\kappa_u|$ increases, because of its $1/\Gamma_H$ dependence, as suggested in Eq. (5.4). At sufficiently large $|\kappa_u|$, the signal is washed out, and the gluon-initiated processes reduce to the continuum background production of ZZ.

In Fig. 5.3, the results in the resonance region are combined, and the expected signal strength, translated from cross section by Eq. (5.5), as function of each individual κ_f, is presented and compare to the signal strength for gluon fusion $\mu_{ggH} = 0.85^{+0.19}_{-0.16}$, reported by the CMS experiment [78]. In Table 5.2, the 95% CL limits for each κ_f is summarized. There is a slight asymmetry about $\kappa_f = 0$ due to the sign of the interference in the gluon-initiated processes.

In the off-shell region, the Standard Model expects the sum of Higgs boson signal and its interference with the continuum background to be slightly negative. While this sum is dependent on $|\kappa_f|$, the total cross section becomes dominated by the quark-initiated process at large $|\kappa_f|$. Although the sensitivity of the off-shell cross section is not as high as that of the gluon-initiated process in the resonance region for relatively small $|\kappa_f|$, sufficiently large $|\kappa_f|$ give rise to a departure from the number of events observed by CMS.

In Fig. 5.4, the expected off-shell signal strength as functions of κ_f are compared with the one estimated from the result published by CMS in Ref. [96, 106]. The subtracted number of background events, instead of signal strength, are presented in Fig. 5.4. The number of events are translated from signal

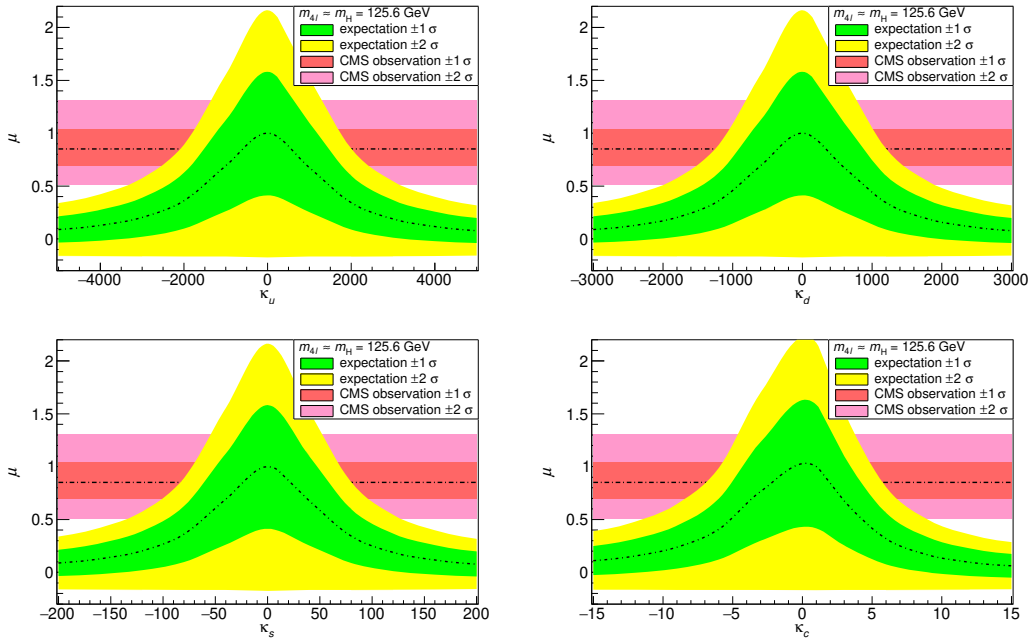

Figure 5.3: Number of $ZZ \to 4\ell$ events expected in the resonance region ($105.6\ \text{GeV} < m_{4\ell} < 140.6\ \text{GeV}$) as functions of κ_f (1σ and 2σ uncertainties in green and yellow bands), in comparison with number of events observed by CMS (1σ and 2σ uncertainties in red and pink bands), with 5.1 fb^{-1} proton-proton collisions at $\sqrt{s} = 7\,\text{TeV}$ and 19.7 fb^{-1} at 8 TeV. See text for details of calculation.

$$
\begin{aligned}
-3300 &\lesssim \kappa_u \lesssim 3200\,, \\
-2000 &\lesssim \kappa_d \lesssim 1900\,, \\
-130 &\lesssim \kappa_s \lesssim 125\,, \\
-11 &\lesssim \kappa_c \lesssim 9\,.
\end{aligned}
$$

Table 5.2: 95% CL limits of scaling factors κ_f, by the observation of production of the Higgs boson in the resonance and its decay to the ZZ final states.

strength by Eq. (5.5). Moreover, since the observation of the Higgs boson signal in the resonance is a well established fact, the analysis respects this fact by scaling the off-shell signal strength in such a way that the resonance signal strength is fixed. In other word, from the analysis in the resonance region, it is learned that signal strength decreases with increasing $|\kappa_f|$, and therefore in the off-shell analysis, the signal strength is scaled accordingly so that for any $|\kappa_f|$ the resonance signal strength remains 0.85. In Table 5.3, the 95% CL limits on each κ_f set by the analysis in the off-shell region are summarized. Again, an additional 50% uncertainty is assigned to each limit for ignoring the quark mass evolution.

From the analysis in the off-shell region, upper limits for $|\kappa_u|$ and $|\kappa_d|$ that are over twice tighter than those due to the Higgs boson width direct measurement are obtained, and slightly tighter results for $|\kappa_s|$ and $|\kappa_c|$. The better performance of this analysis on $|\kappa_u|$ and $|\kappa_d|$ is due to the higher parton luminosities of $u\bar{u}$ and $d\bar{d}$ than those of $s\bar{s}$ and $c\bar{c}$. Furthermore, at a fixed energy of proton-proton collision, although parton luminosities decrease in general as the center-of-mass energy of the colliding partons increases, the rates of decreasing are slower for $u\bar{u}$ and $d\bar{d}$ luminosities than those for $s\bar{s}$ and $c\bar{c}$, which are still slower than that of gg (see, e.g. Ref. [35]). This suggests an improvement of this analysis as the higher invariant mass region is explored. As an illustration, I perform the analysis with $m_{4\ell} > 1200$ GeV at High-Luminosity LHC (HL-LHC), where an integrated luminosity of $3000\,\text{fb}^{-1}$ is delivered at $\sqrt{s} = 14\,\text{TeV}$. As shown in Fig. 5.5, a factor of ~ 3 improvement over the current limits can be expected for $|\kappa_u|$ and $|\kappa_d|$, as well as a factor of

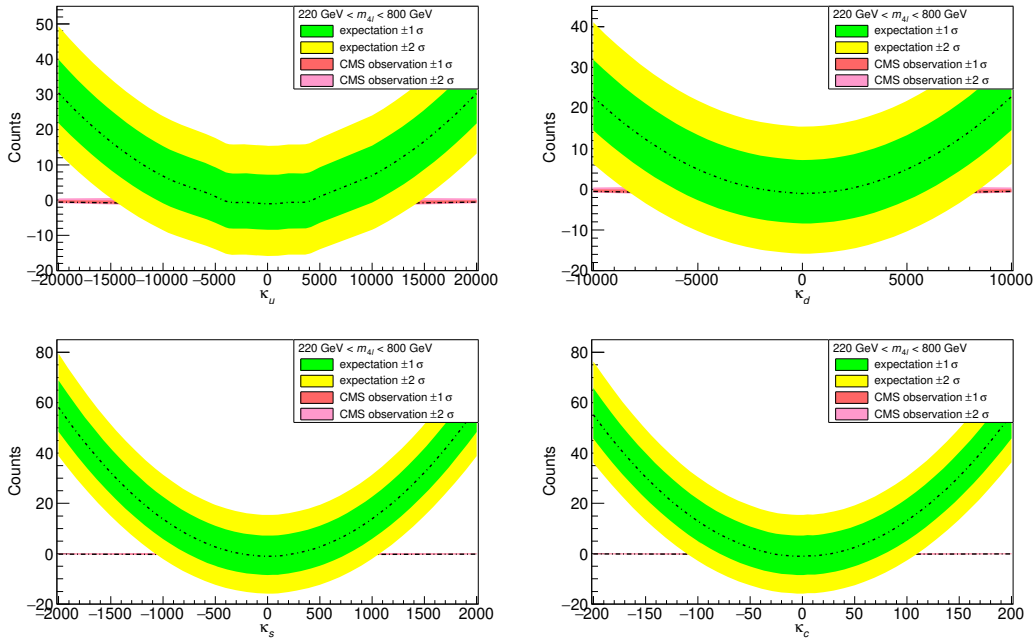

Figure 5.4: Number of $ZZ \to 4\ell$ events due to Higgs boson (signal and interference) expected in the off-shell ($220\ \text{GeV} < m_{4\ell} < 800\ \text{GeV}$) region as functions of κ_f (1σ and 2σ uncertainties in green and yellow bands), in comparison with number of events observed by CMS (1σ and 2σ uncertainties in red and pink bands), with $5.1\,\text{fb}^{-1}$ proton-proton collisions at $\sqrt{s} = 7\,\text{TeV}$ and $19.7\,\text{fb}^{-1}$ at 8 TeV. See text for details.

$$
\begin{aligned}
|\kappa_u| &\lesssim 1.5 \times 10^4\,, \\
|\kappa_d| &\lesssim 8600\,, \\
|\kappa_s| &\lesssim 1100\,, \\
|\kappa_c| &\lesssim 110\,.
\end{aligned}
$$

Table 5.3: 95% CL upper limits of scaling factors $|\kappa_f|$, by the observation of off-shell production of the Higgs boson and its decay to the ZZ final states.

~ 2 for $|\kappa_s|$ and $|\kappa_c|$.

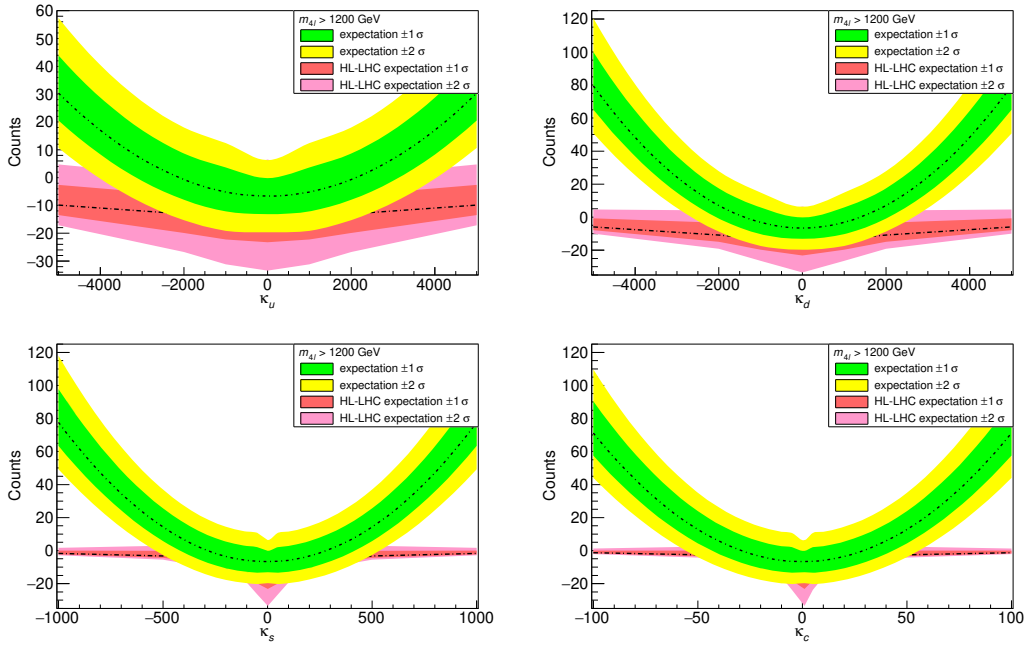

Figure 5.5: Number of $ZZ \to 4\ell$ events due to Higgs boson (signal and interference) expected in the off-shell ($m_{4\ell} > 1200$ GeV) region as functions of κ_f (1σ and 2σ uncertainties in green and yellow bands), in comparison with number of events expected by HL-LHC (1σ and 2σ uncertainties in red and pink bands), with 3000 fb^{-1} proton-proton collisions at $\sqrt{s} = 14$ TeV. See text for details.

The analysis in the off-shell region may be further improved in two ways. The first is to improve the statistics and include the $WW \to 2\ell 2\nu$ final states. The second is to suppress the ZZ (WW) continuum background by employing a matrix-element-based method, as done in Ref. [96, 106][1]. Due to the lack of experimental access, I was unable to perform the analysis with combined CMS and ATLAS results. I believe, however, an analysis based on ATLAS result would yield very similar constraints; and for the purpose of demonstrating our analysis methods, it suffices to use CMS results alone.

[1] See, e.g. Ref. [35, 107] for more details on the signal-background separation for $H \to ZZ$ and $H \to WW$ processes using the matrix element likelihood analysis.

Chapter 6

Discussion and Conclusions

In Chapters 2-4, I presented in detail the construction of the event generator for the processes of $e^-e^+ \to ZH$, $q\bar{q}' \to VH$, and $gg \to ZH$, within the framework of JHUGEN. Particular focus was given to the Higgs boson decaying to a pair of bottom quark. The $q\bar{q}' \to VH$ processes were calculated at leading order and next-to-leading order in QCD. The event generator was then used to simulate a variety of VH processes involving anomalous HVV, Htt, and Hbb couplings at lepton and hadron colliders. These simulations were used to not only present kinematic distributions of these processes, but also demonstrate techniques that may be applied to experimental data analysis. In particular, I applied the matrix-element-based kinematic discriminants in separating gg- and $q\bar{q}$-initiated events, as well as in resolving theoretical scenarios involving anomalous HVV, Hbb and Htt couplings. The asymmetry between ZH and WH processes was also discussed, and to take full advantage of the effect of the anomalous couplings on the asymmetry, one should go beyond simply counting the total number of events.

In Chapter 5, I suggested that the Yukawa coupling between the Higgs

boson and light quarks can be constrained by comparing the signal strength of Higgs boson production as functions of scaling factors of the Yukawa couplings with the value measured by the LHC experiments. The tightest constraints are set in the resonance region, which are listed in Table 5.2. Upon the original publication in 2016, these constraints are comparable with the best phenomenological results in the literature [91, 92]. While the analysis performed in the Higgs off-shell region does not place as tight limits on the scaling factor, it places independent constraints. In addition, I demonstrated that the analysis performed in a higher invariant mass region can receive improvement by taking advantage of the behavior of parton luminosity functions. While I believe that my analysis is sufficiently accurate for order-of-magnitude estimates, the present study ignores several theoretical as well as experimental details. Therefore, it will be the best if experimental collaborations perform a detailed analysis.

Outlooks

The tools and techniques I presented are for the study of HVV, Hbb, Htt, and Higgs boson coupling to light quarks. The Higgs boson coupling that has not been studied in this thesis is the Higgs boson self coupling HHH and $HHHH$, whose measurement is arguably the ultimate test of the Standard Model. Fortunately, the same techniques of constructing an event generator for the $gg \to ZH$ processes can be easily applied to that for the $gg \to HH(\to b\bar{b}b\bar{b})$ and $gg \to H \to HH(\to b\bar{b}b\bar{b})$ processes, which may be sensitive to HHH, Htt, and Hbb couplings. The representative Feynman diagrams are shown in

Fig. 6.1.

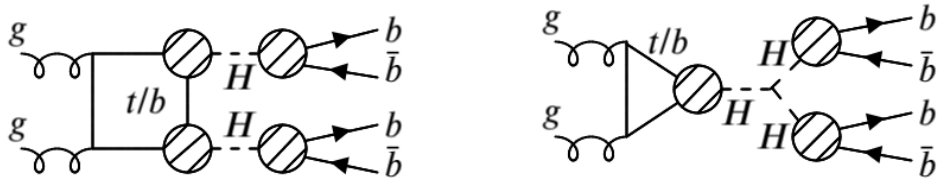

Figure 6.1: Representative Feynman diagrams of the $gg \to HH \to b\bar{b}b\bar{b}$ and $gg \to H \to HH \to b\bar{b}b\bar{b}$ processes. The shaded blob indicates the Higgs Yukawa interactions with anomalous couplings.

As a matter of fact, I have implemented the matrix element of this process in JHUGEN, including the anomalous Htt, and Hbb couplings, and the generator for both weighted and unweighted events are in development.

Another development one can make based on the NLO calculation of the $V^* \to VH$ processes is to produce unweighted events and perform matrix-element likelihood analysis at the next-to-leading order. The technique for achieving these can be found in Ref. [108]. These next-to-leading order techniques not only provide some treatment of the jet radiation, but also handles kinematics more realistically because at NLO the $V^* \to VH$ system may have non-zero transverse momentum.

References

[1] Georges Aad et al. "Search for the Standard Model Higgs boson produced in association with top quarks and decaying into $b\bar{b}$ in pp collisions at $\sqrt{s}$ = 8 TeV with the ATLAS detector". In: *Eur. Phys. J.* C75.7 (2015), p. 349. DOI: 10.1140/epjc/s10052-015-3543-1. arXiv: 1503.05066 [hep-ex].

[2] Serguei Chatrchyan et al. "Observation of a new boson at a mass of 125 GeV with the CMS experiment at the LHC". In: *Phys. Lett.* B716 (2012), pp. 30–61. DOI: 10.1016/j.physletb.2012.08.021. arXiv: 1207.7235 [hep-ex].

[3] M. Aaboud et al. "Observation of Higgs boson production in association with a top quark pair at the LHC with the ATLAS detector". In: *Phys. Lett.* B784 (2018), pp. 173–191. DOI: 10.1016/j.physletb.2018.07.035. arXiv: 1806.00425 [hep-ex].

[4] Albert M Sirunyan et al. "Observation of $t\bar{t}H$ production". In: *Phys. Rev. Lett.* 120.23 (2018), p. 231801. DOI: 10.1103/PhysRevLett.120.231801, 10.1130/PhysRevLett.120.231801. arXiv: 1804.02610 [hep-ex].

[5] Morad Aaboud et al. "Observation of $H \to b\bar{b}$ decays and VH production with the ATLAS detector". In: (2018). arXiv: 1808.08238 [hep-ex].

[6] Albert M Sirunyan et al. "Observation of Higgs boson decay to bottom quarks". In: (2018). arXiv: 1808.08242 [hep-ex].

[7] Albert M Sirunyan et al. "Observation of the Higgs boson decay to a pair of τ leptons with the CMS detector". In: *Phys. Lett.* B779 (2018), pp. 283–316. DOI: 10.1016/j.physletb.2018.02.004. arXiv: 1708.00373 [hep-ex].

[8] Morad Aaboud et al. "Cross-section measurements of the Higgs boson decaying into a pair of τ-leptons in proton-proton collisions at $\sqrt{s} = 13$

TeV with the ATLAS detector". In: *Submitted to: Phys. Rev.* (2018). arXiv: 1811.08856 [hep-ex].

[9] Georges Aad et al. "Measurements of Higgs boson production and couplings in the four-lepton channel in pp collisions at center-of-mass energies of 7 and 8 TeV with the ATLAS detector". In: *Phys. Rev.* D91.1 (2015), p. 012006. DOI: 10.1103/PhysRevD.91.012006. arXiv: 1408.5191 [hep-ex].

[10] Georges Aad et al. "Search for the Standard Model Higgs boson produced in association with a vector boson and decaying into a tau pair in pp collisions at $\sqrt{s} = 8$ TeV with the ATLAS detector". In: *Phys. Rev.* D93.9 (2016), p. 092005. DOI: 10.1103/PhysRevD.93.092005. arXiv: 1511.08352 [hep-ex].

[11] M. Aaboud et al. "Evidence for the $H \to b\bar{b}$ decay with the ATLAS detector". In: *JHEP* 12 (2017), p. 024. DOI: 10.1007/JHEP12(2017)024. arXiv: 1708.03299 [hep-ex].

[12] Morad Aaboud et al. "Measurement of the Higgs boson coupling properties in the $H \to ZZ^* \to 4\ell$ decay channel at $\sqrt{s}$ = 13 TeV with the ATLAS detector". In: *JHEP* 03 (2018), p. 095. DOI: 10.1007/JHEP03(2018)095. arXiv: 1712.02304 [hep-ex].

[13] Morad Aaboud et al. "Measurements of Higgs boson properties in the diphoton decay channel with 36 fb^{-1} of pp collision data at $\sqrt{s} = 13$ TeV with the ATLAS detector". In: (2018). arXiv: 1802.04146 [hep-ex].

[14] *Observation of $H \to b\bar{b}$ decays and VH production with the ATLAS detector*. Tech. rep. ATLAS-CONF-2018-036. Geneva: CERN, 2018. URL: http://cds.cern.ch/record/2630338.

[15] Vardan Khachatryan et al. "Search for a pseudoscalar boson decaying into a Z boson and the 125 GeV Higgs boson in $\ell^+\ell^- b\bar{b}$ final states". In: *Phys. Lett.* B748 (2015), pp. 221–243. DOI: 10.1016/j.physletb.2015.07.010. arXiv: 1504.04710 [hep-ex].

[16] Vardan Khachatryan et al. "Precise determination of the mass of the Higgs boson and tests of compatibility of its couplings with the standard model predictions using proton collisions at 7 and 8 TeV". In: *Eur. Phys. J.* C75.5 (2015), p. 212. DOI: 10.1140/epjc/s10052-015-3351-7. arXiv: 1412.8662 [hep-ex].

[17] Vardan Khachatryan et al. "Combined search for anomalous pseudoscalar HVV couplings in VH(H $\to b\bar{b}$) production and H $\to$ VV decay". In: *Phys. Lett.* B759 (2016), pp. 672–696. DOI: 10.1016/j.physletb.2016.06.004. arXiv: 1602.04305 [hep-ex].

[18] Georges Aad et al. "Measurements of the Higgs boson production and decay rates and constraints on its couplings from a combined ATLAS and CMS analysis of the LHC pp collision data at $\sqrt{s} = 7$ and 8 TeV". In: *JHEP* 08 (2016), p. 045. DOI: 10.1007/JHEP08(2016)045. arXiv: 1606.02266 [hep-ex].

[19] Albert M Sirunyan et al. "Constraints on anomalous Higgs boson couplings using production and decay information in the four-lepton final state". In: *Phys. Lett.* B775 (2017), pp. 1–24. DOI: 10.1016/j.physletb.2017.10.021. arXiv: 1707.00541 [hep-ex].

[20] Albert M Sirunyan et al. "Evidence for the Higgs boson decay to a bottom quark–antiquark pair". In: *Phys. Lett.* B780 (2018), pp. 501–532. DOI: 10.1016/j.physletb.2018.02.050. arXiv: 1709.07497 [hep-ex].

[21] *Observation of Higgs boson decay to bottom quarks*. Tech. rep. CMS-PAS-HIG-18-016. Geneva: CERN, 2018. URL: https://cds.cern.ch/record/2633415.

[22] *Search for the standard model Higgs boson decaying to a pair of τ leptons and produced in association with a W or a Z boson in proton-proton collisions at $\sqrt{s} = 13$ TeV*. Tech. rep. CMS-PAS-HIG-18-007. Geneva: CERN, 1900. URL: https://cds.cern.ch/record/2621550.

[23] *Measurements of properties of the Higgs boson in the four-lepton final state at $\sqrt{s} = 13$ TeV*. Tech. rep. CMS-PAS-HIG-18-001. Geneva: CERN, 2018. URL: https://cds.cern.ch/record/2621419.

[24] *Combined measurements of the Higgs boson's couplings at $\sqrt{s} = 13$ TeV*. Tech. rep. CMS-PAS-HIG-17-031. Geneva: CERN, 2018. URL: https://cds.cern.ch/record/2308127.

[25] Albert M Sirunyan et al. "Search for resonant pair production of Higgs bosons decaying to bottom quark-antiquark pairs in proton-proton collisions at 13 TeV". In: *Submitted to: JHEP* (2018). arXiv: 1806.03548 [hep-ex].

[26] F. Englert and R. Brout. "Broken Symmetry and the Mass of Gauge Vector Mesons". In: *Phys. Rev. Lett.* 13 (9 1964), pp. 321–323. DOI: 10.1103/PhysRevLett.13.321. URL: https://link.aps.org/doi/10.1103/PhysRevLett.13.321.

[27] Peter W. Higgs. "Broken symmetries, massless particles and gauge fields". In: *Phys. Lett.* 12 (1964), pp. 132–133. DOI: 10.1016/0031-9163(64)91136-9.

[28] Peter W. Higgs. "Broken Symmetries and the Masses of Gauge Bosons". In: *Phys. Rev. Lett.* 13 (16 1964), pp. 508–509. DOI: 10.1103/PhysRevLett.13.508. URL: https://link.aps.org/doi/10.1103/PhysRevLett.13.508.

[29] G. S. Guralnik, C. R. Hagen, and T. W. B. Kibble. "Global Conservation Laws and Massless Particles". In: *Phys. Rev. Lett.* 13 (20 1964), pp. 585–587. DOI: 10.1103/PhysRevLett.13.585. URL: https://link.aps.org/doi/10.1103/PhysRevLett.13.585.

[30] Sheldon L. Glashow. "The renormalizability of vector meson interactions". In: *Nucl. Phys.* 10 (1959), pp. 107–117. DOI: 10.1016/0029-5582(59)90196-8.

[31] Abdus Salam and J. C. Ward. "Weak and electromagnetic interactions". In: *Il Nuovo Cimento (1955-1965)* 11.4 (1959), pp. 568–577. ISSN: 1827-6121. DOI: 10.1007/BF02726525. URL: https://doi.org/10.1007/BF02726525.

[32] S. Weinberg. "A Model of Leptons". In: *Physical Review Letters* 19 (1967), pp. 1264–1266. DOI: 10.1103/PhysRevLett.19.1264.

[33] Kien Nguyen. "Lecture notes on Higgs phenomenon". In: (). URL: https://www.theorie.physik.uni-muenchen.de/lsfrey/teaching/archiv/sose_09/rng/higgs_mechanism.pdf.

[34] Mark Srednicki. *Quantum Field Theory*. Cambridge: Cambridge Univ. Press, 2007. URL: https://cds.cern.ch/record/1019751.

[35] Ian Anderson et al. "Constraining anomalous HVV interactions at proton and lepton colliders". In: *Phys. Rev.* D89.3 (2014), p. 035007. DOI: 10.1103/PhysRevD.89.035007. arXiv: 1309.4819 [hep-ph].

[36] A. Soni and R. M. Xu. "Probing CP violation via Higgs decays to four leptons". In: *Phys. Rev.* D48 (1993), pp. 5259–5263. DOI: 10.1103/PhysRevD.48.5259. arXiv: hep-ph/9301225 [hep-ph].

[37] Sara Bolognesi, Yanyan Gao, Andrei V. Gritsan, Kirill Melnikov, Markus Schulze, Nhan V. Tran, and Andrew Whitbeck. "On the spin and parity of a single-produced resonance at the LHC". In: *Phys. Rev.* D86 (2012), p. 095031. DOI: 10.1103/PhysRevD.86.095031. arXiv: 1208.4018 [hep-ph].

[38] Yanyan Gao, Andrei V. Gritsan, Zijin Guo, Kirill Melnikov, Markus Schulze, and Nhan V. Tran. "Spin determination of single-produced resonances at hadron colliders". In: *Phys. Rev.* D81 (2010), p. 075022. DOI: 10.1103/PhysRevD.81.075022. arXiv: 1001.3396 [hep-ph].

[39] Yaofu Zhou. "Constraining the Higgs boson coupling to light quarks in the H $\to$ ZZ final states". In: *Phys. Rev.* D93.1 (2016), p. 013019. DOI: 10.1103/PhysRevD.93.013019. arXiv: 1505.06369 [hep-ph].

[40] G Peter Lepage. "A new algorithm for adaptive multidimensional integration". In: *Journal of Computational Physics* 27.2 (1978), pp. 192–203. ISSN: 0021-9991. DOI: https://doi.org/10.1016/0021-9991(78)90004-9. URL: http://www.sciencedirect.com/science/article/pii/0021999178900049.

[41] R. Keith Ellis, Zoltan Kunszt, Kirill Melnikov, and Giulia Zanderighi. "One-loop calculations in quantum field theory: from Feynman diagrams to unitarity cuts". In: *Phys. Rept.* 518 (2012), pp. 141–250. DOI: 10.1016/j.physrep.2012.01.008. arXiv: 1105.4319 [hep-ph].

[42] Lance J. Dixon. "Calculating scattering amplitudes efficiently". In: *QCD and beyond. Proceedings, Theoretical Advanced Study Institute in Elementary Particle Physics, TASI-95, Boulder, USA, June 4-30, 1995*. 1996, pp. 539–584. arXiv: hep-ph/9601359 [hep-ph]. URL: http://www-public.slac.stanford.edu/sciDoc/docMeta.aspx?slacPubNumber=SLAC-PUB-7106.

[43] Michael E. Peskin and Daniel V. Schroeder. *An Introduction to quantum field theory*. Reading, USA: Addison-Wesley, 1995. ISBN: 9780201503975, 0201503972. URL: http://www.slac.stanford.edu/~mpeskin/QFT.html.

[44] J. Kuipers, T. Ueda, J. A. M. Vermaseren, and J. Vollinga. "FORM version 4.0". In: *Comput. Phys. Commun.* 184 (2013), pp. 1453–1467. DOI: 10.1016/j.cpc.2012.12.028. arXiv: 1203.6543 [cs.SC].

[45] Gavin Cullen, Maciej Koch-Janusz, and Thomas Reiter. "Spinney: A Form Library for Helicity Spinors". In: *Comput. Phys. Commun.* 182 (2011), pp. 2368–2387. DOI: 10.1016/j.cpc.2011.06.007. arXiv: 1008.0803 [hep-ph].

[46] Andy Buckley, James Ferrando, Stephen Lloyd, Karl Nordström, Ben Page, Martin Rüfenacht, Marek Schönherr, and Graeme Watt. "LHAPDF6: parton density access in the LHC precision era". In: *Eur. Phys. J.* C75 (2015), p. 132. DOI: 10.1140/epjc/s10052-015-3318-8. arXiv: 1412.7420 [hep-ph].

[47] Gerald Aarons et al. "ILC Reference Design Report Volume 3 - Accelerator". In: (2007). Ed. by Nan Phinney, Nobukazu Toge, and Nicholas J. Walker. arXiv: 0712.2361 [physics.acc-ph].

[48] The CEPC-SPPC Study Group. *CEPC-SppC Preliminary Conceptual Design Report Volume II: Accelerator*. Beijing, 2015. URL: http://cepc.ihep.ac.cn/preCDR/volume.html.

[49] Johan Alwall et al. "A Standard format for Les Houches event files". In: *Comput. Phys. Commun.* 176 (2007), pp. 300–304. DOI: 10.1016/j.cpc.2006.11.010. arXiv: hep-ph/0609017 [hep-ph].

[50] Peter Uwer. "EasyNData: A Simple tool to extract numerical values from published plots". In: (2007). arXiv: 0710.2896 [physics.comp-ph].

[51] Sayipjamal Dulat, Tie-Jiun Hou, Jun Gao, Marco Guzzi, Joey Huston, Pavel Nadolsky, Jon Pumplin, Carl Schmidt, Daniel Stump, and C. P. Yuan. "New parton distribution functions from a global analysis of quantum chromodynamics". In: *Phys. Rev.* D93.3 (2016), p. 033006. DOI: 10.1103/PhysRevD.93.033006. arXiv: 1506.07443 [hep-ph].

[52] A. D. Martin, W. J. Stirling, R. S. Thorne, and G. Watt. "Parton distributions for the LHC". In: *Eur. Phys. J.* C63 (2009), pp. 189–285. DOI: 10.1140/epjc/s10052-009-1072-5. arXiv: 0901.0002 [hep-ph].

[53] Richard D. Ball et al. "Parton distributions from high-precision collider data". In: *Eur. Phys. J.* C77.10 (2017), p. 663. DOI: 10.1140/epjc/s10052-017-5199-5. arXiv: 1706.00428 [hep-ph].

[54] Paul Avery et al. "Precision studies of the Higgs boson decay channel $H \to ZZto4\ell$ with MEKD". In: *Phys. Rev.* D87.5 (2013), p. 055006. DOI: 10.1103/PhysRevD.87.055006. arXiv: 1210.0896 [hep-ph].

[55] B. Hespel, F. Maltoni, and E. Vryonidou. "Higgs and Z boson associated production via gluon fusion in the SM and the 2HDM". In: *JHEP* 06 (2015), p. 065. DOI: 10.1007/JHEP06(2015)065. arXiv: 1503.01656 [hep-ph].

[56] W. H. Furry. "A Symmetry Theorem in the Positron Theory". In: *Phys. Rev.* 51 (2 1937), pp. 125–129. DOI: 10.1103/PhysRev.51.125. URL: https://link.aps.org/doi/10.1103/PhysRev.51.125.

[57] G. Passarino and M. J. G. Veltman. "One Loop Corrections for e+ e- Annihilation Into mu+ mu- in the Weinberg Model". In: *Nucl. Phys.* B160 (1979), pp. 151–207. DOI: 10.1016/0550-3213(79)90234-7.

[58] Ansgar Denner. "Techniques for calculation of electroweak radiative corrections at the one loop level and results for W physics at LEP-200". In: *Fortsch. Phys.* 41 (1993), pp. 307–420. DOI: 10.1002/prop.2190410402. arXiv: 0709.1075 [hep-ph].

[59] Stefano Carrazza, R. Keith Ellis, and Giulia Zanderighi. "QCDLoop: a comprehensive framework for one-loop scalar integrals". In: *Comput. Phys. Commun.* 209 (2016), pp. 134–143. DOI: 10.1016/j.cpc.2016.07.033. arXiv: 1605.03181 [hep-ph].

[60] Ansgar Denner, Stefan Dittmaier, and Lars Hofer. "Collier: a fortran-based Complex One-Loop LIbrary in Extended Regularizations". In: *Comput. Phys. Commun.* 212 (2017), pp. 220–238. DOI: 10.1016/j.cpc.2016.10.013. arXiv: 1604.06792 [hep-ph].

[61] Stefan Dittmaier. "Separation of soft and collinear singularities from one loop N point integrals". In: *Nucl. Phys.* B675 (2003), pp. 447–466. DOI: 10.1016/j.nuclphysb.2003.10.003. arXiv: hep-ph/0308246 [hep-ph].

[62] Wolfram Research, Inc. *Mathematica, Version 11.3*.

[63] D. de Florian et al. "Handbook of LHC Higgs Cross Sections: 4. Deciphering the Nature of the Higgs Sector". In: (2016). DOI: 10.23731/CYRM-2017-002. arXiv: 1610.07922 [hep-ph].

[64] R. V. Harlander, J. Klappert, C. Pandini, and A. Papaefstathiou. "Exploiting the WH/ZH symmetry in the search for New Physics". In: (2018). arXiv: 1804.02299 [hep-ph].

[65] John M. Campbell, R. Keith Ellis, and Ciaran Williams. "Associated production of a Higgs boson at NNLO". In: *JHEP* 06 (2016), p. 179. DOI: 10.1007/JHEP06(2016)179. arXiv: 1601.00658 [hep-ph].

[66] Giancarlo Ferrera, Gábor Somogyi, and Francesco Tramontano. "Associated production of a Higgs boson decaying into bottom quarks at the LHC in full NNLO QCD". In: *Phys. Lett.* B780 (2018), pp. 346–351. DOI: 10.1016/j.physletb.2018.03.021. arXiv: 1705.10304 [hep-ph].

[67] Robert V. Harlander, Jonas Klappert, Stefan Liebler, and Lukas Simon. "vh@nnlo-v2: New physics in Higgs Strahlung". In: *JHEP* 05 (2018), p. 089. DOI: 10.1007/JHEP05(2018)089. arXiv: 1802.04817 [hep-ph].

[68] Fabrizio Caola, Gionata Luisoni, Kirill Melnikov, and Raoul Röntsch. "NNLO QCD corrections to associated WH production and $H \to b\bar{b}$ decay". In: *Phys. Rev.* D97.7 (2018), p. 074022. DOI: 10.1103/PhysRevD.97.074022. arXiv: 1712.06954 [hep-ph].

[69] Pazilet Obul, Sayipjamal Dulat, Tie-Jiun Hou, Ablikim Tursun, and Nijat Yalkun. "Next-to-leading order QCD and electroweak corrections to Higgs-strahlung processes at the LHC". In: *Chin. Phys.* C42.9 (2018), p. 093105. DOI: 10.1088/1674-1137/42/9/093105. arXiv: 1801.06851 [hep-ph].

[70] Liang-Wen Chen, Wen-Gan Ma, Ren-You Zhang, Xiao-Zhou Li, and Yong Wang. "HZ associated production at the LHC within the littlest Higgs model at NLO+NLL accuracy". In: *Phys. Rev.* D94.7 (2016), p. 074020. DOI: 10.1103/PhysRevD.94.074020. arXiv: 1610.05476 [hep-ph].

[71] Fabio Maltoni, Kentarou Mawatari, and Marco Zaro. "Higgs characterisation via vector-boson fusion and associated production: NLO and parton-shower effects". In: *Eur. Phys. J.* C74.1 (2014), p. 2710. DOI: 10.1140/epjc/s10052-013-2710-5. arXiv: 1311.1829 [hep-ph].

[72] S. Catani and M. H. Seymour. "A General algorithm for calculating jet cross-sections in NLO QCD". In: *Nucl. Phys.* B485 (1997), pp. 291–419. DOI: 10.1016/S0550-3213(96)00589-5, 10.1016/S0550-3213(98)81022-5. arXiv: hep-ph/9605323 [hep-ph].

[73] W. Beenakker, S. Dittmaier, M. Kramer, B. Plumper, M. Spira, and P. M. Zerwas. "NLO QCD corrections to t anti-t H production in hadron collisions". In: *Nucl. Phys.* B653 (2003), pp. 151–203. DOI: 10.1016/S0550-3213(03)00044-0. arXiv: hep-ph/0211352 [hep-ph].

[74] Zoltan Nagy. "Next-to-leading order calculation of three jet observables in hadron hadron collision". In: *Phys. Rev.* D68 (2003), p. 094002. DOI: 10.1103/PhysRevD.68.094002. arXiv: hep-ph/0307268 [hep-ph].

[75] Tanju Gleisberg and Frank Krauss. "Automating dipole subtraction for QCD NLO calculations". In: *Eur. Phys. J.* C53 (2008), pp. 501–523. DOI: 10.1140/epjc/s10052-007-0495-0. arXiv: 0709.2881 [hep-ph].

[76] The ATLAS collaboration. "Measurements of the Higgs boson production and decay rates and coupling strengths using pp collision data at $\sqrt{s}$ = 7 and 8 TeV in the ATLAS experiment". In: (2015).

[77] The ATLAS collaboration. "Study of the spin and parity of the Higgs boson in HVV decays with the ATLAS detector". In: (2015).

[78] Vardan Khachatryan et al. "Precise determination of the mass of the Higgs boson and tests of compatibility of its couplings with the standard model predictions using proton collisions at 7 and 8 TeV". In: *Eur. Phys. J.* C75.5 (2015), p. 212. DOI: 10.1140/epjc/s10052-015-3351-7. arXiv: 1412.8662 [hep-ex].

[79] Georges Aad et al. "Search for the Standard Model Higgs boson produced in association with top quarks and decaying into $b\bar{b}$ in pp collisions at $\sqrt{s}$ = 8 TeV with the ATLAS detector". In: *Eur. Phys. J.* C75.7 (2015), p. 349. DOI: 10.1140/epjc/s10052-015-3543-1. arXiv: 1503.05066 [hep-ex].

[80] Georges Aad et al. "Search for $H \to \gamma\gamma$ produced in association with top quarks and constraints on the Yukawa coupling between the top quark and the Higgs boson using data taken at 7 TeV and 8 TeV with the ATLAS detector". In: *Phys. Lett.* B740 (2015), pp. 222–242. DOI: 10.1016/j.physletb.2014.11.049. arXiv: 1409.3122 [hep-ex].

[81] Georges Aad et al. "Search for the $b\bar{b}$ decay of the Standard Model Higgs boson in associated $(W/Z)H$ production with the ATLAS detector". In: *JHEP* 01 (2015), p. 069. DOI: 10.1007/JHEP01(2015)069. arXiv: 1409.6212 [hep-ex].

[82] Vardan Khachatryan et al. "Search for a Standard Model Higgs Boson Produced in Association with a Top-Quark Pair and Decaying to Bottom Quarks Using a Matrix Element Method". In: *Eur. Phys. J.* C75.6 (2015), p. 251. DOI: 10.1140/epjc/s10052-015-3454-1. arXiv: 1502.02485 [hep-ex].

[83] Vardan Khachatryan et al. "Search for the associated production of the Higgs boson with a top-quark pair". In: *JHEP* 09 (2014), p. 087. DOI: 10.1007/JHEP09(2014)087, 10.1007/JHEP10(2014)106. arXiv: 1408.1682 [hep-ex].

[84] Serguei Chatrchyan et al. "Search for the standard model Higgs boson produced in association with a W or a Z boson and decaying to bottom quarks". In: *Phys. Rev.* D89.1 (2014), p. 012003. DOI: 10.1103/PhysRevD.89.012003. arXiv: 1310.3687 [hep-ex].

[85] CMS Collaboration. "Search for H to bbbar in association with single top quarks as a test of Higgs couplings". In: (2014).

[86] Serguei Chatrchyan et al. "Evidence for the direct decay of the 125 GeV Higgs boson to fermions". In: *Nature Phys.* 10 (2014), pp. 557–560. DOI: 10.1038/nphys3005. arXiv: 1401.6527 [hep-ex].

[87] Georges Aad et al. "Search for the Standard Model Higgs boson decay to $\mu^+\mu^-$ with the ATLAS detector". In: *Phys. Lett.* B738 (2014), pp. 68–86. DOI: 10.1016/j.physletb.2014.09.008. arXiv: 1406.7663 [hep-ex].

[88] Georges Aad et al. "Evidence for the Higgs-boson Yukawa coupling to tau leptons with the ATLAS detector". In: *JHEP* 04 (2015), p. 117. DOI: 10.1007/JHEP04(2015)117. arXiv: 1501.04943 [hep-ex].

[89] Vardan Khachatryan et al. "Search for a standard model-like Higgs boson in the $\mu^+\mu^-$ and e^+e^- decay channels at the LHC". In: *Phys. Lett.* B744 (2015), pp. 184–207. DOI: 10.1016/j.physletb.2015.03.048. arXiv: 1410.6679 [hep-ex].

[90] Serguei Chatrchyan et al. "Evidence for the 125 GeV Higgs boson decaying to a pair of τ leptons". In: *JHEP* 05 (2014), p. 104. DOI: 10.1007/JHEP05(2014)104. arXiv: 1401.5041 [hep-ex].

[91] Gilad Perez, Yotam Soreq, Emmanuel Stamou, and Kohsaku Tobioka. "Constraining the charm Yukawa and Higgs-quark coupling universality". In: *Phys. Rev.* D92.3 (2015), p. 033016. DOI: 10.1103/PhysRevD.92.033016. arXiv: 1503.00290 [hep-ph].

[92] Alexander L. Kagan, Gilad Perez, Frank Petriello, Yotam Soreq, Stoyan Stoynev, and Jure Zupan. "Exclusive Window onto Higgs Yukawa Couplings". In: *Phys. Rev. Lett.* 114.10 (2015), p. 101802. DOI: 10.1103/PhysRevLett.114.101802. arXiv: 1406.1722 [hep-ph].

[93] Particle Data Group. In: *Chin. Phys.* C38.090001 (2014). URL: http://pdg.lbl.gov/2014/tables/rpp2014-sum-quarks.pdf.

[94] Nikolas Kauer and Giampiero Passarino. "Inadequacy of zero-width approximation for a light Higgs boson signal". In: *JHEP* 08 (2012), p. 116. DOI: 10.1007/JHEP08(2012)116. arXiv: 1206.4803 [hep-ph].

[95] Nikolas Kauer. "Inadequacy of zero-width approximation for a light Higgs boson signal". In: *Mod. Phys. Lett.* A28 (2013), p. 1330015. DOI: 10.1142/S0217732313300152. arXiv: 1305.2092 [hep-ph].

[96] Vardan Khachatryan et al. "Constraints on the Higgs boson width from off-shell production and decay to Z-boson pairs". In: *Phys. Lett.* B736 (2014), pp. 64–85. DOI: 10.1016/j.physletb.2014.06.077. arXiv: 1405.3455 [hep-ex].

[97] John M. Campbell and R. K. Ellis. "MCFM for the Tevatron and the LHC". In: *Nucl. Phys. Proc. Suppl.* 205-206 (2010), pp. 10–15. DOI: 10.1016/j.nuclphysbps.2010.08.011. arXiv: 1007.3492 [hep-ph].

[98] S. Dittmaier et al. "Handbook of LHC Higgs Cross Sections: 1. Inclusive Observables". In: (2011). DOI: 10.5170/CERN-2011-002. arXiv: 1101.0593 [hep-ph].

[99] J R Andersen et al. "Handbook of LHC Higgs Cross Sections: 3. Higgs Properties". In: (2013). Ed. by S Heinemeyer, C Mariotti, G Passarino, and R Tanaka. DOI: 10.5170/CERN-2013-004. arXiv: 1307.1347 [hep-ph].

[100] Giampiero Passarino. "Higgs CAT". In: *Eur. Phys. J.* C74 (2014), p. 2866. DOI: 10.1140/epjc/s10052-014-2866-7. arXiv: 1312.2397 [hep-ph].

[101] A. D. Martin, W. J. Stirling, R. S. Thorne, and G. Watt. "Parton distributions for the LHC". In: *Eur. Phys. J.* C63 (2009), pp. 189–285. DOI: 10.1140/epjc/s10052-009-1072-5. arXiv: 0901.0002 [hep-ph].

[102] Johan Alwall, Michel Herquet, Fabio Maltoni, Olivier Mattelaer, and Tim Stelzer. "MadGraph 5 : Going Beyond". In: *JHEP* 06 (2011), p. 128. DOI: 10.1007/JHEP06(2011)128. arXiv: 1106.0522 [hep-ph].

[103] Anastasiya Bierweiler, Tobias Kasprzik, and Johann H. Kühn. "Vector-boson pair production at the LHC to $\mathcal{O}(\alpha^3)$ accuracy". In: *JHEP* 12 (2013), p. 071. DOI: 10.1007/JHEP12(2013)071. arXiv: 1305.5402 [hep-ph].

[104] Julien Baglio, Le Duc Ninh, and Marcus M. Weber. "Massive gauge boson pair production at the LHC: a next-to-leading order story". In: *Phys. Rev.* D88 (2013), p. 113005. DOI: 10.1103/PhysRevD.94.099902, 10.1103/PhysRevD.88.113005. arXiv: 1307.4331 [hep-ph].

[105] "Properties of the Higgs-like boson in the decay H to ZZ to 4l in pp collisions at $\sqrt{s}$ =7 and 8 TeV". In: (2013).

[106] Vardan Khachatryan et al. “Limits on the Higgs boson lifetime and width from its decay to four charged leptons”. In: *Phys. Rev.* D92.7 (2015), p. 072010. DOI: 10.1103/PhysRevD.92.072010. arXiv: 1507.06656 [hep-ex].

[107] Sara Bolognesi, Yanyan Gao, Andrei V. Gritsan, Kirill Melnikov, Markus Schulze, Nhan V. Tran, and Andrew Whitbeck. “On the spin and parity of a single-produced resonance at the LHC”. In: *Phys. Rev.* D86 (2012), p. 095031. DOI: 10.1103/PhysRevD.86.095031. arXiv: 1208.4018 [hep-ph].

[108] Till Martini and Peter Uwer. “Extending the Matrix Element Method beyond the Born approximation: Calculating event weights at next-to-leading order accuracy”. In: *JHEP* 09 (2015), p. 083. DOI: 10.1007/JHEP09(2015)083. arXiv: 1506.08798 [hep-ph].

Yaofu Zhou

3701 San Martin Drive
Bloomberg 467
Baltimore, MD 21218

yzhou49@jhu.edu

Personal

I was born on November 18, 1988 in China, and received primary and secondary education in Shenzhen.

Education

- **Johns Hopkins University**, Baltimore, MD, 21218
  PhD in Physics, September 2011 – February 2019
  Field of Study: Phenomenological Particle Physics
  Joint Advisors: Prof. Jared Kaplan and Prof. Andrei Gritsan
- **Illinois Institute of Technology**, Chicago, IL 60616
  BS in Physics, August 2007 - May 2011
  Advisor: Prof. Zack Sullivan
  GPA: 3.72/4.00

Research

My main field of study is phenomenological particle physics. My recent focus has been Monte Carlo event generators with one-loop calculations and collider phenomenology of the Higgs boson and top quark. I am the co-developer of the JHUGen event generator, which is dedicated to the study of *XVV* interactions (*X* is a boson with arbitrary quantum numbers and arbitrary interactions with vector boson *V*). Previous studies include *W'* boson phenomenology, in which a generic *W'* model package for MadGraph/MadEvent was developed; and data analysis at the CDF Experiment.

Teaching

During my seven and half years of study at Johns Hopkins University, I gained extensive experience in teaching and assisting physics lectures. Courses I have taught the most are General Physics I and II, especially the laboratory part. Courses I have assisted include graduate level Statistical Mechanics, Electrodynamics, and General Relativity. I have also worked as an assistant in the lecture demonstration equipment room.

Publications

- Y. Zhou, *Constraining the Higgs Boson Coupling to Light Quarks in the H→ZZ Final States*, Phys. Rev. D 93, 013019 (2016), arXiv:1505.06369 [hep-ph]
- S. Dawson, et al., *Higgs Working Group Report of the Snowmass 2013 Community Planning Study*, (2013), arXiv:1310.8361 [hep-ex]
- Anderson, et al., *Constraining anomalous HVV interactions at proton and lepton colliders*, Phys. Rev. D 89, 035007 (2014), arXiv:1309.4819 [hep-ph]
- J. Freeman, et al, *Anomalous Coupling Limits from Z gamma Production Combining Electronic and Muonic Channels in 5/fb*, CDF Note 10043 (2010)

Awards

- German Academic Exchange Service (DAAD) Short-Term Research Grants, 2017
- The Coordinated Theoretical-Experimental Project on QCD (CTEQ) Summer School, Peking University, Beijing, China, 2014

Presentations

- *US-China Big Science Collaboration at Daya Bay*, China Brown Bag Talk, School for Advanced International Studies, Johns Hopkins University, 2016
- *Constraining anomalous HVV interactions at proton and lepton colliders*, Particle Theory Seminar, Michigan State University, 2014
- *Constraining and Measuring the Higgs Boson Total Width*, Journal Club Talk, Michigan State University, 2014
- *Constraining pseudoscalar HZZ interactions in Higgs production in association with Z*, 2014 Phenomenology Symposium, University of Pittsburg
- *Fully Differential W-prime Production and Decay in Arbitrary Models*, 2010 Prairie Section APS Meeting
- *Antimatter Gravity Experiment at Fermilab*, 2010 APS April Meeting
  Debugging a Mach-Zehnder Interferometer for Antimatter Gravity Experiment, 2009 Fermilab Users' Meeting

Translations

- English – Chinese translation. Adrienne Kolb, Lillian Hoddeson, and Michael Riordan, *Tunnel Visions: The Rise and Fall of the Superconducting Super Collider*, University of Chicago Press. Work in progress.
- Chinese – English translation. Artist Zhang Yan's backup speech to his Holiness Pope Francis and delegation of the Vatican Museums (unused), 2017.
- Chinese – English translation. Verbal introduction to the sketch *Holy Snowy Mountain*, artist Zhang Yan's donation to his Holiness Pope Francis, 2017.
- English – Chinese translation. Andrew Groen, *Empires of EVE: A History of the Great Wars of Eve Online* (Chapters of), 2015
- Chinese – English translation. Documentation on slow control system of Daya Bay Neutrino Experiment, 2009

Skills

Fortran, FORM, Mathematica, MCFM, MadGraph/MadEvent, Maple, C/C++, LaTeX, ROOT, Microsoft Office, and private pilot